

UNIVERSITY OF TOKYO

MASTERS THESIS

**Radio, Submillimetre, and Infrared Signals
from Embryonic Supernova Remnants**

誕生後数十年以内の超新星残骸からの
電波、サブミリ、近赤外放射

Author:
Conor M. B. OMAND

Supervisor:
Dr. Naoki YOSHIDA

*A thesis submitted in fulfillment of the requirements
for the degree of Masters of Science*

in the

Theoretical Astrophysics Group
Graduate School of Science

January 25, 2018

Declaration of Authorship

I, Conor M. B. OMAND, declare that this thesis titled, "Radio, Submillimetre, and Infrared Signals from Embryonic Supernova Remnants " and the work presented in it are my own. I confirm that:

- This work was done wholly or mainly while in candidature for a research degree at this University.
- Where any part of this thesis has previously been submitted for a degree or any other qualification at this University or any other institution, this has been clearly stated.
- Where I have consulted the published work of others, this is always clearly attributed.
- Where I have quoted from the work of others, the source is always given. With the exception of such quotations, this thesis is entirely my own work.
- I have acknowledged all main sources of help.

Abstract

Radio, Submillimetre, and Infrared Signals from Embryonic Supernova Remnants

Today, large surveys detect thousands of supernovae a year, and our understanding of their causes, mechanisms, and aftermath is very thorough. However, there are several other transients, including Gamma-Ray Bursts (GRBs), Hypernovae (HNe), Super-Luminous Supernovae (SLSNe), and Fast Radio Bursts (FRBs), where the causes and mechanisms are less certain or even completely unknown.

The remnant of the deaths of stars in a certain mass range is a neutron star. These dense stars can be rapidly rotating and have extremely large magnetic fields, thus emitting radiation and particles while losing their rotational energy (spinning down). These pulsars can emit more energy than the supernova explosion over their spin-down timescale, which can be as short as a few minutes. Many models predict that spin-down from pulsars with different properties can power multiple kinds of transients.

In this thesis, we explore the pulsar-powered supernova model and try and predict broadband emission from the pulsar wind nebula (PWN). Quasi-thermal optical supernova emission can not differentiate between different central supernova engines, but this non-thermal PWN emission is unique to the pulsar engine. We are interested in the detectability of this emission.

First, we overview the models used throughout the work. We describe the models for quasi- and non-thermal emission from SLSNe, and also models for dust formation, grain growth, sublimation, and thermal re-emission.

Next, we calculate the PWN emission from six bright newborn SLSN-I remnants, assuming that they are pulsar-driven, and examine the constraints placed by radio and submm emission. We find that the Atacama Large Millimeter/submillimetre Array (ALMA) can detect the submm PWN emission from most of them in a few years after the explosion, while the Jansky Very Large Array (VLA) can detect the radio PWN emission from a few of them in a few decades. We propose to study SN2015bn and SN2016ard with ALMA to detect this emission, which can tell us about the mechanism and central engine of SLSNe, as well as investigate the FRB-SLSN connection.

Then, we introduce and discuss the preliminary results of a study about an indirect detection method for young PWN: re-emission from dust grains. We study the growth of dust grains in the ejecta of a pulsar-powered supernova, and examine sublimation of smaller grains and re-emission from larger grains due to PWN emission. For the cases of SN2015bn and SN2016ard, we find that the dust emission is not detectable at all, although this may be due to an unphysical part of our model we have yet to be able to correct.

The combination of extreme gravity, magnetism, and density make neutron stars a unique laboratory to probe theories like general relativity, quantum electrodynamics, and nuclear physics, so it is important to understand their formation, life cycle, and diversity. Yet, the youngest pulsar astronomers know about, the Kes 75 pulsar, is around 700 years old. We hope to elucidate the connection between pulsars and transients to further our understanding of both compact objects and the luminous transients they may cause, and to detect and study newborn pulsars, only a few years after their birth, as new insights in various areas of physics and astronomy could come from identifying, modelling, and observing nascent neutron stars.

Acknowledgements

First and foremost, I would like to thank my supervisor, Naoki Yoshida, for his guidance during my entire masters program, particularly in making sure I always had the opportunities I needed to thrive. Next, I would like to thank my mentor and closest collaborator, Kazumi Kashiya, who has taught me almost everything I need to perform my current research and who is a constant source of information, encouragement, and assistance.

I want to thank all my other collaborators as well, which includes Kohta Murase, who collaborated with us in the radio detectability section (Chapter 3) and also wrote the ALMA proposal which 5 is based on, and the entire team for the ALMA proposal, which consists of Kohta Murase, Kazumi Kashiya, Hiroshi Nagai, Casey Law, Geoffrey Bower, Raffaella Margutti, Ryan Chornock, Deanna Coppejans, Derek Fox, Peter Mészáros. I also want to thank Kazumi Kashiya and Kohta Murase for writing most of the code used to derive the results in Chapter 3.

I want to thank everyone in UTAP for being a constant source of both help and entertainment for me, and for their willingness to make sure I don't miss out on anything due to my lack of Japanese skill. A special thank you to Liouhei Nakatani, who helped me code the implicit solver used to calculate dust properties in Chapter 4.

I need to thank a few previous mentors and supervisors who are responsible for where I am today. In chronological order, this includes my high school physics teacher Mark Sakakibara, who made physics fun and interesting and sparked my interest in the field; my first research supervisor, Sarah Burke, who took a chance on me as a young student and taught me a lot about performing research; Michael Balogh, who supervised my first successful research project and taught me how to write and publish papers; Petr Navrátil, who supervised another successful project and taught me how to perform large calculations; Seiji Miyashita, who supervised my internship at the University of Tokyo and strongly advocated for my return; and Jeremy Heyl, who supervised my honours thesis and subsequent internship and taught me a lot about high-energy physics, much of which I still use in my current research.

Finally, I want to thank my parents, Debbie and Michael, and brother, Travis, who've put up with me my whole life and who's support has allowed me to flourish, as well as my girlfriend, Anh, who I spend most of my downtime with and with whom my life in Tokyo has been significantly easier and more enjoyable.

Contents

Declaration of Authorship	iii
Abstract	v
Acknowledgements	vii
1 Introduction	1
1.1 A Historical Overview	1
1.2 Supernovae and Neutron Star Formation	3
1.2.1 Core Collapse and Compact Object Formation	3
1.2.2 Dynamics of Supernova Remnants	5
1.3 Neutron Star Overview	6
1.3.1 Pulsar Spin-Down Emission	7
1.3.2 Pulsar Wind Nebulae (PWNe)	9
1.3.3 Magnetars	12
SGR Flares	13
1.4 Possible Pulsar-Driven Transients	14
1.4.1 Gamma-Ray Bursts (GRBs) and Hypernovae (HNe)	16
1.4.2 Superluminous Supernovae (SLSNe)	18
1.4.3 Fast Radio Bursts (FRBs)	20
1.5 Thesis Overview	22
2 Theory and Models	25
2.1 Modeling SLSN Emission	25
2.1.1 Modelling Quasi-Thermal Optical Emission	25
Spin-Down	25
Ejecta Dynamics	27
Electromagnetic Emission	28
Peak Time and Luminosity	31
Summary	32
2.1.2 Modelling Non-Thermal Emission	33
Leptonic Emission from Embryonic PWNe - Analytical Model	33
Leptonic Emission from Embryonic PWNe - Numerical Model	36
Two-photon Annihilation in Embryonic PWNe	36
Matter Attenuation in the Stellar Material	37
2.2 Dust	41
2.2.1 Dust Formation	41
Introduction	41
Formation of a Dimer	42
Steady State Approximation	43
Cluster Formation	46
2.2.2 Criteria for Dust Sublimation	46
2.2.3 Dust Emission	47

3	Radio Emission from Embryonic SLSN Remnants	49
3.1	Introduction	49
3.2	Pulsar-driven Super-luminous Supernovae	51
3.2.1	Supernova Samples	51
3.2.2	Modeling of Optical Light Curves	51
3.3	Predictions for Radio Emission	55
3.3.1	Radio Emission from Embryonic Nebulae	55
3.3.2	Radio Emission from Ejecta Forward Shocks	61
3.4	Summary and Discussion	61
4	Preliminary Results: Thermal PWN Re-emission from Dust Grains	63
4.1	Introduction	63
4.2	Reproducing Previous Results	64
4.3	Study Overview	66
4.4	Preliminary Results	69
4.5	What Next?	75
5	Proposal: ALMA Observations of SN2015bn and SN2016ard	79
5.1	Overview	79
5.2	Scientific Justification	80
5.3	Description of Proposed Observations	81
5.4	Feasibility	82
6	Concluding Remarks	85
A	Analytic Integration of Equation 2.144	87

Chapter 1

Introduction

1.1 A Historical Overview

Astronomy is considered one of the oldest sciences, as many ancient civilizations collected astronomical information in a systematic manner through observation. This information was limited to the relative positions of celestial bodies, with subjects like the structure and chemical makeup of the planets and stars not being a consideration.

The beginning of transit astronomy may have been as early as 10 000 to 20 000 years ago. In 1977, an archeologist found carving left by ancient Native Americans in Bolivia. The carvings show two groups of small circles, which resemble stellar groupings in the constellations Vela and Carina, and two large circles: one may represent the star Capella, and the other is located near the position of the Vela Supernova Remnant. The archeologist suggested this may represent the supernova explosion as witnessed by the indigenous residents (Michanowsky 1977).

The first confirmed record of a supernova is from 185 CE, when Chinese astronomers recorded the appearance of a bright star in the sky and observed that it took about eight months to fade (Zhao et al. 2006). It sparkled like a star and did not move across the sky, like a comet would. SN 185 may have also have been recorded in Roman literature, but no records have survived (Stothers 1977). The gaseous shell RCW 86 is suspected as being the remnant of this event, as x-ray studies show a good match for the expected age (Vink et al. 2006).

Over the span of about 2000 years, Chinese astronomers recorded a total of twenty candidate supernovae, and some later explosions were also noted by Islamic, European, and possibly Indian and other observers (Chin & Huang 1994; Clark & Stephenson 1977; Stephenson & Clark 1976; Stephenson & Green 2003, 2005). Two of the most well known and brightest were SN 1006, which is the brightest observed stellar event in recorded history (reaching one quarter the brightness on the moon) and was recorded by astronomers in China, Egypt, Iraq, Italy, Japan and Switzerland, and may also have been noted in France, Syria, and North America (Murdin & Murdin 1985; Murdin & Murdin 2011; Winkler et al. 2003); and SN 1054, the precursor to the Crab Nebula, which had brightness comparable to Venus and was recorded by Arab, Chinese, and Japanese astronomers (Brecher et al. 1983).

Supernovae were originally thought to be something in the Earth's atmosphere, since the common belief in Europe before the 1700s was the Aristotelian idea that the world beyond the Moon and planets was immutable. Tycho Brahe noted that SN 1572 remained stationary from night to night - never changing its parallax - so it must lie far away. The modern word *nova* comes from the title of his book about these observations, *De nova et nullius aevi memoria prius visa stella* (Latin for "Concerning the new and previously unseen star") (Brahe 1573). Subsequent observations of SN 1604, the most recent supernova to be seen in the Milky Way, by Johannes Kepler led to

Galileo also trying, in vain, to measure the parallax of the supernova, and then also arguing against the Aristotelian view of an immutable heavens (Kepler 1606).

The first spectroscopic observations of a nova were done in 1866 by William Huggins, when he discovered lines of hydrogen in the unusual spectrum of the recurrent nova T Coronae Borealis. He proposed that a cataclysmic explosion was the underlying mechanism (Huggins 1866). In 1885, a nova-like burst was discovered in the direction of the Andromeda Galaxy, and once astronomers measured distance to the Andromeda Galaxy they realized the event must have released a much greater amount of energy than was typical for a nova. In the 1930s, Walter Baade and Fritz Zwicky postulated that the energy for these events, which they called super-novae (the hyphen was dropped before the end of the decade), was by the gravitational collapse of ordinary stars into neutron stars (Baade & Zwicky 1934; Osterbrock 2001), which was also the first postulation of the existence of neutron stars (Baade & Zwicky 1934).

In 1938, Baade was the first to identify a nebula as a supernova remnant (SNR) by associating the Crab Nebula with the remains of SN 1054 (Baade 1938). He noted that the expansion velocity was far too high to be a planetary nebula. He also proposed using what would later be called Type Ia supernova as a distance indicator. Later work refined the process and allowed Type Ia supernovae to become a type of standard candle for measuring large distances across the cosmos (Branch & Tammann 1992; Colgate 1979; Hamuy et al. 1996, 1993; Phillips 1993; Sandage et al. 1992).

While the first computer-controlled search for supernovae was begun in the 1960s, which was able to discover 14 supernovae over a period of two years (Marschall 1988), this time also marked the birth of neutron star astronomy. At first, they were thought to be too faint to be detectable and thus largely ignored by astronomers, but Franco Pacini pointed out that if neutron stars were spinning and had large magnetic fields, they would emit electromagnetic waves (Pacini 1967). The first neutron star to be detected was found by Antony Hewish and Samuel Okoye in 1965. They saw "an unusual source of high radio brightness temperature in the Crab Nebula" (Hewish & Okoye 1965), which turned out to be the Crab Pulsar (pulsar being short for "pulsating star"). In 1967, Iosif Shklovsky found evidence in x-ray and optical observations for a neutron star accreting matter from its companion in Scorpius X-1 (Shklovsky 1967), a system that was discovered five years earlier by a team led by Riccardo Giacconi (Giacconi et al. 1962). Later that year, Jocelyn Bell and Antony Hewish discovered regular radio pulses from four sources, which were later identified as pulsars (Gold 1968; Hewish et al. 1968; Pilkington et al. 1968). Hewish was awarded the Nobel Prize in 1974 for this discovery. To date, a large fraction of known neutron stars were discovered as pulsars emitting regular radio bursts (Rosswog & Brüggen 2007).

Since the 1960s, larger telescopes, more broadband sky coverage, and coordinated surveys have led to the discoveries of thousands of supernovae and neutron stars. The first discovery of x-ray pulsars was in 1971, when the *UHURU* satellite saw periodicity in the source Cen X-3 and Her X-1 (Schreier et al. 1972; Tananbaum et al. 1972). The first binary pulsar system was discovered in 1975 (Hulse & Taylor 1975), which provided an opportunity to measure the mass of a neutron star and test for the existence of gravitational radiation; a merger of a similar system was recently seen by the Laser Interferometer Gravitational-wave Observatory (LIGO) and various electromagnetic telescopes (Abbott et al. 2017a,b; Cowperthwaite et al. 2017; Soares-Santos et al. 2017; Tanaka et al. 2017; Utsumi et al. 2017). Observations of supernovae have started to see them at earlier times after the explosion, as SN 1987A was observed within hours of its start (McCray 1993) and SN 2008D was caught on camera just as it was exploding (Soderberg et al. 2008), allowing for early multiwavelength follow-up.

Peculiar classes of supernovae, such as hypernovae and superluminous supernovae, were discovered, and supernovae have also been associated with Gamma-Ray Bursts.

Thanks to current wide-field transient surveys, including the Palomar Transit Factory (PTF), La-Silla Quest Supernova Survey (LQSS), Dark Energy Survey (DES), and a survey with the upcoming Large Synoptic Survey Telescope (LSST), which will lead to the discovery of hundreds of thousands of supernovae every year (Ivezic et al. 2008; Skidmore et al. 2015); the next generation telescopes across the electromagnetic spectrum, including the Thirty Meter Telescope (TMT), James Webb Space Telescope (JWST), Wide-Field Infrared Survey Telescope - Astrophysics Focused Telescope Assets (WFIRST-AFTA), and Five-hundred-meter Aperture Spherical Telescope (FAST); and the birth of gravitational wave, and thus multi-messenger, astronomy; the future of supernovae and neutron star astronomy seems like it can only get brighter from here.

1.2 Supernovae and Neutron Star Formation

In the initial burning stages of a star, the hydrogen in the core is burnt into helium; this is known as the main sequence phase. Once the central hydrogen is depleted, the star contracts and heats up until the central helium ignites. The hydrogen shell is also burned off, and for stars with mass $> 0.5M_{\odot}$, the helium core ignites at $\sim 10^8$ K and produces carbon and oxygen, and smaller amounts of neon, magnesium, and silicon, via the triple-alpha process. Low mass stars do not burn further, as their self-gravity is not strong enough to further ignite carbon and oxygen via contraction. Instead, these stars eject their envelopes via thermal pulses caused by the temperature dependence of helium burning (Rosswog & Brüggen 2007). These envelopes are observable as planetary nebulae, and the remains of these stars are known as white dwarfs.

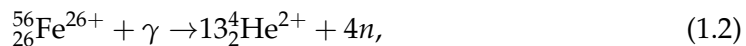
Stars more massive than $\sim 8M_{\odot}$ can burn carbon at $> 6 \times 10^8$ K to produce mostly oxygen, neon, and magnesium; and stars more massive than $\sim 9 - 10M_{\odot}$ can burn these into silicon, sulphur, calcium, argon, and finally iron, the strongest bound nuclei (Fewell 1995). Nuclear burning is only exothermic up to iron, and further burning would cost the system energy, so no further burning takes place. At this point, the star has a mostly iron core with a onion-esque structure comprised from shells of silicon, oxygen, carbon, helium, and hydrogen.

1.2.1 Core Collapse and Compact Object Formation

Once the iron core reaches the Chandrasekhar mass $1.44(Y_e/0.5)^2 M_{\odot}$, where Y_e is the number of leptons per baryon (Bethe et al. 1979), the electrons are ultrarelativistic and can not support the core against gravitational collapse, and so the iron core, no longer stabilized by electron degeneracy pressure, begins to contract (Chandrasekhar 1931, 1935; Lieb & Yau 1987). Electron capture

$$e^{-} + p^{+} \rightarrow n + \nu_e. \quad (1.1)$$

in the iron core reduces the pressure, and the temperatures become high enough to photodisintegrate the star through reactions like (den Hartog 2008; Rosswog & Brüggen 2007)



The collapsing core has two parts: an inner core of $\sim 0.8 M_{\odot}$ (corresponding to the Chandrasekhar mass at the local Y_e (Goldreich & Weber 1980)), which collapses homologously ($v \propto r$), and an outer, supersonically infalling core. The collapsing core is completely decoupled from the rest of the star, and the outer mantle is not affected by the collapse. In the early stages of infall, neutrinos from various weak interactions can escape the star almost unhindered, but once the density reaches $\sim 10^{12} \text{ g cm}^{-3}$ and the neutrino escape time becomes comparable to the infall time, the neutrinos are dragged along with the infalling core (Epstein et al. 1988; Haxton 1988; Hayakawa et al. 2006; Woosley et al. 1990; Woosley & Haxton 1988). Once this happens, neutrino and electron captures come to an equilibrium, and the reaction in Equation 1.1 becomes reversible.

Once the density becomes comparable to $\rho_{\text{nuc}} \sim 2.6 \times 10^{14} \text{ g cm}^{-3}$ and the nucleons are essentially touching, the short-range repulsive nuclear force begins to dominate and stiffens to material. The nearly-incompressible nuclear matter stops the collapse and makes the infalling material bounce back, which causes an outward-moving shock that triggers the supernova explosion.

The shock forms at 20-30 km and moves through several tenths of solar masses of infalling material, breaking up the iron nuclei into neutrons and protons. These interactions cause the shock to lose energy and stall around 10-20 ms after the bounce at a radius of 100-200 km, forming a quasi-stationary accretion shock. The mass enclosed by the shock keeps increasing as matter continues to fall in, but the shock stays at a constant radius.

The bulk of the gravitational energy from the collapse is converted into neutrinos, which diffuse out of the protoneutron star on a diffusion timescale $\tau_{\text{diff}} \sim 5 \text{ s}$ with a typical luminosity of $\sim 6 \times 10^{52} \text{ erg s}^{-1}$. Most of the neutrinos leave the star and carry away energy, but a small fraction deposit their energy in the stellar material. This deposition could serve to re-accelerate the shock and drive the explosion - this mechanism is known as the delayed explosion mechanism. This scenario is far from certain and often fails when simulated (Buras et al. 2006; Janka et al. 2007; Liebendoerfer 2005), although state-of-the-art simulations can reliably produce supernovae (Nagakura et al. 2017; Pan et al. 2016). Alternative hypotheses include the standing accretion shock instability, where perturbations to the accretion shock cause oscillations which destabilize it and cause re-acceleration (Abdikamalov et al. 2015; Blondin et al. 2003), and a mechanism where acoustic waves emitted by g -mode oscillations energize the stalled shock and eventually induce an explosion (Burrows et al. 2006a, 2007b; Harada et al. 2017).

As the shock wave breaks through the star, the inner regions are heated to high enough temperatures to synthesize further elements through nuclear fusion. Parts of the silicon shell are burnt into iron-peak nuclei, parts of the oxygen shell into intermediate mass nuclei, and some carbon into oxygen. Radioactive isotopes such as ^{56}Ni and ^{57}Ni , which help power the light curve peak, ^{56}Co , which helps power the ~ 30 -100 day light curve, and ^{44}Ti , which helps power the late-time light curve, are also produced.

Depending on whether the neutron-degeneracy pressure and short-range strong nuclear force can withstand the extreme gravity or not, a protoneutron star will either stabilize or the core will collapse into a black hole. If the neutron star is stable, the magnetic field from the original star will be strongly amplified during the collapse due to the rapid rotation of the new compact object. There are two other mechanisms which may amplify the magnetic field of a newborn neutron star. The first is the convective dynamo, where convective motion of the conducting fluid through the magnetic field produces more field, which adds to the original field (Bonanno et al.

2005; Burrows & Lattimer 1986; Duncan & Thompson 1992; Obergaulinger et al. 2014; Thompson & Duncan 1993). The other is collective magnetism, where domains of the material in the neutron star undergo a ferromagnetic transition to the Pauli-preferred triplet state at high density (Brownell & Callaway 1969; Haensel & Bonazzola 1996; Kutschera & Wójcik 1989). It is unknown which of these mechanisms dominate, or if they coexist to some extent (Lyne et al. 2013).

1.2.2 Dynamics of Supernova Remnants

Supernovae inject stellar material into the interstellar medium (ISM), which strongly affects gas distribution within galaxies. They play large roles in the heating and chemical evolution of galaxies, and their shocks can cause gas clouds to collapse and form new stars. Although the supernova itself is short, the SNR can emit electromagnetic radiation for about 100 000 years. Also, since elements heavier than helium are synthesized in star and ejected during supernovae, some material used to form the next generation of stars and planets comes from SNRs.

A SN with typical energy $E_{\text{SN}} \sim 10^{51}$ erg ejects matter with a velocity

$$E_{\text{SN}} \sim \frac{1}{2} M_{\text{ej}} v_{\text{ej}}^2, \quad (1.4)$$

$$v_{\text{ej}} \sim 10^4 \text{ km/s} \left(\frac{E_{\text{SN}}}{10^{51} \text{ erg}} \right)^{1/2} \left(\frac{M_{\text{ej}}}{M_{\odot}} \right)^{-1/2}. \quad (1.5)$$

The expansion of the supernova can be divided into roughly four phases, which are each dominated by a different physical principle. At first, the stellar ejecta retains its initial velocity such that the radius of the blast wave is $v_{\text{ej}} t$. As the blast wave sweeps up mass, energy conservation forces it to slow down. Generally, the blast wave has swept up M_{ej} during this time, and the radius is

$$r_1 \sim 2 \text{ pc} \left(\frac{\rho_{\text{ISM}}}{10^{-24} \text{ g cm}^{-3}} \right)^{-1/3} \left(\frac{M_{\text{ej}}}{M_{\odot}} \right)^{1/3}, \quad (1.6)$$

which occurs at time

$$t_1 \sim \frac{r_1}{v_{\text{ej}}} \sim 200 \text{ yr} \left(\frac{E_{\text{SN}}}{10^{51} \text{ erg}} \right)^{-1/2} \left(\frac{\rho_{\text{ISM}}}{10^{-24} \text{ g cm}^{-3}} \right)^{-1/3} \left(\frac{M_{\text{ej}}}{M_{\odot}} \right)^{5/6}. \quad (1.7)$$

In the second phase, since energy losses from radiation are still negligible, the ejecta expands adiabatically. The constant E_{SN} is proportional to $\rho_{\text{ISM}} r^3 v^2$, and since $v = \dot{r}$, we can write

$$E_{\text{SN}} / \rho_{\text{ISM}} \propto r^3 \dot{r}^2, \quad (1.8)$$

which can be integrated to give

$$r \propto (E_{\text{SN}} / \rho_{\text{ISM}})^{1/5} t^{2/5}. \quad (1.9)$$

This phase is known as the Sedov phase (Sedov 1946). In this second phase, the ejecta is decelerating as it expands, and since material further out decelerates earlier, the material inside runs into the outer shells, which heats up the outer shell and can produce complex flow patterns (Rosswog & Brüggen 2007).

The shocked gas still has a very high temperature. In the strong shock limit, the ratio of temperatures behind and in front of the shock is (Rosswog & Brüggen 2007)

$$\frac{T_2}{T_1} = \frac{2\Gamma(\Gamma-1)\mathcal{M}_\infty^2}{(\Gamma+1)^2} = \frac{5}{16}\mathcal{M}_\infty^2, \quad (1.10)$$

where \mathcal{M}_∞ is the Mach number of the shock with respect to the sound speed of the unshocked gas. The last quantity assumes the adiabatic exponent of the gas is $\Gamma = 5/3$.

The temperatures in this phase are roughly 10^6 K. When temperatures fall below 10^6 K, some ions start to recombine and form atoms. These atoms cool strongly due to line emission, and once the radiative losses affect the kinetic energy of the ejecta, the Sedov phase is over.

In the third phase, the outer shell cools so fast from line emission that it forms a cold, dense shell that is driven by the hotter interior. This shell propagates with constant radial momentum and piles up ambient material, giving this phase the name "snowplow phase". The constant momentum can be described by

$$\frac{d}{dt}[Mv] = \frac{d}{dt} \left[\left(\frac{4\pi}{3} \right) \rho r^3 \dot{r} \right] = 0. \quad (1.11)$$

If we set the initial conditions t_o , r_o , and v_o as when the thin shell first forms, then

$$\rho r^3 \dot{r} = \rho r_o^3 v_o, \quad (1.12)$$

which, when integrated, gives

$$r = \rho r_o \left(1 + \frac{4v_o(t-t_o)}{r_o} \right)^{1/4}, \quad (1.13)$$

which has $r \propto t^{1/4}$ at late times. In this phase, the gas has temperatures around 10^4 K, emits strong line emission, and strongly radiates in the optical band.

The final stage of the SNR is when the ejecta merges with the ISM. This happens when the ejecta speed becomes comparable to the sound speed of the ISM, usually around 10^5 years after the supernova explosion. At this point, it contributes its remaining kinetic energy to the general turbulence of the ISM flow.

1.3 Neutron Star Overview

The inner structure of a neutron star (NS) is described by the relationship between density and pressure, which gives an insight into the internal composition of the NS; the relationship is usually known as an equation of state (EoS). It is known that NSs are comprised mostly of neutrons, but also contain protons and electrons near their surface. The EoS at the centre of NSs is still an open question in NS astrophysics, and there could possibly be more exotic states of matter, such as quark-gluon plasma or quark-degenerate matter, in their ultra-dense cores (Burgio et al. 2002; Haensel et al. 2007; Pons et al. 2013). A variety of NS EoSs predict very different neutron star mass-radius relations, which allows this relation to be constrained by observational studies.

The first NS EoS was worked out by J. Robert Oppenheimer and George Volkoff in 1939 (Oppenheimer & Volkoff 1939), using the work of Richard Chace Tolman (Tolman 1939). They assumed the neutrons formed a cold degenerate Fermi gas, and obtained a maximum NS mass of $0.7 M_\odot$ (where $M_\odot = 1.98892 \times 10^{33}$ g is the mass

of the Sun) (Oppenheimer & Volkoff 1939). Recent work, which takes the strong nuclear interaction into account, leads to limiting masses between 2.0 and 3.0 M_{\odot} (Bombaci 1996; Chamel et al. 2013; Kalogera & Baym 1996). This limit, now known as the Tolman-Oppenheimer-Volkov limit, is uncertain because the equations of state of extremely dense matter are not well known. An empirical lower bound for the maximum mass is set by the most massive known neutron star, PSR J0348+0432, at $2.01 \pm 0.04 M_{\odot}$ (Antoniadis et al. 2013). Reviews by Lattimer & Prakash (2007) and Weber et al. (2007) give insight into the difficulties in the quest for the EoS.

In this thesis, we use a canonical NS with mass $M_{\text{NS}} = 1.4 M_{\odot}$ and radius $R = 1.2 \times 10^6 \text{ cm} = 12 \text{ km}$. The moment of inertia $I = kMR \sim 10^{45} \text{ g cm}^2$ is often used, and our value for k is 0.35, giving an overall value of $I = 1.4 \times 10^{45} \text{ g cm}^2$. Most pulsars have periods of 0.1 - 1 s, but some have periods as high as 10 s or as low as 1.4 ms (den Hartog 2008; Hessels et al. 2006; Manchester et al. 2005; Olausen & Kaspi 2014). The most rapidly rotating neutron stars have surface speeds of around 10% the speed of light.

There are three main subtypes of pulsars: rotation-powered pulsars, where the dipole radiation is powered by loss of rotational kinetic energy in star, causing its rotation to slow down (Rosswog & Brüggen 2007; Shapiro & Teukolsky 1983); accretion-powered pulsars, where gravitational potential energy of accreted matter powers the radiation (Zeilik & van Panhuys Smith 1987); and magnetars, where the radiation is powered by the decay of an extremely strong magnetic field (Brownlee 2003; Duncan & Thompson 1992; Heyl & Kulkarni 1998; Norris et al. 1991; Thompson & Duncan 1993; Thompson et al. 2002).

1.3.1 Pulsar Spin-Down Emission

Pulsars have a dipolar magnetic field and rotate with periods between 1 ms and 10 s. Pulsars that do not accrete generally slow down, losing rotational kinetic energy; most of this energy is emitted as energetic particles (called the pulsar wind) and high-energy radiation (den Hartog 2008), but there is also a pulsating radio signal from which pulsars, short for "pulsating stars", get their name. The dipole model (Ostriker & Gunn 1969; Pacini 1967, 1968) was the first model for examining the emission from pulsars, and still widely remains in use today.

The rotational kinetic energy of a NS with period P , angular frequency Ω , and moment of inertia I is

$$E = \frac{1}{2} I \Omega^2 \approx 2.76 \times 10^{52} \left(\frac{P}{1 \text{ ms}} \right)^{-2} \text{ erg.} \quad (1.14)$$

The kinetic energy loss from a NS with period derivative \dot{P} yields the maximum possible spin-down luminosity of the pulsar

$$\dot{E} = -\frac{d}{dt} \frac{1}{2} I \Omega^2 = -I \Omega \dot{\Omega} = I \frac{2\pi}{P} \frac{2\pi \dot{P}}{P^2} = 4\pi^2 I \frac{\dot{P}}{P^3} \approx 5.54 \times 10^{46} \frac{\dot{P}}{P^3} \text{ erg s}^{-1}. \quad (1.15)$$

Independent of the internal field geometry, a pure magnetic dipole field at the magnetic pole of the star, B_{dip} , is related to the magnetic dipole moment \mathbf{m} by

$$|\mathbf{m}| = \frac{B_{\text{dip}} R^3}{2}. \quad (1.16)$$

This configuration has a time-varying dipole moment as seen from infinity, and so radiates energy with power

$$\dot{E} = -\frac{2}{3c^3} |\ddot{\mathbf{m}}|^2. \quad (1.17)$$

Using

$$\mathbf{m} = \frac{B_{\text{dip}} R^3}{2} (\mathbf{e}_{\parallel} \cos \alpha + \mathbf{e}_{\perp} \sin \alpha \cos \Omega t + \mathbf{e}'_{\perp} \sin \alpha \sin \Omega t), \quad (1.18)$$

where \mathbf{e}_{\parallel} is a unit vector parallel to the rotation axis, \mathbf{e}_{\perp} and \mathbf{e}'_{\perp} are fixed mutually orthogonal unit vectors perpendicular to \mathbf{e}_{\parallel} , and α is the angle between the rotation axis and the magnetic polar axis. Substituting this into Equation 1.17 gives

$$\dot{E} = -\frac{B_{\text{dip}}^2 R^6 \Omega^4 \sin^2 \alpha}{6c^3}, \quad (1.19)$$

in which the radiation is emitted at frequency Ω .

If one assumes that the pulsar spin-down is caused by the torque of the magnetic field with its surroundings and that the emission process is completely dipole radiation, the characteristic surface magnetic field (at the poles) can be inferred by equating Equation 1.15 with Equation 1.19, giving

$$B_{\text{dip}} = \sqrt{\frac{3Ic^3}{2\pi^2 R^6 \sin^2 \alpha} P \dot{P}} = 4.39 \times 10^{19} \text{ G } \sqrt{P \dot{P}}, \quad (1.20)$$

Since α is generally not known, $\sin \alpha = 1$ is sometimes assumed (we take that assumption here) and the magnetic field strength at the equator, which is half of the field at the poles, is more commonly used as the characteristic value B_{char} .

The spin-down timescale t_{SD} of a pulsar is the ratio of the initial rotation energy and the initial spin-down luminosity

$$t_{\text{SD}} = \frac{E_{\text{rot}}}{\dot{E}} = \frac{\frac{1}{2} I \Omega^2}{I \Omega \dot{\Omega}} = \frac{\Omega}{2 \dot{\Omega}} = \frac{2P}{\dot{P}}, \quad (1.21)$$

A NS will lose much of its energy within t_{SD} , and the early emission will be extremely luminous. Substituting B_{char} in here gives

$$t_{\text{SD}} = \frac{3Ic^3}{4\pi^2 R^6} \left(\frac{P}{B_{\text{char}}} \right)^2 = 111 \text{ days } \left(\frac{P}{1 \text{ ms}} \right)^2 \left(\frac{B_{\text{char}}}{10^{13} \text{ G}} \right)^{-2} \quad (1.22)$$

which allows one to calculate t_{SD} from the initial period and magnetic field - common parameters in models. The energy lost during the initial spin-down $E_{\text{SD}} = E_{\text{rot}}$ from Equation 1.14, which does not depend on period derivative or magnetic field.

This dipole model is assumed to be in vacuum, but Goldreich & Julian (1969) showed by contradiction that a pulsar can not exist in a vacuum, since a rotating magnetic dipole surrounded by a vacuum will induce a Lorentz force parallel to the magnetic field. For pulsars, this force will exceed the gravitational force by orders of magnitude, and charged particles will be forced from the surface into the magnetosphere. The particles will co-rotate with the neutron star within the light cylinder magnetosphere.

Radiation can be created at different sites around the pulsar. Popular models are the polar-cap models which include the vacuum-gap model (Ruderman & Sutherland 1975; Usov & Melrose 1995) and the space-charge limited-flow gap model (Harding

& Muslimov 1998; Usov & Melrose 1995), slot-gap model (Arons 1983; Muslimov & Harding 2003) and outer-gap model (Cheng et al. 1986a; Hirovani 2006; Romani 1996). They are named after the sites where particle acceleration can be efficient due to an electric field parallel to the magnetic field. Mechanisms like curvature radiation, synchrotron radiation or inverse Compton scattering may play a role in creating the observed non-thermal emission ranging from radio to the gamma-ray bands (den Hartog 2008).

1.3.2 Pulsar Wind Nebulae (PWNe)

As noted in the previous section, most of the energy loss from spin-down goes into the emission of energetic particles (electron and positrons), known as a pulsar wind. If this magnetized wind is confined by an SNR or the interstellar medium, the boundary can form what's known as a wind termination shock, which accelerates the particles to ultrarelativistic energies, where they radiate synchrotron emission across the electromagnetic spectrum (Pacini & Salvati 1973; Rees & Gunn 1974). This confined pulsar wind is known as a pulsar wind nebula (PWN). Detailed theoretical evolution has been studied by Blondin et al. (2001); Bucciantini et al. (2003); Chevalier (1998); Reynolds & Chevalier (1984) and van der Swaluw et al. (2004).

The basic picture for the formation of pulsar winds is that a charge-filled magnetosphere surrounds the pulsar, and that particle acceleration occurs in charge-separated gaps either near the pulsar polar caps or in outer regions that extend to the light cylinder (where $R_{LC} = c/\Omega$). The maximum voltage generated by the rotating magnetic field in the case where the magnetic and spin axes are co-aligned is (Goldreich & Julian 1969)

$$\Delta\Phi = \frac{B_{\text{char}}\Omega^2 R_{\text{NS}}^3}{2c} \approx 10^{22} \text{ V} \left(\frac{B_{\text{char}}}{10^{13} \text{ G}} \right) \left(\frac{R_{\text{NS}}}{12 \text{ km}} \right) \left(\frac{P}{1 \text{ s}} \right) \quad (1.23)$$

Although this current is considerably modified in subsequent models, it provides the basis for our understanding of the pulsar wind.

In almost all models, the wind leaving the pulsar magnetosphere is dominated by the Poynting flux, $F_{E \times B}$, with the particle energy flux, F_{particle} , being much smaller. The magnetization parameter, σ_B , is

$$\sigma_B = \frac{F_{E \times B}}{F_{\text{particle}}} = \frac{B^2}{4\pi\rho\gamma c^2} \quad (1.24)$$

where B , ρ , and γ are the magnetic field, mass density of particles, and Lorentz factor, respectively, in the wind. Typically, wind leaving the magnetosphere has $\sigma_B > 10^4$, however, models for the structure and spectrum of the Crab Nebula (Kennel & Coroniti 1984; Rees & Gunn 1974) require $\sigma_B \sim 10^{-3}$ just behind the termination shock. The process that dissipates the magnetic energy and transfers it to particles is still unknown, and this question is commonly known as the "sigma problem" (Kirk & Skjæraasen 2004). Two possible mechanisms are magnetic reconnection in the current sheet generated by a striped wind (Kirk & Skjæraasen 2003; Lyubarsky & Kirk 2001; Lyubarsky 2003; Sironi & Spitkovsky 2011) and a kink instability in the field (Porth et al. 2013).

When the pulsar-driven wind decelerates from expanding into the cold, slowly expanding SN ejecta, there is a wind termination shock produced, which accelerates electron/positron pairs to ultrarelativistic energies. As they move through the

wound-up magnetic field of the PWN, they produce broadband synchrotron radiation. For a power-law electron spectrum, the constant injection of particles and a finite synchrotron-emitting lifetime lead to a spectral break at a frequency (Ginzburg & Syrovatskii 1965)

$$\nu_b = 10^{16} \text{ GHz} \left(\frac{B}{10^{-6} \text{ G}} \right)^{-3} \left(\frac{t}{10 \text{ yr}} \right)^{-2} \quad (1.25)$$

which results in the size of the PWN decreasing with increasing frequency. The particle injection must be greater than 10^{40} s^{-1} (Slane 2017), which is difficult to obtain from pair creation within pulsar magnetospheres (Timokhin & Harding 2015), suggesting that relic electrons created early in the PWN formation might be required (Atoyan & Aharonian 1996).

The highly relativistic magnetized pulsar wind inflates a bubble confined by the SN ejecta. The wind termination shock is formed at R_w , where the wind is decelerated by the slow, cold SN ejecta and the ram pressure of the wind is balanced by the internal pressure of the PWN:

$$R_w = \sqrt{\dot{E}/4\pi\omega c\mathcal{P}_{\text{PWN}}} \quad (1.26)$$

where ω is the equivalent filling factor for an isotropic wind, and \mathcal{P}_{PWN} is the total pressure in the shocked nebular interior. Upstream of this shock, the particles flow relativistically along with the frozen-in magnetic field instead of radiating. At the shock, particles are thermalized and reaccelerated, producing synchrotron radiation (Equation 1.25) in the downstream flow (Gaensler & Slane 2006).

Particles accelerated at the wind termination shock form a toroidal structure and some of the flow is collimated along the rotation axis, which can possibly contribute to jet formation (Bogovalov et al. 2005). The emission pattern from jets or ring-like structures and the large scale geometry of the PWN provide an indication of the pulsar's orientation. The emission structures in the post-shock and jet regions provide direct insight on particle acceleration, magnetic collimation and the magnetization properties of the PWN wind (Gaensler & Slane 2006).

Since pulsars are formed with a random space velocity, due to asymmetry in the SN explosion, with typical magnitude $400\text{-}500 \text{ km s}^{-1}$ (although sometimes reaching 1500 km s^{-1} (Arzoumanian et al. 2002)), while the SN blast wave first moves outward at a speed $> (5 - 10) \times 10^3 \text{ km s}^{-1}$, the pulsar is located near the SNR's center at early times. The pulsar wind has extremely high pressure with respect to the SN ejecta, so the PWN expands rapidly, moving supersonically and driving the PWN forward shock into the ejecta (Gaensler & Slane 2006).

In the spherically symmetric case, the PWN evolves as (Chevalier 1977; Gelfand et al. 2009)

$$R_{\text{PWN}} \approx 1.5 \dot{E}_0^{1/5} E_{\text{SN}}^{3/10} M_{\text{ej}}^{-1/2} t^{6/5}, \quad (1.27)$$

$$\approx 4.4 \times 10^{-3} \text{ pc} \left(\frac{\dot{E}_0}{10^{38} \text{ erg s}^{-1}} \right)^{1/5} \left(\frac{E_{\text{SN}}}{10^{51} \text{ erg}} \right)^{3/10} \left(\frac{M_{\text{ej}}}{10 M_{\odot}} \right)^{-1/2} \left(\frac{t}{10 \text{ yr}} \right)^{6/5} \quad (1.28)$$

where R_{PWN} is the radius of the PWN forward shock at time t , \dot{E}_0 is the spin-down luminosity at $t = 0$, and E_{SN} and M_{ej} are the kinetic energy and ejected mass, respectively, of the SN.

Since the PWN expansion velocity is steadily increasing, the PWN remains centered on the pulsar, and we expect to see a rapidly expanding SNR with a reasonably symmetric PWN near its center and a young pulsar near the center of the PWN. An example of this is pulsar J1833-1034, which powers the bright X-ray and radio PWN that lies at the center of SNR G21.5-0.9, which is estimated to be ~ 1000 years old (Camilo et al. 2006; Gupta et al. 2005; Matheson & Safi-Harb 2010).

The PWN is often elongated along the pulsar spin axis due to the higher equatorial pressure associated with the toroidal magnetic field (Begelman & Li 1992; Lyubarsky 2002; van der Swaluw 2003). As the PWN expands, Rayleigh-Taylor instabilities form due to the fast-moving relativistic fluid accelerating slower unshocked SN ejecta, producing dense, finger-like filamentary structures.

As the SN evolves into the Sedov-Taylor phase, the total energy becomes conserved as the ejecta cools adiabatically and is partitioned almost equally between kinetic and thermal contributions (Truelove & McKee 1999). The interaction between the SNR and surrounding medium is now more complicated, with a SN forward shock which compresses and heats ambient gas, and a reverse shock that decelerates the ejecta. The two shocks are separated by a contact discontinuity where instabilities can form. The reverse shock initially propagates outward behind the SN forward shock, but eventually begins to move inward.

In the absence of a pulsar and PWN, the reverse shock reaches the SNR center at (Reynolds & Chevalier 1984)

$$t_{\text{RS}} = 7 \text{ kyr} \left(\frac{M_{\text{ej}}}{10 M_{\odot}} \right)^{5/6} \left(\frac{E_{\text{SN}}}{10^{51} \text{ erg}} \right)^{-1/2} \left(\frac{n_0}{1 \text{ cm}^{-3}} \right)^{-1/3} \quad (1.29)$$

where n_0 is the number density of the ambient gas, which is assumed to be constant. At this point, the interior of the SNR is filled entirely with shock-heated ejecta and can be described by a small set of simple self-similar equations (Cox 1972).

In the presence of a pulsar and PWN, the inwardly-propagating SN reverse shock collides with the outwardly-moving PWN forward shock after a time $t_{\text{coll}} < t_{\text{RS}}$, typically a few thousand years (Blondin et al. 2001; van der Swaluw et al. 2001). Even in the simplest case, with a stationary pulsar, isotropic wind, and spherical SNR, the evolution is complicated. The reverse shock compresses the PWN by a large factor, increasing the magnetic pressure inside the PWN and causing the PWN to expand again. The sudden magnetic field increase during compression burns off the highest energy electrons (Blondin et al. 2001; Bucciantini et al. 2003; Reynolds & Chevalier 1984), and the alternation of compression due to ram pressure from the shocked ejecta and expansion due to the magnetic pressure inside the PWN cause the nebula to reverberate on a timescale of a few thousand years. The compression of the PWN produces Rayleigh-Taylor instabilities, which can produce a chaotic, filamentary structure (Blondin et al. 2001; Chevalier 1998).

At later times, the motion of the pulsar carries it away from the SNR center and even outside the PWN. This leads at first to a complicated three-dimensional interaction, causing large asymmetries and distortions in the shape of the PWN (Chevalier 1998; van der Swaluw et al. 2004), then a new, smaller PWN around its current position (van der Swaluw et al. 2004). The motion of the pulsar eventually becomes supersonic, and drives a bow shock through the SNR interior (Chevalier 1998; Van Der Swaluw et al. 1998). The ram pressure from the pulsar motion confines the new PWN to within 1 pc, and the PWN no longer expands steadily with time.

Eventually the pulsar will spin down to the point where their energy output is insufficient to power an observable synchrotron nebula. At this stage, a pulsar is

surrounded by a static or slowly expanding cavity of relativistic material with a radius $\ll 1$ pc confined by the thermal pressure of the interstellar medium (Arons 1983; Blandford et al. 1973); deep searches only recently detected these pulsar bow shock nebulae (Rangelov et al. 2016, 2017).

1.3.3 Magnetars

Most pulsars have a dipole field strength of $\sim 10^{12}$ G, but a small fraction have fields as high as $\sim 10^{15}$ G; these pulsars are commonly known as magnetars. Quantum electrodynamic effects can become important around and above (Duncan 2001)

$$B_{\text{crit}} = \frac{m_e^2 c^3}{e \hbar} = 4.413 \times 10^{13} \text{ G}, \quad (1.30)$$

where the nonrelativistic Landau energy $\hbar e B / m_e c$ is equal to the electron rest energy $m_e c^2$ (den Hartog 2008; Landau 1957a,b; Thompson & Duncan 2001). Such effects include the vacuum becoming anisotropic and birefringent (den Hartog 2008; Mészáros & Ventura 1979), vacuum polarization (Mészáros & Ventura 1979; Pavlov & Shibano 1979), magnetic lensing (den Hartog 2008), and photon splitting (Adler 1971; Harding et al. 1997). Atoms in magnetic fields of this strength are stretched into long, thin cylinders (Harding & Lai 2006; Lai 2001; Thirumalai & Heyl 2009).

Magnetars were historically found as two different types of objects: the Soft Gamma-Ray Repeaters (SGRs), which were first found due to their repeated bursts in the soft gamma-ray band, and Anomalous X-ray Pulsars (AXPs), which have a persistent x-ray flux higher than predicted by dipolar spin-down. These types of objects both have very long ($P \sim 5\text{-}12$ s) rotation periods and spin down very rapidly ($\dot{P} \sim 10^{-10}$ s s $^{-1}$); these properties give very large magnetic fields (Equation 1.20) and find a natural interpretation within the magnetar model. The first detection of pulsations in the persistent/quiescent emission from SGR 1806-20 was made in 1998 (Kouveliotou et al. 1998), which included measurement of the period and period derivative. The persistent x-ray flux was more than two orders of magnitude higher than the available spin-down energy (Kouveliotou et al. 1998; Rosswog & Brüggen 2007) and the period and period derivative indicate a magnetic field of $\sim 8 \times 10^{14}$ G. Because these phenomena were predicted by the magnetar model (Thompson & Duncan 1995, 1996), this was when astronomers became convinced that SGRs are indeed magnetars (den Hartog 2008).

It is not currently known how such high magnetic fields are generated, but there are several possible mechanisms. The fossil field, magnetohydrodynamic dynamo, and collective magnetism mechanisms from Section 1.2.1 can all generate magnetar fields. Other possibilities include differential rotation with a magnetic instability (Akiyama et al. 2003; Spruit 2002) and vector spin alignment in a pion-condensated quark matter core (Bhattacharya & Soni 2007). These mechanisms are not of great importance to explaining the observed characteristics, but it is clear that it is possible to create neutron stars with magnetar fields.

There are several possible mechanisms involved in transporting magnetic energy from the magnetar core to its surface: Ohmic dissipation, ambipolar diffusion, and Hall drift (Goldreich & Reisenegger 1992). The dissipation timescale for Ohmic decay in the core is too long to significantly contribute to energy transportation in magnetars. Ambipolar diffusion is capable of transporting energy from the core to lower crust, while Hall drift generates turbulence in the crust which enhances the local rate of Ohmic dissipation. The force due to the magnetic field, affected by Hall drift, can

rupture the magnetar crust and give rise to a glitch or flare (Goldreich & Reisenegger 1992; Pons & Geppert 2007)

Thompson et al. (2002) studied the effects of the internal twisted toroidal magnetic field on the external poloidal field, and find that the internal field is strong enough to twist the outer one. This twisting induces currents that produce both thermal and non-thermal persistent emission, and causes extra magnetospheric current to cross the light cylinder, which increases the spin-down torque of the neutron star. This is sufficient to power magnetars for several thousand years (Durant & van Kerkwijk 2006), and also why no older magnetars are discovered. The absence of this internal energy is thought to be why high magnetic-field radio pulsars do not show similar behaviour to magnetars.

As of April 2016, there were 23 confirmed magnetars (11 Soft Gamma-ray Repeaters (SGRs) and 12 Anomalous X-ray Pulsars (AXPs)) and 6 candidates (4 SGRs and 2 AXPs) in existence (Olausen & Kaspi 2014).

SGR Flares

The first detection of an SGR was a flare from SGR 1806-20 on January 7, 1979 (Aptekar et al. 2001; Laros et al. 1986; Mazets & Golenetskii 1981). On March 5, 1979, the first SGR hyperflare was detected from SGR 0526-66, which is located in the Large Magellanic Cloud (Cline et al. 1982; Mazets et al. 1979). The hyperflare started with an extremely bright initial spike followed by a three minute decaying tail (Cline 1980). The magnetar's 8 s pulsations were clearly visible (Barat et al. 1983). The total energy emitted during the hyperflare was $\sim 5 \times 10^{44}$ erg (assuming isotropic emission) (den Hartog 2008). The same source was then observed to repeatedly emit smaller flares (Aptekar et al. 2001; Cline et al. 1982; Mazets & Golenetskii 1981; Usov 1996). SGR 1900+14 was discovered shortly afterwards when three flares were detected on March 24, 25, and 27, 1979 from the same location (Kouveliotou et al. 1993; Mazets et al. 1981). The detection of these flares were only a few years after the first extragalactic gamma-ray bursts were detected (den Hartog 2008; Klebesadel et al. 1973). SGR 0526-66, SGR 1900+14, and SGR 1806-20 all showed recurrent non-periodic flares over the next few years (Atteia et al. 1987; Golenetskii et al. 1984; Kouveliotou et al. 1987; Laros et al. 1987), which lead to the name Soft Gamma-ray Repeater.

There have been two more recent SGR hyperflares: one on August 27, 1998 from SGR 1900+14, which was similar to the first hyperflare from SGR 0526-66 (Feroci et al. 2001; Hurley et al. 1999), and one on December 27, 2004 from SGR 1806-20, which was more than two orders of magnitude larger than the previous two ($\sim 10^{47}$ erg) (Boggs et al. 2007; Borkowski et al. 2004; Götz et al. 2006; Palmer et al. 2005; Terasawa et al. 2005). The x-rays and gamma rays from both of these hyperflares ionized the Earth's upper atmosphere and caused the earth's ionosphere to contract to the same extent as it would from sunlight. These contractions changed the way radio waves propagated off the ionosphere (Campbell et al. 2005; Inan et al. 1999, 2007; Manda & Balasis 2006). Radio afterglows were also observed after both hyperflares (Cameron et al. 2005; Frail et al. 1999; Gaensler et al. 2005).

The small flares from SGRs show very irregular behavior. SGRs have short periods of bursting activity, where hundreds of bursts can be detected within several weeks, followed by years of inactivity (Aptekar et al. 2001; Göğüş et al. 2001; Woods et al. 1999). The energy distribution of these flares is a power-law ($dN/dE \propto E^{-5/3}$) (Cheng et al. 1996), much like the Gutenberg-Richter law for earthquakes (Gutenberg & Richter 1956). Other similarities exist between earthquakes, solar flares, and SGR flares; they all have comparable waiting times and none of them show a correlation

between energy and waiting time (den Hartog 2008; Göğüş et al. 1999, 2000; Thompson & Duncan 2001).

Because of the similarity to earthquakes, a "magnetar-quake" is regarded as a plausible mechanism for producing flares and hyperflares (Pons & Geppert 2007; Thompson & Duncan 2001). An estimate of the magnetic field energy gives $(U_B V_{\text{NS}} \sim 10^{48}$ erg, while the energy released in the SGR 1806-20 hyperflare was $\sim 10^{46}$ erg, so the energy released in the burst is only a fraction of the magnetic energy inside the star, and both theory and observations of magnetar giant flares indicate that the magnetic energy can be converted to high energy photon emission (Elenbaas et al. 2017; Thompson & Duncan 1995). The restructuring of the magnetic field that causes the initial spike also radiates a hot, optically thick, electron-positron pair-plasma fireball that is trapped near the magnetar by closed magnetic field loops. This fireball is forced to rotate with the star and slowly evaporates by leaking photons, which powers the decaying tail (Duncan 2004; Paczynski 1992; Rosswog & Brüggen 2007; Thompson & Duncan 2001).

1.4 Possible Pulsar-Driven Transients

Although supernova astronomy is thousands of years old, the advances in multi-wavelength (and now multimessenger, with the detection of gravitational waves from LIGO) astronomy over the past 50 years have led to the discovery of many different high-energy transients, including Gamma-ray Bursts (GRBs) and Fast Radio Bursts (FRBs). Improvements in optical telescopes have also led to the discovery of more luminous subclasses of supernovae, such as Hypernovae (HNe) and Superluminous Supernovae (SLSNe). Scientists have long struggled to determine the energy sources and emission mechanisms for these transients, and even though models have been developed, there is still no clear evidence from observations to support them.

Many of these models involve the death of a massive star (Bisnovatyi-Kogan 1971; Kardashev 1964; Ostriker & Gunn 1971; Shklovskii 1973, 1976). The collapsar model, where a fast rotating star with a 5-15 M_{\odot} core collapses into a black hole and the fall-back accretion onto the black hole produces relativistic jets (MacFadyen & Woosley 1999), is often used to explain HNe and GRBs (Fujimoto et al. 2008; MacFadyen et al. 2001). The pair-instability model, where pair production in stars with masses 130-250 M_{\odot} temporarily reduces the internal pressure supporting the star against gravitational collapse and greatly accelerates nuclear burning, causing a runaway thermonuclear explosion that leaves no remnant (Fraley 1968; Kasen et al. 2011), is often used to explain SLSNe (Cooke et al. 2012; Gal-Yam et al. 2009). Also, a circumstellar shock between SN ejecta and dense nebular material or dust close to the star is thought to be the power source for hydrogen-rich SLSNe (Gal-Yam & Leonard 2009; Smith et al. 2008).

However, a model that can explain a wide variety of transients is the pulsar-driven model (e.g., Dai et al. 2016b; Inserra et al. 2013; Metzger et al. 2015; Nicholl et al. 2014, 2016b; Pastorello et al. 2010; Quimby et al. 2011; Wang et al. 2015). In this model, the spin-down energy of a newborn pulsar is injected into the ejecta of a supernova; this energy is thermalized and remitted as quasi-thermal optical radiation. A sufficiently asymmetrical explosion can also lead to jets around the pulsar poles, which can either be absorbed by the ejecta or punch a hole right through it. The diversity of possible explosions in this model follows from the diversity of possible neutron stars and environments: there is a large possible range in possible spin periods and magnetic fields, there could be a binary companion or accretion disk, the envelope can vary vastly in

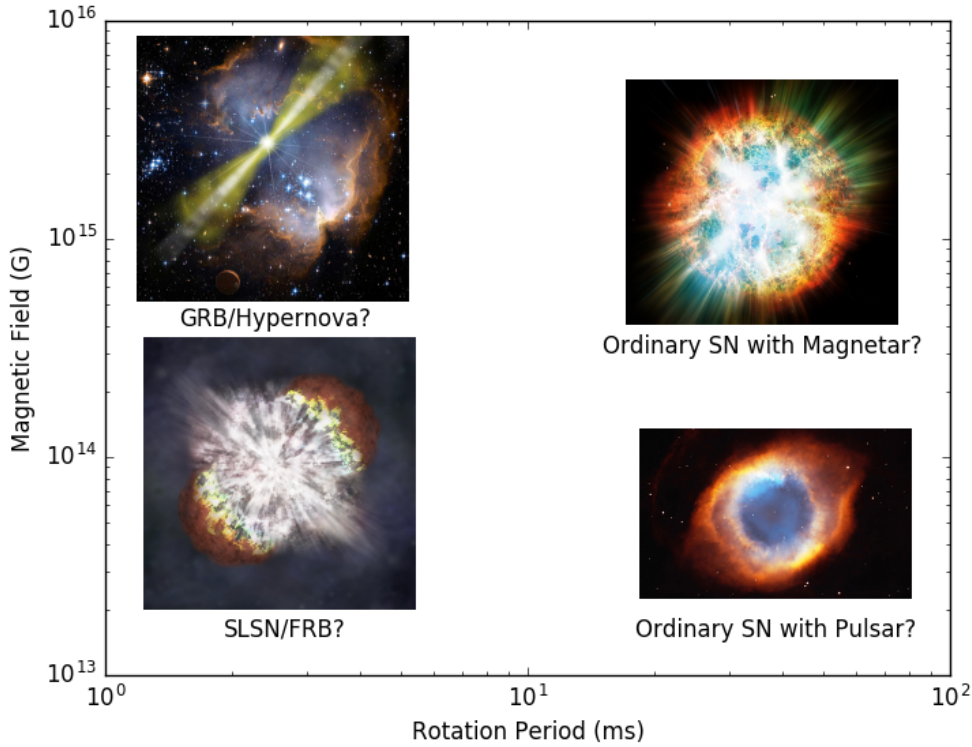


FIGURE 1.1: The diversity of transients caused by pulsar formation or young pulsars, and their approximate dependence on the initial spin period and dipole magnetic field of the pulsar. Pulsars with ms rotation periods and $\sim 10^{13}$ G magnetic fields are thought to power SLSNe during their formation, and power FRBs years or decades after their birth (Connor et al. 2016; Cordes & Wasserman 2016; Lyubarsky 2014; Lyutikov et al. 2016; Popov & Postnov 2010a). Pulsars with ms rotation periods and $\sim 10^{15}$ G magnetic fields are thought to power HNe and GRBs during their formation (Burrows et al. 2007a; Troja et al. 2007; Zhang & Mészáros 2001). Pulsars with longer rotation periods are thought to power some ordinary Type Ibc SNe, with those with $\sim 10^{15}$ G magnetic fields having a central magnetar and those with smaller field having a central pulsar.

mass and composition, and the pulsar could have a magnetar-like twisted poloidal magnetic field.

Although the pulsar-driven model can explain all these different transients, no observational finding has been able to conclusively validate the pulsar-driven scenario so far (Kashiyama et al. 2016). The quasi-thermal optical radiation produced in HNe and SLSNe can be explained by a number of different central engines. The question is, how can we discriminate newborn pulsar engines for each type of transient by using ongoing and upcoming multi-messenger observations (Kashiyama et al. 2016).

Figure 1.1 shows a number of different transients that are thought to be powered by newborn or young pulsars, and the expected initial spin period and dipole magnetic field of the pulsar engine. We describe the different transients individually in the rest of the section.

1.4.1 Gamma-Ray Bursts (GRBs) and Hypernovae (HNe)

Gamma-ray bursts were discovered in 1967 by the Vela 3 and Vela 4 satellites, which were originally launched to detect nuclear weapons tests in space (Katz 2002; Schilling 2002). The operation of four satellites made it possible to localize the burst to a compact region of space. Vela 5 and Vela 6 were launched in 1969 and 1970 respectively, and the six satellites were able to detect and trace 16 GRBs in the next three years, leading up to the publication of the first GRB observations by Klebesadel et al. (1973).

By 1978, there were 11 satellites, together known as the Inter-Planetary Network (IPN), in orbit around the Earth, Venus, and the Sun, attempting to detect and localize GRBs. These satellites could pinpoint GRBs to within a arcminutes, but this was not enough to detect a counterpart in any other wavelength band. Three gamma-ray satellites were launched in the 1990s and early 2000s: the Burst and Transient Source Explorer (BATSE) in 1991, BeppoSAX in 1996, and the High Energy Transient Explorer 2 (HETE2) in 2000 (The first HETE lost radio contact with the Earth after one day).

The launch of BATSE was able to show the isotropy of GRBs (Meegan et al. 1992), confirming them as extragalactic, as well as two distinct categories, short GRBs (SGRBs) with periods less than two seconds and long GRBs (LGRBs) with periods greater than two seconds (Kouveliotou et al. 1993). These categories are broad with significant overlap, and other categories, such as ultra-long GRBs (Boër et al. 2015; Levan et al. 2014; Virgili et al. 2013), intermediate GRBs (Horváth et al. 2006; Mukherjee et al. 1998), and low-luminosity GRBs (LL-GRBs) (Virgili et al. 2009), have also been suggested based on theoretical and observational grounds (Chattopadhyay et al. 2007; Hakkila et al. 2003; Horváth 1998).

The best hope for the detection of a counterpart would rely on the localization of a GRB afterglow at lower wavelengths (Fishman & Meegan 1995; Paczynski & Rhoads 1993). In February 1997, BeppoSAX discovered GRB 970228, a gamma-ray burst with fading x-ray emission (Costa et al. 1997), and optical telescopes were able to detect a fading counterpart as well (van Paradijs et al. 1997). With a location identified, later deep observations were able to identify a distant, faint host galaxy for the GRB; the discovery of the distance scale and environments where GRBs occur revolutionized the study of GRBs (Frontera & Piro 1999).

Although radio emission from GRBs was originally thought to be too faint to be detectable (Meszaros & Rees 1993), the afterglow of GRB 970508 was detected by the Very Large Array (VLA) (Frail et al. 1997). This observation determined that the source of radio waves had expanded almost at the speed of light. There was also a very complete spectrum for this event, which allowed Wijers & Galama (1999) to determine the total energy of the burst (assuming isotropic emission) and particle density of the surrounding medium as 3×10^{52} erg and 30 000 particles per cubic meter respectively. Although they did not consider their results to be considered incredibly reliable, they were able to show that it would be possible, in principle, to determine the physical characteristics of GRBs based on their spectra (Schilling 2002).

The next important GRB was GRB 971214, which would have emitted 3×10^{53} erg if isotropic. This amount of energy was higher than predicted by any model and would have been the most energetic explosion observed since the Big Bang, which earned it the nickname "Big Bang 2". After this, astronomers concluded that GRBs were highly focused explosions, with most of the explosion energy collimated into a narrow jet (Abdo et al. 2009; Rykoff et al. 2009). The approximate width of the jet can be estimated by observing the achromatic "jet breaks" in afterglow light curves, where the afterglow decays rapidly as the jet slows and can no longer beam its radiation effectively (Burrows et al. 2006b; Frail et al. 2001; Sari et al. 1999). This implies that for

every burst observed on earth, several hundred occur which are not observed because their beams are not pointed towards earth (Schilling 2002).

GRBs were predicted to be associated with core-collapse supernovae (Paczynski 1997), and in 1998, the first supernova to be coincident with a gamma-ray burst, SN1998bw, was discovered (Galama et al. 1998; Vreeswijk et al. 2000), although it was never confirmed that the events were related. This type of supernova came to be known as a hypernova (HN), which has an explosion energy too high for only neutrino deposition, but is only slightly more luminous than a regular supernova (Iwamoto et al. 1998). Hypernovae are typically broad-lined Type Ic supernovae (Woosley et al. 1999), although some hydrogen rich supernovae share similar energetic properties (Terreran et al. 2017). In 2003, the connection was confirmed with the detection of GRB 030329 in gamma-ray (Vanderspek et al. 2003), x-ray (Marshall & Swank 2003), optical (Peterson & Price 2003), and radio (Berger et al. 2003), and subsequent detection of SN2003dh in the afterglow (Matheson et al. 2003; Stanek et al. 2003), with spectral features similar to previous hypernovae (Iwamoto et al. 2000; Patat et al. 2001).

The central engine for SGRBs has long been thought to be binary neutron star mergers (Blinnikov et al. 1984; Eichler et al. 1989; Nakar 2007; Narayan et al. 1992; Paczynski 1986, 1991) due to their lack of association with star-forming regions and galaxies (Bloom et al. 2006; Gehrels et al. 2005; Prochaska et al. 2006), and were hypothesized to produce also optical emission, known as a kilonova (Tanvir et al. 2013), due to the decay of heavy radioactive elements (Berger et al. 2013; Metzger et al. 2010), as well as radio emission (Hurley et al. 2002; Piran 2004) and gravitational waves (Cutler & Flanagan 1994; Flanagan & Hughes 1998; Nakar 2007; Phinney 1991). This was recently confirmed by the multimessenger observations of GW170817 and GRB 170817A (Abbott et al. 2017c), as it produced a gravitational wave signal (Abbott et al. 2017b), short- to intermediate-duration GRB (Abbott et al. 2017a), UV/optical/ infrared kilonova (Cowperthwaite et al. 2017; Nicholl et al. 2017e; Smartt et al. 2017; Valenti et al. 2017), and radio emission (Alexander et al. 2017; Hallinan et al. 2017). This event appears to show cocoon-like shock breakout behaviour (Gottlieb et al. 2017; Mooley et al. 2017; Piro & Kollmeier 2017), as detailed below, although this is still a topic of intense discussion (Bromberg et al. 2017; Ioka & Nakamura 2017; Kisaka et al. 2017; Lamb & Kobayashi 2017). Since there has only been one detection and it does not resemble a "typical" short GRB in terms of its luminosity and spectra (Bégué et al. 2017; Horvath et al. 2017; Palmese et al. 2017), there is now much discussion of the possibility of multiple types of SGRB progenitors, including magnetar hyperflares from nearby galaxies (Frederiks et al. 2008; Hurley et al. 2005; Tong & Yu 2017), black hole-neutron star mergers (Mochkovitch et al. 1993; Nakar 2007; Narayan et al. 1992), or even certain types of black hole-black hole mergers (de Mink & King 2017; Loeb 2016).

LGRBs are unambiguously associated with star formation and the deaths of massive stars (Pontzen et al. 2010; Woosley & Bloom 2006), but the central engine is yet unclear, and could be a collapsar (Fujimoto et al. 2008; Gendre et al. 2013; Ioka et al. 2016; MacFadyen & Woosley 1999; MacFadyen et al. 2001), tidal disruption event (Bloom et al. 2011; Ioka et al. 2016; Krolik & Piran 2011; Levan et al. 2011), or newborn magnetar (Bucciantini 2012; Greiner et al. 2015; Ioka et al. 2016; Thompson et al. 2004; Usov 1992; Wheeler et al. 2000), among other possibilities (Cline 1996; MacFadyen et al. 2006; Vietri & Stella 1998; Winterberg 2001). In the millisecond magnetar model, the rotational energy of $\sim 10^{52}$ erg is extracted in ~ 100 s with a field of $\sim 10^{15}$ G.

During magnetar formation, the proto-NS cools via neutrino emission in the thermal Kelvin-Helmholtz timescale $\tau_{\text{KH}} \sim 10 - 100$ s (Pons et al. 1999). About 1 s after

the core bounce, a neutrino driven wind develops due to a density decrease around the proto-NS (Thompson et al. 2001). For regular pulsars, this wind carries little energy (Thompson et al. 2001), but for magnetars, the wind is magnetocentrifugally accelerated and far more energetic, eventually reaching relativistic speeds (Bucciantini et al. 2006; Thompson et al. 2004). In the first ~ 1 s, the wind has typical thermal speeds of $\sim 0.1c$. In the next ~ 10 s, the proto-NS relaxes to a radius of around 20 km and begins to spin down, and the magnetization parameter σ_B increases from ~ 1 to ~ 10 ; the neutrinos become relativistic, but the bulk of the neutrinos are still confined within the proto-NS. After most of the neutrinos break out of the proto-NS, they start to accelerate in the stellar material and σ_B increases to $\sim 10^2 - 10^3$. These neutrinos ablate baryons from the surface of the NS as they break out, and these baryons are accelerated by the magnetar fields and collimated into a jet by a compressed toroidal magnetic field in the nascent magnetar wind nebula that expands in the polar directions (Del Zanna et al. 2004; Komissarov & Lyubarsky 2004) as well as by the cocoon mechanism described below (Bromberg & Tchekhovskoy 2016; Bromberg et al. 2017); the toroidal magnetic field collimation process has been shown to work under various assumptions (Bucciantini et al. 2007, 2008, 2009; Komissarov & Barkov 2007) and is sometimes known as the "tube of toothpaste" effect (Bucciantini 2012), but can lead to magnetic field shearing (Alves et al. 2014). After ~ 100 s, the neutrino luminosity drops below the threshold to drive a baryon-loaded wind, which is replaced by a leptonic wind once the density in the magnetosphere drops below the threshold for pair production (Metzger et al. 2011). The magnetized wind can also drive a shock into the expanding SN ejecta, depositing up to $\sim 10^{52}$ erg into the ejecta. The fraction of energy that escapes with the GRB and the fraction that is deposited in the ejecta is still unknown, with some astronomers claiming most of the energy escapes (Bucciantini 2012; Bucciantini et al. 2009; Komissarov & Barkov 2007) and some claiming most goes into the ejecta (Thompson et al. 2004).

The jets for GRBs need to break through the ejecta surrounding the central engine in most models, even those for SGRBs. Once this highly-relativistic jet collides with the non-relativistic ejecta, its advance is slowed and most of its energy during this phase is deposited into a surrounding cocoon (Ramirez-Ruiz et al. 2002; Waxman & Mészáros 2003; Zhang et al. 2003). The jet propagates through the dense ejecta and mixes with it, lowering the kinetic energy of the jet and increasing the energy of the cocoon. If the ejecta is thin enough, the jet will punch through the ejecta and propagate with relativistic speed, leading to a collimated gamma-ray burst with a small amount of off-axis emission due to the cocoon. If the ejecta is thick, the jet and ejecta will be thoroughly mixed and break through the ejecta as a mildly relativistic cocoon fireball, and emit highly luminous optical, UV, and x-ray emission with a beaming angle of $\sim 10 - 30^\circ$ (De Colle et al. 2017; Mizuta & Ioka 2013; Nakar & Piran 2017).

1.4.2 Superluminous Supernovae (SLSNe)

SLSNe have only been discovered recently, with the first one being SN2005ap 12 years ago (Quimby et al. 2007); to date there have only been around 50 confirmed SLSNe. Although they are extremely rare, accounting for 1 out of every 10^3-10^4 supernovae (Quimby et al. 2011), they are the most luminous optical/UV transients associated with the deaths of massive stars, being generally around 100 times brighter than regular supernovae. While Type II SLSNe show narrow spectroscopic features, like Type II SN, consistent with strong interaction with the circumstellar medium, Type I SLSNe do not exhibit these features, have blue continua at maximum light, a distinctive feature due to [O II] at early epochs, and at about 30 days after peak, they are

spectroscopically similar to normal or broad-lined SNe Ic at peak luminosity (Inserra et al. 2016a; Pastorello et al. 2010). They are found predominantly in low metallicity dwarf galaxies with high rates of specific star formation (Lunnan et al. 2014; Vreeswijk et al. 2014) and extreme emission lines (Leloudas et al. 2015), although this is not always the case (Chen et al. 2017).

Early time bumps (pre-peak, double peaks, or excess emission), which can be explained by shock-cooling or CSM-interaction models (Chatzopoulos et al. 2012; Nakar & Sari 2010; Piro 2015; Rabinak & Waxman 2011), have been observed for SLSNe such as SN2006oz (Leloudas et al. 2012), LSQ14bdq (Nicholl et al. 2015), PTF12dam and iPTF13dcc (Vreeswijk et al. 2017), and DES14X3tza (Smith et al. 2016), and may be common among SLSNe (Nicholl & Smartt 2016). Late-time (post-peak) bumps have also been observed in a few cases, such as SN2007bi (Gal-Yam et al. 2009) iPTF13ehe (Yan et al. 2015), PS1-14bj (Lunnan et al. 2016), and SN2015bn (Nicholl et al. 2016a). Undulations in late-time decay have been observed in a few slowly declining SLSNe (Inserra et al. 2017). Late emergence of hydrogen emission has been detected in a few cases, which can be explained by substantial mass loss shortly before the progenitors exploded (Yan et al. 2015, 2017b). Liu et al. (2017) showed that these light curves could be explained by a multiple-shell CSM interaction model. The diversity observed so far in H-poor SLSNe seem to indicate that multiple processes may contribute to powering their light curves (De Cia et al. 2017).

These SNe are too luminous to be powered by the neutrino mechanism detailed in Section 1.2.1 - magnetohydrodynamic models usually require these supernovae to have an explosion energy of $\sim 10^{52}$ erg, while the limit due to neutrino deposition is only $\sim 2 \times 10^{51}$ erg because of the neutrino's small cross section (Janka 2012; Müller 2017; Terreran et al. 2017). Also, bright supernovae usually indicate that a large amount of ^{56}Ni was synthesized in the explosion, as its radioactive decay serves to keep the ejecta hot during its early rapid expansion. However, late-time observations suggest that the M_{Ni} is much lower than required to match the SLSN luminosity (Chen et al. 2013; Inserra et al. 2013; Pastorello et al. 2010; Quimby et al. 2011), and estimated ejecta masses are much lower than the necessary core mass to synthesize a large amount of ^{56}Ni (Moriya et al. 2010; Nicholl et al. 2015). These mandate the need for a central engine or other power source; hydrogen-rich SLSN are likely powered by SN ejecta and the hydrogen-rich envelope (e.g., Chatzopoulos et al. 2012; Chevalier & Fransson 1994; Chevalier & Irwin 2011; Chugai & Danziger 1994; Inserra et al. 2016b; Ofek et al. 2013; Smith & McCray 2007), while hydrogen-poor SLSN are likely powered by central engine, possibly a fast-rotating pulsar.

Although most SLSN models are spherically symmetric, a pulsar-powered SN should have some intrinsic asymmetry characterized by a dominant polarization angle as observed for other types of stripped-envelope SNe (e.g., Maund et al. 2007; Tanaka et al. 2012; Wang et al. 2001). A strong magnetic field could lead to larger asymmetries than normal stripped-envelope SNe, and detection of this asymmetry could suggest magnetar energy injection as the source. Asymmetry in the ejecta could hide signatures of hydrogen or helium in SLSN-I spectra (Kozyreva & Blinnikov 2015), as well as ionization (De Cia et al. 2017; Mazzali et al. 2016). Axisymmetric ejecta could be the consequence of aspherical energy and momentum production during the explosion due to magnetohydrodynamic jets (Khokhlov et al. 1999), magnetoturbulence (Mösta et al. 2014), accretion flow around the pulsar (Chevalier 1989), asymmetric neutrino emission (Müller 2015; Wheeler & Akiyama 2010), clumping of the ejecta material, or a combination of these (Inserra et al. 2016a).

In the pulsar-driven model for SLSNe, the engine timescale in the SLSN must be comparable to the ejecta diffusion timescale (~ 100 days), so most of the energy in the

SLSN can go into quasi-thermal optical radiation rather than driving a jet (Metzger et al. 2015; Nicholl et al. 2016a). The large required injection energy also requires that pulsar initially rotates with a millisecond time scale (see Equation 1.14). From Equation 1.21, we find that these criteria prohibit pulsars with extremely high magnetic fields ($\geq 10^{15}$ G) from being the possible SLSN progenitor, and require the field to be around $10^{13} - 10^{14}$ G.

1.4.3 Fast Radio Bursts (FRBs)

FRBs, which are luminous, coherent bursts of radio emission, were discovered in 2007 using the Parkes Radio Telescope (Lorimer et al. 2007), but astronomers were initially skeptical until a population was found using the Arecibo and Green Bank Telescopes (Spitler et al. 2014; Thornton et al. 2013). FRBs are typically ≤ 1 ms, and can not be temporally resolved by most receivers (Katz 2016). To date, 29 burst sources have been found ¹ (Petroff et al. 2016); 28 of which appear to have been one time events, while one (FRB 121102) has been seen to repeat over 150 times (Gajjar et al. 2017; Mann 2017; Scholz et al. 2016; Spitler et al. 2016). The dispersion measure

$$DM = \int_{\text{Source}}^{\text{Object}} n_e dl \quad (1.31)$$

which causes a frequency-dependent time delay in the signal, can be used to roughly estimate the source distance; the DM for FRBs was found to be too high to come from a galactic source (Bannister et al. 2017), which established the bursts as being extragalactic (Caleb et al. 2017). This dispersion may be partially due to a dense magnetic plasma (Masui et al. 2015) or PWN surrounding the source (Kashiyama & Murase 2017); in the case of the PWN, the density puts a lower limit of the age of the source (Kashiyama & Murase 2017). In 2015, an FRB was observed in real-time and a circular polarization of $21 \pm 7\%$ was measured (Petroff et al. 2015).

The all-sky rate of FRBs is estimated to be 10 000 per day (Spitler et al. 2014), but until recently there was no localization or association with other sources. However, recent observations of the repeating FRB 121102 led to the localization of its host galaxy at $z = 0.193$ and the discovery of a persistent radio counterpart, which was seen by VLA and the European Very Long Baseline Interferometry (VLBI) Network (Chatterjee et al. 2017; Marcote et al. 2017; Tendulkar et al. 2017). The source is coincident with the star forming region in the galaxy (Bassa et al. 2017), which suggests a possible connection FRBs and the deaths of massive stars, similar to SNe and GRBs (DeLaunay et al. 2016; Deng & Zhang 2014; Zhang 2014).

The nature of FRBs is still unknown due to their isolated nature and there is no generally accepted explanation, but there have been many models proposed. Some of these models involve cataclysmic events, such as collisions and mergers of compact massive objects such as white dwarves, neutron stars, or black holes (Kashiyama et al. 2013; Ravi & Lasky 2014; Totani 2013; Zhang 2016), blitzars (Falcke & Rezzolla 2014; Thornton et al. 2013), the dark matter-induced collapse of pulsars (Bramante & Linden 2014; Fuller & Ott 2015), quark novae (Shand et al. 2016), and the collapse of the magnetospheres of Kerr-Newman black holes (Barrau et al. 2014; Liu et al. 2016; Zhang 2016). Other models involve non-cataclysmic events, such as giant neutron star pulses (Connor et al. 2016; Cordes & Wasserman 2016; Lyutikov et al. 2016), magnetar hyperflares (Champion et al. 2016; Kulkarni et al. 2015; Lyubarsky 2014; Popov & Postnov 2010b), intermittent Roche lobe overflow in a neutron star-white dwarf

¹<http://frbcat.org/>

binary (Gu et al. 2016), or pulsars interacting with planets (Mottez & Zarka 2014), asteroids (Dai et al. 2016a), or comets (Geng & Huang 2015). They have even been proposed to come from extragalactic civilizations (Lingam & Loeb 2017). Since the discovery of the repeating FRB, we know that not all FRBs can be caused by cataclysmic events. However, due to there being only one repeating source detected, which has over 100 bursts, it has been proposed that the repeating burst might be a separate subclass of FRB with a different physical mechanism entirely.

Magnetar hyperflares are predicted to emit energy in three channels: in thermal heat, in the bulk motion of plasma, and in energetic non-thermal particles (Lyutikov 2002). Solar flares are often accompanied by radio bursts (Bastian et al. 1998), which are signatures of electrons accelerated along coronal magnetic field lines that cause electrostatic plasma turbulence and the subsequent collision of plasma waves (Lyutikov 2002); magnetars are predicted to exhibit similar behaviour. However, the radio non-detection of the 2004 SGR 1806-20 hyperflare gives a fluence limit that is inconsistent with all but one of the first fifteen FRBs (Tendulkar et al. 2016); however, due to the variability in magnetar and FRB properties and possible dependence on the circum-magnetar medium, the hyperflare hypothesis has yet to be discarded by the community.

The giant pulses arise from young neutron stars, and arise in an outer magnetosphere acceleration gap (Cheng et al. 1986b; Romani & Yadigaroglu 1995). Photon production is maintained by synchrotron radiation in the gap itself, where high magnetic fields enhance synchrotron emissivity and pair-production (Johnston & Romani 2004). This dense pair plasma promotes instabilities which create enhancements in particle coherence and thus the giant radio pulses (Johnston & Romani 2004). Giant pulses have been observed in 11 sources so far (Kuzmin 2007), most notably the Crab pulsar (Argyle & Gower 1972; Staelin & Reifenstein 1968) and millisecond pulsar PSR B1937+21 (Wolszczan et al. 1984). It is worth noting that these pulsars have extremely high magnetic fields at their light cylinder (Johnston & Romani 2004). The brightness temperature 5×10^{39} K, from a giant pulse from PSR B1937+21, is the highest observed brightness temperature in the Universe (Soglasnov et al. 2004). However, these pulses are extremely short (Hankins et al. 2003; Soglasnov et al. 2004), with one pulse from the Crab pulsar being only 2 ns long (Hankins et al. 2003). If the pulse duration t is interpreted as the maximum size of the emitting region $r < ct$, then 2 ns corresponds to a maximum size of only 60 cm, the smallest entity ever detected outside our solar system (Kuzmin 2007).

FRBs are expected to originate from similar young NS as SLSNe. The host galaxy of FRB 121102 is a low-metallicity dwarf galaxy with prominent emission lines, similar to SLSNe, and since the radio counterpart was found in the star forming region of the galaxy, it is likely that there is a link between stellar death and FRBs. This radio counterpart is consistent with a young PWN from a neutron star engine with sub-magnetar field strength and a millisecond initial rotation period (Kashiyama & Murase 2017), similar to SLSNe (see Figure 1.1 for the overlap). These properties strongly suggest that the FRB engine might be born in SLSN explosions, and motivates theoretical studies and follow-up observations of candidates for pulsar-driven supernovae, for which SLSNe are among the most interesting.

1.5 Thesis Overview

The combination of extreme gravity, magnetism, and density make neutron stars a unique laboratory to probe theories like general relativity, quantum electrodynamics, and nuclear physics, so it is important to understand their formation, life cycle, and diversity. Yet, the youngest pulsar astronomers know about is the Kes 75 pulsar, which is around 700 years old (Gotthelf et al. 2000). A central engine, like a fast spinning newborn pulsar or a black hole accretion disk, is thought to power many transients across the electromagnetic spectrum, including SLSNe, HNe, and GRBs. Also, the recent localization of the source for the repeating FRB 121102 with a host galaxy similar to observed SLSN hosts makes it likely that the FRB engine might be born in SLSN explosions. We aim to elucidate the connection between pulsars and transients by predicting the detectability of multiple types of non-thermal signals unique to the pulsar engine and doing follow-up observations on promising candidates to verify or refute these predictions and further our understanding of both compact objects and the luminous transients they may cause. We also want to detect and study newborn pulsars, only a few years after their birth, as new insights in nuclear physics, condensed matter, plasma physics, quantum mechanics, and general relativity could come from identifying, modelling, and observing nascent neutron stars.

In Chapter 2, the models used to derive the results in later chapters are introduced and overviewed. Descriptions of the qualitative behaviours and parameter dependencies of the models are left to those later chapters, and instead focus is placed on the physical motivation and mathematical formulation of each model. We describe the models for quasi-thermal and non-thermal emission from SLSNe, including the effects of spin-down; radioactivity; PWN dynamics; electron cooling, acceleration, and pair production; quantum effects; and broadband absorption and attenuation. We also describe models for dust formation due to nucleation and subsequent growth, dust sublimation via PWN emission, and thermal re-emission of absorbed emission from dust grains of arbitrary composition within the ejecta as it expands and cools.

There have been previous arguments that Type-I SLSNe are powered by central engines which inject energy for a long period of time after the core-collapse of the progenitor star. A popular hypothesis is that the engine is a rapidly-rotating pulsar with a magnetic field between $10^{13} - 10^{15}$ G, but quasi-thermal optical emission can not differentiate this from other possible engines. Murase et al. (2016) proposed that radio/submm emission from non-thermal positron-electron pairs in the newborn PWN can be used to identify and characterize pulsars in the supernovae they power. In Chapter 3, we calculate the PWN emission from six bright newborn SLSN-I remnants, assuming that they are pulsar-driven, and examine the constraints placed by radio and submm emission. We find that the Atacama Large Millimeter/submillimetre Array (ALMA) can detect the submm PWN emission from most of them in a few years after the explosion, while the Jansky Very Large Array (VLA) can detect the radio PWN emission from a few of them in a few decades. Follow-up observations could help solve the parameter degeneracy problem in the pulsar-powered SN model and could give clues about young neutron stars scenarios for SLSNe-I and FRBs.

In Chapter 4, we introduce and discuss the preliminary results of a study about an indirect detection method for young PWN: re-emission from dust grains. We use a steady-state model to study the growth of dust grains in the ejecta of a pulsar-powered supernova, and examine sublimation of smaller grains and re-emission from larger grains due to PWN emission. We consider dust compositions based on those expected for a variety of progenitors of Type Ic, Ib, and IIb supernovae, including SLSNe, and calculate the properties of C, MgSiO_3 , and MgO grains in their ejecta.

We find that dust is always optically thick from a few months after formation, and re-emits at a temperature between 1500-2000 K. For the cases of SN2015bn and SN2016ard, which we propose to study in Chapter 5, we find that the dust emission is not detectable at all, although this may be due to an unphysical part of our model. Apart from fixing this, the next steps include realistically calculating absorption, calculating emission using more parameter sets, and diagnosing our model to test its accuracy.

Chapter 5 is based on our Cycle 5 proposal to observe SN2015bn and SN2016ard, two bright, recent SLSNe, with the Atacama Large Millimeter/submillimetre Array (ALMA), in hopes of detecting the PWN emission predicted in Chapter 3. These observations have the potential to provide hints on the origin of super-luminous supernovae (SLSNe) that may be applicable to other interesting high-energy phenomena, such as Fast Radio Bursts (FRBs). However, these observations may not unambiguously confirm the magnetar model, even if synchrotron radiation is detected, and it is not obvious which system parameters would be constrained from the ALMA in a model-independent way. Nevertheless, these observations are a critical test for the pulsar-driven model, as this is the first attempt at detecting early submm PWN emission, and a successful detection would be strong evidence for the model as well as detection of the youngest known pulsar to date; studying this system would give a lot of insight into early pulsar evolution and its impact on the surrounding SN. This proposal was accepted with B priority, and the observations should take place this winter.

Finally, Chapter 6 will give the author's concluding remarks on the outlook of the SLSN and pulsar-driven SN community.

Chapter 2

Theory and Models

In this chapter, we overview the models used to derive the results in Chapters 3 and 4. We leave descriptions of the qualitative behaviours and parameter dependencies of the models to later chapters, and instead focus on the physical motivation and mathematical formulation of each model. We begin by describing the models for quasi-thermal and non-thermal emission from SLSNe in Section 2.1, and then describe models for dust formation, sublimation, and emission in Section 2.2. Throughout this chapter, we use the notation $Q = 10^x Q_x$ in CGS units unless noted otherwise.

2.1 Modeling SLSN Emission

In the early phase after a pulsar-driven supernova explosion, the broadband non-thermal emission from the emergent PWN is thermalized in the ejecta due to the high opacity of the dense ejecta, producing only quasi-thermal optical emission. Once the density, and thus the broadband opacity, decreases due to expansion of the ejecta, the non-thermal emission can escape from the ejecta without being absorbed or scattered. The escape time depends on photon energy, and can vary from months to decades. This is shown schematically in Figure 2.1. We use two different models to describe the two situations: the model for quasi-thermal optical emission (Section 2.1.1) works well in the early phases and is computationally inexpensive, but is not reliable at later times, while the model for non-thermal emission reliably and self-consistently calculates non-thermal emission for decades after the explosion, but is much more computationally expensive. The quasi-thermal model was developed in Kashiyama et al. (2016) while the non-thermal model was developed in Murase et al. (2015).

2.1.1 Modelling Quasi-Thermal Optical Emission

Spin-Down

The spin-down of the newborn pulsar is calculated from (Ostriker & Gunn 1969)

$$-\frac{dE_{\text{rot}}}{dt} = L_{\text{em}} + L_{\text{gw}}, \quad (2.1)$$

where the electromagnetic and gravitational wave luminosities are given by

$$L_{\text{em}} = \frac{\mu^2 \Omega^4}{c^3} (1 + C \sin^2 \chi_\mu) \quad \text{and} \quad (2.2)$$

$$L_{\text{gw}} = \frac{2}{5} \frac{G(\epsilon_G I)^2 \Omega_{\text{pat}}^6}{c^5} (1 + 15 \sin^2 \chi_{\epsilon_G}) \sin^2 \chi_{\epsilon_G} \quad (2.3)$$

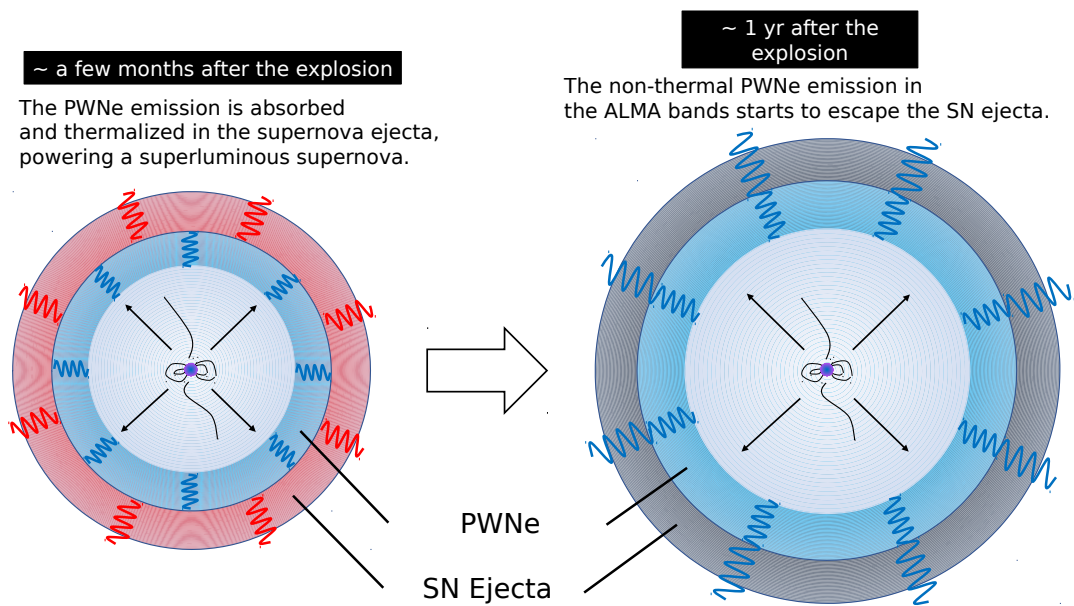


FIGURE 2.1: Schematic picture of the rapidly-rotating pulsar model for SLSNe. In a PWN, electrons and positrons from a newborn pulsar or magnetar are efficiently accelerated to very high energies. Non-thermal emission is converted into thermal radiation while the ejecta is dense enough, but at later times, the system becomes transparent to broadband non-thermal emission. The timescale for photon escape depends on photon energy - while the time for submillimetre AMLA emission to escape is ~ 1 year after the explosion, the timescale for VLA band emission to escape is ~ 10 years. The situation on the left is described by the model in Section 2.1.1 and the situation on the right is described by the model in Section 2.1.2.

respectively. $\mu = B_{\text{dip}} R^3 / 2$ is the magnetic moment, Ω is the rotational angular frequency, χ_μ is the angle between the magnetic and rotational axes, $C \sim 1$ is a pre-factor, $\epsilon_G \equiv \Delta I / I$ is the deformation rate (we assume magnetically deformed rotation (Cutler 2002; Dall’Osso et al. 2009; Stella et al. 2005)), Ω_{pat} is the pattern angular frequency, and χ_{ϵ_G} is the angle between the deformation and rotational axes (Cutler & Jones 2001). Equation 2.2 is motivated by numerical simulations (Gruzinov 2005; Spitkovsky 2006; Tchekhovskoy et al. 2013) and is a factor $3(1 + C \sin^2 \chi_\mu) / 2 \sin^2 \chi_\mu \sim 5$ larger than Equation 1.15.

We assume an isotropic magnetized wind for simplicity. This assumption, and thus this model, fails if the explosion becomes sufficiently non-spherical due to the formation of a jet. Although jet formation is still uncertain, the timescale for the prompt emission from an LGRB is around 100 – 1000 s, which corresponds to the spin-down timescale of a NS with $B_{\text{dip}} \sim 10^{15}$ G and $P \sim 1$ ms. If this timescale is comparable to the cooling or Kelvin-Helmholtz timescale ($\tau_{\text{KH}} \sim GM_{\text{NS}}^2 / L_{\text{neutrino}} R_{\text{NS}} \lesssim 100$ s) (Thompson et al. 2004) of the proto-NS, which is the diffusion timescale for neutrinos generated by the core-collapse to escape the proto-NS, then the baryons that are ablated from the proto-NS surface due to a neutrino-driven wind can be loaded into the dipolar magnetic field as it is amplified shortly after collapse. If this happens, the highly-magnetized relativistic jet could punch a hole in the progenitor star (Buciantini et al. 2007, 2008) and the GRB prompt emission can escape. Therefore, in order to avoid jet formation during pulsar spin down, we only consider spin-down timescales $\gg 100$ s and $B_{\text{dip}} < 10^{15}$ G.

We also assume magnetically deformed rotation (Cutler 2002; Dall’Osso et al. 2009; Stella et al. 2005); once inner toroidal magnetic fields are amplified and become comparable to the magnetar value, the young NS deforms and becomes oblate due to a magnetic pinch (Cutler 2002; Gualtieri et al. 2011; Kiuchi & Yoshida 2008). The deformation rate is

$$\epsilon_G = \frac{15}{4} \frac{\mathcal{E}_B}{|W|} \sim 2.5 \times 10^{-4} \left(\frac{B_t}{10^{16} \text{ G}} \right)^2, \quad (2.4)$$

where $|W| \approx M_{\text{ns}} c^2 \times 0.6\mathcal{C} / (1 - 0.5\mathcal{C}) \sim 4.4 \times 10^{53}$ erg is the gravitational binding energy of a NS with compactness parameter $\mathcal{C} = GM_{\text{ns}} / R_{\text{ns}} c^2 \sim 0.17$ (Lattimer & Prakash 2001). The deformation axis generally does not coincide with the rotation axis, which causes the NS to precess around the rotation axis (Mestel & Takhar 1972) and eventually evolve into a more prolate shape, which is a plausible configuration for the gravitational wave emission ($\chi_\mu = \chi_{\epsilon_G} = \pi/2, \Omega = \Omega_{\text{pat}}$). The gravitational wave emission only occurs when the viscous dumping timescale of the NS is shorter than the magnetic braking timescale, which can equivalently be stated as (Dall’Osso et al. 2009)

$$B_t < 2.4 \times 10^{16} \text{ G} \left(\frac{P_i}{\text{ms}} \right)^{-1} \left(\ln \left[320 \left(\frac{P_i}{\text{ms}} \right)^2 \left(\frac{B_{\text{dip}}}{10^{14} \text{ G}} \right)^{-2} + 1 \right] \right)^{1/2}. \quad (2.5)$$

Ejecta Dynamics

We assume the density structure of the supernova ejecta to be

$$\rho_{\text{ej}} \approx \frac{3 - \delta}{4\pi} \frac{M_{\text{ej}}}{R_{\text{ej}}^3} \left(\frac{R}{R_{\text{ej}}} \right)^{-\delta}, \quad (2.6)$$

with $\delta = 1$ for the index, so most of the mass is around $R \approx R_{\text{ej}}$. This index is motivated by 1D simulations by Kasen & Bildsten (2010), but more recent multi-dimensional simulations suggest that the index may be higher at later times (Suzuki & Maeda 2017). The radius of the ejecta evolves as

$$\frac{dR_{\text{ej}}}{dt} = V_{\text{ej}}. \quad (2.7)$$

Without energy ejection after the explosion, the ejecta velocity is almost constant up to the Sedov radius, but when a newborn pulsar exists, a magnetized wind accelerates the ejecta with

$$\frac{dE_{\text{K}}}{dt} = \frac{E_{\text{int}}}{t_{\text{dyn}}}, \quad (2.8)$$

where $E_{\text{K}} \approx M_{\text{ej}}V_{\text{ej}}^2/2$ is the kinetic energy of the ejecta, E_{int} is its total internal energy, and $t_{\text{dyn}} = R_{\text{ej}}/V_{\text{ej}}$ is the dynamical timescale of the ejecta. The energy injection occurs at the shock between the pulsar wind and supernova ejecta. The radius of the shocked wind region increases as

$$\frac{dR_{\text{w}}}{dt} = V_{\text{nb}} + \frac{R_{\text{w}}}{t}, \quad (2.9)$$

where V_{nb} is obtained from pressure equilibrium:

$$V_{\text{nb}} \approx \sqrt{\frac{7}{6(3-\delta)} \frac{\int L_{\text{em}} \times \min[1, \tau_{\text{T}}^{\text{nb}} V_{\text{nb}}/c] dt}{M_{\text{ej}}} \left(\frac{R_{\text{ej}}}{R_{\text{w}}}\right)^{3-\delta}}, \quad (2.10)$$

where the factor $\min[1, \tau_{\text{T}}^{\text{nb}} V_{\text{nb}}/c]$ is the fraction of spin-down luminosity deposited in the SN ejecta and $\tau_{\text{T}}^{\text{nb}} = (R_{\text{w}}/R_{\text{ej}})\tau_{\text{T}}^{\text{ej}}$, where (Equation 2.12 gives a formulation for $\tau_{\text{T}}^{\text{ej}}$). If $R_{\text{w}} \geq R_{\text{ej}}$, we set $R_{\text{w}} \approx R_{\text{ej}}$.

Electromagnetic Emission

The time dependency of E_{int} is

$$\frac{dE_{\text{int}}}{dt} = -L_{\text{sn}} - \frac{E_{\text{int}}}{t_{\text{dyn}}} + f_{\text{dep,em}}L_{\text{em}} + f_{\text{dep},^{56}\text{Ni}}L^{56}\text{Ni} + f_{\text{dep},^{56}\text{Co}}L^{56}\text{Co}. \quad (2.11)$$

The terms on the right-hand side give the energy loss via quasithermal supernova emission and adiabatic expansion and the energy injection via the pulsar wind, ^{56}Ni decay, and ^{56}Co decay respectively. L_{sn} can be given as

$$L_{\text{sn}} \approx \frac{E_{\text{int}}}{t_{\text{esc}}}, \quad (2.12)$$

where $t_{\text{esc}}^{\text{ej}}$ is the thermal photon escape time from the ejecta (also called the diffusion time t_{dif}),

$$t_{\text{esc}}^{\text{ej}} = \frac{\tau_{\text{T}}^{\text{ej}}R_{\text{ej}}}{c}, \quad (2.13)$$

where τ_T^{ej} is the optical depth of the ejecta (c/τ_T^{ej} is called the diffusion velocity), and

$$\tau_T^{\text{ej}} = \frac{(3 - \delta)\kappa M_{\text{ej}}}{4\pi R_{\text{ej}}^2}, \quad (2.14)$$

where κ is the Thompson opacity. κ generally depends on temperature, composition, and ionization state, which can all change in time, but we set it constant at $0.1 \text{ g}^{-1} \text{ cm}^2$, which is reasonable around the optical peak of SLSN; this is further justified in Chapter 3. The emission temperature can be estimated as

$$T_{\text{sn}} = \left(\frac{E_{\text{int}}}{a\mathcal{V}_{\text{ej}}} \right)^{1/4}, \quad (2.15)$$

where \mathcal{V}_{ej} is the spherical ejecta volume and a here is the radiation constant. This method of calculating the supernova emission is equivalent to the Arnett model with uniform ejecta temperature, instead of having the temperature depend on position as in the original model (Arnett 1982; Chatzopoulos et al. 2012).

There are several absorption and scattering processes which cause non-thermal photons across the entire spectrum to be thermalized or down-scattered as they propagate through the SN ejecta. The dominant type of interaction depends on the photon energy: Bethe-Heitler (BH) pair production above 10 MeV, where a gamma-ray photon interacts with a virtual photon from an electron to produce an electron-positron pair; Compton scattering for $10 \text{ keV} \lesssim h\nu \lesssim 10 \text{ MeV}$; photoelectric (bound-free) absorption for $10 \text{ eV} \lesssim h\nu \lesssim 10 \text{ keV}$; and bound-bound and free-free absorption at lower energies. We calculate the photon energy deposition fraction as

$$f_{\text{dep}} = \max[1, f_{\text{dep,sc}} + f_{\text{dep,ab}}] \quad (2.16)$$

with the contribution for scattering and absorption estimated as

$$f_{\text{dep,sc}} = 1 - (1 - K_{\text{comp}})^{\max[\tau_{\text{comp}}, \tau_{\text{comp}}^2]} \quad \text{and} \quad (2.17)$$

$$f_{\text{dep,ab}} = 1 - \exp(-\tau_{\text{BH}} - \tau_{\text{pe}}), \quad (2.18)$$

where K_{comp} is the inelasticity of Compton scattering, τ_{comp} is the optical depth, τ_{BH} is the optical depth of Bethe-Heitler pair production, and τ_{pe} is the optical depth of photoelectric absorption (Murase et al. 2015). The optical depth for photoelectric absorption is

$$\tau_{\text{pe}} = \frac{(3 - \delta)K_{\text{pe}}M_{\text{ej}}}{4\pi R_{\text{ej}}^2}, \quad (2.19)$$

where

$$K_{\text{pe}} = 5\zeta \left(\frac{E_\gamma}{10 \text{ keV}} \right)^{-3} \text{ g}^{-1} \text{ cm}^2 \quad (2.20)$$

is the opacity for oxygen dominated ejecta. $0 \leq \zeta \leq 1$ is a time-dependent scaling factor that can be determined from the effective ionization fraction; it increases as the ejecta becomes less ionized since there are more bound electrons to absorb the photons. This value is still very uncertain, and to solve for it would require full radiation hydrodynamics simulations which account for ionization in the ejecta. Since these simulations are difficult and have not yet been done in the case of pulsar-driven supernovae, we set ζ to the midpoint 0.5 for simplicity. It is worth noting that the

fraction of energy in the soft x-ray bands is always subdominant, and the SN light curve is not sensitive to photoelectric absorption until $\gtrsim 100$ days after the explosion.

At the interface between the magnetized wind and ejecta, highly relativistic electrons are injected and further accelerated by the shock or magnetic turbulence; these electrons then rapidly cool via sychrotron emission and inverse Compton scattering. These scattered photons have high enough energies to produce a positron/electron pair by two photon annihilation, which can lead to an electromagnetic cascade. This effect can be calculated by assuming an electron injection spectrum of (Murase et al. 2015)

$$E_e \frac{d\dot{e}_{E_e}^{\text{inj}}}{d\gamma_e} \propto \begin{cases} (\gamma_e/\gamma_b)^{-q_1} & (\gamma_e < \gamma_{e,b}), \\ (\gamma_e/\gamma_b)^{-q_2} & (\gamma_b < \gamma_e < \gamma_M), \end{cases} \quad (2.21)$$

where $q_1 = 1-1.5$, $q_2 = 2.5-3$, and $\gamma_b \sim 10^{4.5-6}$; these are motivated by observations of young PWNe (Tanaka & Takahara 2010). By equating the acceleration timescale $t_{\text{acc}} = \eta\gamma_e m_e c / eB$, where $\eta \geq 1$ is a pre-factor accounting for acceleration efficiency, and the sychrotron cooling timescale $t_{\text{syn}} = 3m_e c / 4\sigma_T U_B \gamma_e$, where U_B is the magnetic energy density calculated in Equation 2.26, the maximum electron energy can be estimated as $\gamma_M \approx (6\pi e / \eta\sigma_T B)^{1/2}$. The electron/positron pair multiplicity μ_{\pm} and break Lorentz factor γ_b can be related using

$$\mu_{\pm} \sim 10^9 \epsilon_e \gamma_{b,5}^{-1} \left(\frac{\gamma_b}{100} \right)^{q_1-1} \left[\frac{(2-q_1)(q_2-2)}{(q_1-1)(q_2-q_1)} \right] B_{\text{dip},14} P_{-2.5}^{-2}, \quad (2.22)$$

where ϵ_e is fraction of energy that goes into particles.

The total energy deposition factor of the magnetized wind is

$$f_{\text{dep,em}} = \frac{\int f_{\text{dep}}(E_\gamma) E_\gamma \frac{dN_\gamma}{dE_\gamma} dE_\gamma}{\int E_\gamma \frac{dN_\gamma}{dE_\gamma} dE_\gamma} \quad (2.23)$$

where $f_{\text{dep}}(E_\gamma)$ is the energy deposition fraction for photons of energy E_γ , and dN_γ/dE_γ is the wind nebula spectrum due to the injected electrons in Equation 2.21, which can also be approximated as a broken power law (Murase et al. 2015)

$$E_\gamma \frac{dN_\gamma}{dE_\gamma} = \frac{\epsilon_e L_{\text{em}}}{\mathcal{R}_b E_{\text{syn}}^b} \begin{cases} (E_\gamma/E_{\text{syn}}^b)^{-q_1/2} & (E_\gamma < E_{\text{syn}}^b), \\ (E_\gamma/E_{\text{syn}}^b)^{-1} & (E_{\text{syn}}^b < E_\gamma < \epsilon_{\gamma,\text{max}}) \end{cases} \quad (2.24)$$

with $\mathcal{R}_b \sim 2/(2-q_1) + \ln(\epsilon_{\gamma,\text{max}}/E_\gamma/E_{\text{syn}}^b)$, $\epsilon_e = 1 - \epsilon_B \approx 1$, and the break photon energy

$$E_{\text{syn}}^b = \frac{3}{2} \hbar \gamma_b^2 \frac{eB}{m_e c} \quad (2.25)$$

We take the magnetic field energy density in the early PWN to be

$$U_B = \epsilon_B \frac{3 \int L_{\text{em}} dt}{4\pi R_w^3}, \quad (2.26)$$

where the fraction of energy that enters the magnetic field $\epsilon_B = 10^{-3} - 10^{-2}$ (e.g., Atoyan & Aharonian 1996; de Jager et al. 1996; Kennel & Coroniti 1984; Tanaka & Takahara 2010). The field B is estimated to be

$$B = 36 \text{ G } P_{i,-2.5}^{-1} \epsilon_{B,-2}^{1/2} \left(\frac{V_{\text{ej}}}{5000 \text{ km s}^{-1}} \right)^{-3/2} t_7^{-3/2} \left[1 - (1 + t/t_{\text{SD}})^{-1} \right]^{1/2}, \quad (2.27)$$

the t_{SD} is the characteristic spin-down time of the pulsar (Equation 1.21).

The luminosity of ^{56}Ni decay is calculated as

$$L_{56\text{Ni}} = M_{56\text{Ni}} \epsilon_{56\text{Ni}} \exp\left(-\frac{t}{t_{56\text{Ni}}}\right), \quad (2.28)$$

$$L_{56\text{Co}} = M_{56\text{Ni}} (\epsilon_{56\text{Co}} - \epsilon_{56\text{Ni}}) \exp\left(-\frac{t}{t_{56\text{Co}}}\right), \quad (2.29)$$

where $M_{56\text{Ni}}$ is the ^{56}Ni mass, $\epsilon_{56\text{Ni}} = 3.9 \times 10^{10} \text{ erg s}^{-1} \text{ g}^{-1}$, $\epsilon_{56\text{Co}} = 6.8 \times 10^9 \text{ erg s}^{-1} \text{ g}^{-1}$, $t_{56\text{Ni}} = 8.8 \text{ days}$, and $t_{56\text{Co}} = 111.3 \text{ days}$. We estimate the deposition fraction from gamma rays consistently with the wind dissipation,

$$f_{\text{dep}, 56\text{Ni}(\text{Co})} = \frac{\sum_i f_{\text{dep}}(\epsilon_{56\text{Ni}(\text{Co}), i}) \mathcal{P}_{56\text{Ni}(\text{Co}), i} \epsilon_{56\text{Ni}(\text{Co}), i}}{\sum_i \mathcal{P}_{56\text{Ni}(\text{Co}), i} \epsilon_{56\text{Ni}(\text{Co}), i}} \quad (2.30)$$

where $\epsilon_{56\text{Ni}(\text{Co}), i}$ $\mathcal{P}_{56\text{Ni}(\text{Co}), i}$ are the mean decay energy and decay probability. We consider the 6 ^{56}Ni channels and 11 ^{56}Co from (Nadyozhin 1994) and assume all energy from positron emission goes into the thermal bath.

Peak Time and Luminosity

The peak of the SLSN will occur around when the velocity of photon diffusion through the ejecta becomes equal to the ejecta velocity, and it follows that the peak time equivalent to both the diffusion time and dynamical time under this condition. Using Equation 2.13 here gives

$$t_{\text{dif}} = \frac{\tau_{\Gamma}^{\text{ej}} R_{\text{ej}}}{c} = \frac{R_{\text{ej}}}{V_{\text{ej}}}, \quad (2.31)$$

where using Equation 2.14 gives the ejecta velocity

$$V_{\text{ej}} = \frac{4\pi c R_{\text{ej}}^2}{(3 - \delta)\kappa M_{\text{ej}}}, \quad (2.32)$$

Solving for R_{ej} here gives

$$R_{\text{ej}} = \sqrt{\frac{(3 - \delta)\kappa M_{\text{ej}}}{4\pi c V_{\text{ej}}}}. \quad (2.33)$$

However, since the kinetic energy of the ejecta comes almost entirely from the spin-down of the central pulsar, then the velocity can also be written

$$V_{\text{ej}} \approx \sqrt{\frac{2E_{\text{rot}}}{M_{\text{ej}}}} = \sqrt{\frac{I}{M_{\text{ej}}}} \frac{2\pi}{P}. \quad (2.34)$$

using Equation 1.14. Using Equations 2.31, 2.33, and 2.34, we can calculate the peak time

$$t_{\text{peak}} \approx \frac{P^{1/2} M_{\text{ej}}^{3/4} \kappa^{1/2}}{\pi I^{1/4} c^{1/2}} \sqrt{\frac{3-\delta}{8}}. \quad (2.35)$$

$$\approx 25 \text{ days} \left(\frac{P}{1 \text{ ms}} \right)^{1/2} \left(\frac{M_{\text{ej}}}{5 M_{\odot}} \right)^{3/4}. \quad (2.36)$$

It is worth noting that the width of the peak is also roughly comparable to the peak time.

The luminosity at the peak time is around

$$L_{\text{peak}} \approx \frac{E_{\text{int}}}{t_{\text{dif}}}, \quad (2.37)$$

where E_{int} can be approximated as

$$E_{\text{int}} \approx E_{\text{rot}} \left(\frac{t_{\text{dif}}}{t_{\text{SD}}} \right)^{\pm 1}, \quad (2.38)$$

where the index is positive if $t_{\text{dif}} \leq t_{\text{SD}}$ and negative if $t_{\text{dif}} \geq t_{\text{SD}}$.

If $t_{\text{dif}} \leq t_{\text{SD}}$, then the peak luminosity is just the spin-down power of the pulsar from Equation 1.15 (Equation 2.2 in our model). Equation 1.15 can also be written to depend on P and B_{char}

$$L_{\text{peak}} \approx 2.9 \times 10^{45} \text{ erg s}^{-1} \left(\frac{P}{1 \text{ ms}} \right)^{-4} \left(\frac{B_{\text{char}}}{10^{13} \text{ G}} \right)^2. \quad (2.39)$$

If $t_{\text{dif}} \geq t_{\text{SD}}$, then L_{peak} becomes

$$L_{\text{peak}} \approx \frac{12\pi^2 I^{5/2} c^4}{R_{\text{NS}} \kappa (3-\delta)} B_{\text{char}}^{-2} P^{-1} M_{\text{ej}}^{-3/2}, \quad (2.40)$$

$$\approx 5.6 \times 10^{46} \text{ erg s}^{-1} \left(\frac{P}{1 \text{ ms}} \right)^{-1} \left(\frac{B_{\text{char}}}{10^{13} \text{ G}} \right)^{-2} \left(\frac{M_{\text{ej}}}{5 M_{\odot}} \right)^{-3/2}. \quad (2.41)$$

Summary

This has six input parameters overall: the initial spin period P , the initial toroidal and poloidal magnetic field B , the ejecta mass M_{ej} , the ejected nickel mass M_{Ni} , the explosion energy from the neutrino mechanism E_{SN} , and the Thompson opacity κ . The model outputs optical light curves in bands that can be modified by the user, allowing us to produce model curves in UBV_R and ugriz filters, as well as any custom filters.

The main assumption that is unreliable at later times is the assumption of the photon spectrum in the wind nebula, Equation 2.24. To solve this self-consistently, should be calculated from the electron injection spectrum and using a more complicated energy transport model within the PWN, which includes a more complicated treatment of pair cascades. The early quasi-thermal emission is not very sensitive to the exact shape of the spectrum, since all the photons are absorbed and re-emitted, so this treatment is justified for modelling that emission, but not for non-thermal emission once it escapes the ejecta.

2.1.2 Modelling Non-Thermal Emission

This model gives a full treatment of electron and photon energy transport, and will thus produce reliable results for later non-thermal emission. The neutron star spin-down and ejecta dynamics are treated in the same way, so Equations 2.1-2.10 and Equation 2.26 are still valid in this model.

Leptonic Emission from Embryonic PWNe - Analytical Model

The electron injection spectrum from Equation 2.21 is also assumed in this model, with the same parameters q_1 , q_2 , and γ_b and with most of the energy $\epsilon_e \sim 1$ being carried by leptons (Tanaka & Takahara 2010, 2013).

The radiative cooling timescale is given by $t_{\text{rad}}^{-1} = t_{\text{syn}}^{-1} + t_{\text{IC}}^{-1} = t_{\text{syn}}^{-1}(1 + Y)$, where $t_{\text{syn}} = 3m_e c / 4\sigma_T U_B \gamma_e$ and $Y = t_{\text{syn}} / t_{\text{IC}}$ is the Compton Y parameter. When $t \gg t_{\text{SD}}$, the cooling Lorentz factor of the electrons is estimated as

$$\gamma_e = 1.9 \times 10^{-2} P_{i,-2.5}^2 \epsilon_{B,-2}^{-1} \left(\frac{V_{\text{ej}}}{5000 \text{ km s}^{-1}} \right)^3 t_7^2 (1 + Y)^{-1}, \quad (2.42)$$

where $t_{\text{rad}} = t_{\text{dyn}} = R_{\text{ej}} / V_{\text{ej}}$. Since γ_e can not physically be less than unity, a γ_e value less than unity implies that relativistic electrons will radiate almost all of their energy within t_{dyn} . In the Thompson limit, Y is roughly

$$Y \approx \frac{-1 + \frac{L_{\text{SN}} t V_{\text{ej}}}{\epsilon_B \mathcal{E}_{\text{em}} c} + \sqrt{\left(1 + \frac{L_{\text{SN}} t V_{\text{ej}}}{\epsilon_B \mathcal{E}_{\text{em}} c}\right)^2 + \frac{4\epsilon_e L_{\text{SN}} t V_{\text{ej}}}{\epsilon_B \mathcal{E}_{\text{em}} c}}}{2}. \quad (2.43)$$

The distribution of pairs is mostly in the fast cooling regime. In this case, with constant Y , the steady-state electron distribution $dN_e/d\gamma_e$ is $\propto \gamma_e^{-2}$ for $1 \lesssim \gamma_e \lesssim \gamma_c$, $\gamma_e^{-q_1-1}$ for $\gamma_c \lesssim \gamma_e \leq \gamma_b$, and $\gamma_e^{-q_2-1}$ for $\gamma_b \leq \gamma_e \leq \gamma_M$, with the decrease in power-law index resulting from higher energy electrons radiating their energy away faster. γ_M is calculated by equating the acceleration timescale $t_{\text{acc}} = \eta \gamma_e m_e c / eB$ and the total radiative timescale t_{rad} , which gives

$$\gamma_M \approx \sqrt{\frac{6\pi e}{\eta \sigma_T B (1 + Y_M)}} \simeq 1.9 \times 10^7 P_{i,-2.5}^{1/2} \eta^{-1/2} \epsilon_{B,-2}^{-1/4} \left(\frac{V_{\text{ej}}}{5000 \text{ km s}^{-1}} \right)^{3/4} t_7^{3/4} (1 + Y_M)^{-1/2}, \quad (2.44)$$

where $Y_M \equiv Y(\gamma_M)$. This means that gamma-ray energies should be less than

$$E_\gamma^M \approx \gamma_M m_e c^2 \simeq 9.9 \text{ TeV } P_{i,-2.5}^{1/2} \eta^{-1/2} \epsilon_{B,-2}^{-1/4} \left(\frac{V_{\text{ej}}}{5000 \text{ km s}^{-1}} \right)^{3/4} t_7^{3/4} (1 + Y_M)^{-1/2}, \quad (2.45)$$

which implies that $\gtrsim 10$ -100 TeV gamma rays are not expected at early stages of the PWN.

In the fast cooling regime, the synchrotron photon spectrum is

$$E_\gamma L_{E_\gamma}^{\text{syn}} \sim \frac{\epsilon_e L_{\text{em}}}{2(1 + Y) \mathcal{R}_b} \begin{cases} (E_\gamma / E_{\text{syn}}^b)^{(2-q_1)/2} & (E_\gamma \leq E_{\text{syn}}^b), \\ (E_\gamma / E_{\text{syn}}^b)^{(2-q_2)/2} & (E_{\text{syn}}^b \leq E_\gamma) \end{cases}, \quad (2.46)$$

with $\mathcal{R}_b \sim (2 - q_1)^{-1} + (q_2 - 2)^{-1}$, and the characteristic synchrotron energy given in Equation 2.25. The spectra is expected to peak in the x-ray range. Note that the synchrotron maximum energy

$$E_{\text{syn}}^M \equiv E_{\text{syn}}^b(\gamma_b = \gamma_M) = 240 \text{ MeV } \eta^{-1}(1 + Y_M)^{-1} \quad (2.47)$$

hardly depends on various parameters.

The expected IC luminosity in the fast cooling regime is very roughly $L_{\text{IC}} \sim Y(1 + Y)^{-1}L_{\text{em}}$. We first assume a seed photon spectrum with $E_\gamma L_{E_\gamma} \propto E_\gamma^{2-\beta}$, where $\beta \leq 1 + q_1/2$. Note that synchrotron self-Compton (SSC) corresponds to $\beta = 1 + q_1/2$ in the fast cooling regime. Thus, in the Thomson limit, the IC photon spectrum is

$$E_\gamma L_{E_\gamma}^{\text{IC}} \propto \begin{cases} E_\gamma^{(2-q_1)/2} & (E_\gamma \leq E_{\text{IC}}^b), \\ E_\gamma^{(2-q_2)/2} & (E_{\text{IC}}^b < E_\gamma) \end{cases} \quad (2.48)$$

This can be obtained by noting that $L_{E_\gamma}^{\text{IC}} \sim \int d\gamma_e (d\tau_{\text{IC}}/d\gamma_e) L_E^{\text{seed}}(\gamma_e, E)$, where τ_{IC} is the IC optical depth. A similar spectrum is expected when the seed spectrum is thermal. In the SSC case, the typical IC energy is

$$E_{\text{SSC}}^b \approx 2\gamma_b^2 E_{\text{syn}}^b \simeq 130 \text{ TeV } \gamma_{b,5}^4 P_{i,-2.5}^{-1} \epsilon_{B,-2}^{1/2} \left(\frac{V_{\text{ej}}}{5000 \text{ km s}^{-1}} \right)^{-3/2} t_7^{-3/2}, \quad (2.49)$$

although such energies are difficult to achieve at early times due to the implications of Equation 2.45. In timescales of days to months, when SN emission is prominent, thermal photons are upscattered by relativistic pairs via the external IC (EIC) process. The energy flux of seed photons has a peak at $E_{\text{SN}} \approx 3.92kT_{\text{SN}}$, and the typical IC energy is

$$E_{\text{EIC}}^b \approx 2\gamma_b^2 E_{\text{SN}} \simeq 78 \text{ GeV } \gamma_{b,5}^2 \left(\frac{k_B T_{\text{SN}}}{1 \text{ eV}} \right). \quad (2.50)$$

In fact, the Klein-Nishina (KN) effect (Klein & Nishina 1929) becomes increasingly important at higher energies. We introduce two energy scales (Murase et al. 2011),

$$E_{\text{KN}}^{\text{typ}} \approx m_e^2 c^4 / (2E_{\text{typ}}), \quad (2.51)$$

$$E_{\text{KN}}^b \approx \gamma_b m_e c^2, \quad (2.52)$$

where E_{typ} is the typical energy for target photons. $E_{\text{KN}}^{\text{typ}}$ is the typical energy of an electron affected by the KN effect while E_{KN}^b corresponds to when the effect becomes more pronounced; these energies also correspond to breaks in the IC spectrum when the Klein-Nishina effect is relevant, as we shall show shortly. The KN cross-section is

$$\sigma_{\text{KN}} = \frac{3}{4} \left[\frac{1+x}{x^3} \left(\frac{2x(1+x)}{1+2x} - \ln(1+2x) \right) \right] + \frac{1}{2x} \ln(1+2x) - \frac{1+3x}{(1+2x)}, \quad (2.53)$$

where $x \equiv \frac{E_\gamma}{m_e c^2}$. We expect $E_{\text{typ}} \approx E_{\text{syn}}^b$ for the SSC case and $E_{\text{typ}} \approx E_{\text{SN}}$ for the EIC case. At these energies the KN effect make the IC spectra complicated, so we end up solving these equations numerically. However, it is useful to see some analytical expressions.

First, we consider a seed photon spectrum of $E_\gamma L_{E_\gamma} \propto E_\gamma^{2-\beta}$ and introduce $E_{\text{KN},1}$ as the first break energy due to the KN effect. For $E_{\text{KN},1} > E_{\text{IC}}^b$, we get (e.g., Murase et al. 2011, 2010)

$$E_\gamma L_{E_\gamma}^{\text{IC}} \propto \begin{cases} E_\gamma^{(2-q_1)/2} & (E_\gamma \leq E_{\text{IC}}^b) \\ E_\gamma^{(2-q_2)/2} & (E_{\text{IC}}^b < E_\gamma \leq E_{\text{KN},1}) \\ E_\gamma^{\beta-q_2} & (E_{\text{KN},1} \leq E_\gamma), \end{cases} \quad (2.54)$$

where

$$E_{\text{KN},1} = E_{\text{KN}}^{\text{typ}} \simeq 33 \text{ GeV} \left(\frac{E_{\text{typ}}}{4 \text{ eV}} \right)^{-1}. \quad (2.55)$$

The IC emission at $E_\gamma > E_{\text{KN},1}$ is dominated by Thomson scattering between pairs with $\gamma_e \sim E_\gamma / (m_e c^2)$ and seed photons with $E \sim m_e^2 c^4 / (2E_\gamma)$. If $E_{\text{KN},1} < E_{\text{IC}}^b$, then

$$E_\gamma L_{E_\gamma}^{\text{IC}} \propto \begin{cases} E_\gamma^{(2-q_1)/2} & (E_\gamma \leq E_{\text{KN},1}) \\ E_\gamma^{\beta-q_1} & (E_{\text{KN},1} < E_\gamma \leq E_{\text{KN},2}) \\ E_\gamma^{\beta-q_2} & (E_{\text{KN},2} \leq E_\gamma), \end{cases} \quad (2.56)$$

where Equation 2.55 still holds for the first KN break and

$$E_{\text{KN},2} = E_{\text{KN}}^b \simeq 51 \text{ GeV } \gamma_{b,5} \quad (2.57)$$

is the second KN break. If $\beta = 1 + q_1/2$, as expected in the SSC case, then

$$E_\gamma L_{E_\gamma}^{\text{IC}} \propto \begin{cases} E_\gamma^{(2-q_1)/2} & (E_\gamma \leq E_{\text{KN},2}) \\ E_\gamma^{\beta-q_2} & (E_{\text{KN},2} \leq E_\gamma). \end{cases} \quad (2.58)$$

This spectrum can be realized in the PWN SSC emission, but the break is smeared out due to leptons upscattering photons with E_{typ} not contributing above $E_{\text{KN}}^{\text{typ}}$.

Because the Rayleigh-Jeans spectrum is quite hard to the synchrotron spectrum, the KN cross section becomes important when the seed photon spectrum is thermal. For $E_{\text{KN},1} > E_{\text{IC}}^b$, we expect

$$E_\gamma L_{E_\gamma}^{\text{IC}} \propto \begin{cases} E_\gamma^{(2-q_1)/2} & (E_\gamma \leq E_{\text{IC}}^b) \\ E_\gamma^{(2-q_2)/2} & (E_{\text{IC}}^b < E_\gamma \leq E_{\text{KN},1}) \\ E_\gamma^{\beta_{\text{KN}}-q_2} & (E_{\text{KN},1} \leq E_\gamma), \end{cases} \quad (2.59)$$

where β_{KN} reflects the logarithmic energy dependence in the KN cross section. For example, in the EIC case, one roughly expects $E_\gamma^{\beta_{\text{KN}}} \propto \ln[2E_\gamma E_{\text{SN}} / (m_e^2 c^4)]$. If $E_{\text{KN},1} \leq E_{\text{IC}}^b$, then

$$E_\gamma L_{E_\gamma}^{\text{IC}} \propto \begin{cases} E_\gamma^{(2-q_1)/2} & (E_\gamma \leq E_{\text{KN},1}) \\ E_\gamma^{\beta_{\text{KN}}-q_1} & (E_{\text{KN},1} < E_\gamma \leq E_{\text{KN},2}) \\ E_\gamma^{\beta_{\text{KN}}-q_2} & (E_{\text{KN},2} \leq E_\gamma). \end{cases} \quad (2.60)$$

These spectra are typically anticipated for EIC emission from the PWN in the early phase.

Leptonic Emission from Embryonic PWNe - Numerical Model

While we have given some analytical estimates, we solve the necessary equations numerically due to not only the KN effect, but also high-energy gamma rays may not escape from the PWN due to the $\gamma\gamma \rightarrow e^+e^-$ process. As a result, detailed numerical spectra may deviate from the above analytical estimates. For the intrinsic PWN emission, we solve the following kinetic equations:

$$\frac{\partial n_{E_e}^e}{\partial t} = \frac{\partial n_{E_e}^{(\gamma\gamma)}}{\partial t} - \frac{\partial}{\partial E} \left[\left(\frac{E_e}{t_{\text{IC}}} + \frac{E_e}{t_{\text{syn}}} + \frac{E_e}{t_{\text{dyn}}} \right) n_{E_e}^e \right] + \dot{n}_{E_e}^{\text{inj}}, \quad (2.61)$$

$$\frac{\partial n_{E_\gamma}^\gamma}{\partial t} = -\frac{n_{E_\gamma}^\gamma}{t_{\gamma\gamma}} - \frac{n_{E_\gamma}^\gamma}{t_{\text{esc}}^{\text{nb}}} + \frac{\partial n_{E_\gamma}^{(\text{IC})}}{\partial t} + \frac{\partial n_{E_\gamma}^{(\text{syn})}}{\partial t}, \quad (2.62)$$

where

$$\begin{aligned} t_{\gamma\gamma}^{-1} &= \int dE_\gamma n_{E_\gamma}^\gamma \int \frac{d \cos \theta}{2} \tilde{c} \sigma_{\gamma\gamma}, \\ \frac{\partial n_{E_\gamma}^{(\text{IC})}}{\partial t} &= \int dE_e n_{E_e}^e \int dE_\gamma n_{E_\gamma}^\gamma \int \frac{d \cos \theta}{2} \tilde{c} \frac{d\sigma_{\text{KN}}}{dE_\gamma}, \\ \frac{\partial n_{E_e}^{(\gamma\gamma)}}{\partial t} &= \frac{1}{2} \int dE_\gamma n_{E_\gamma}^\gamma \int dE_\gamma' n_{E_\gamma'}^\gamma \int \frac{d \cos \theta}{2} \tilde{c} \frac{d\sigma_{\gamma\gamma}}{dE_e}, \\ \sigma_{\gamma\gamma} &= \frac{3}{16} \sigma_T (1 - \beta_{\text{cm}}^2) \left(2\beta_{\text{cm}} (\beta_{\text{cm}}^2 - 2) + (3 - \beta_{\text{cm}}^4) \ln [(1 + \beta_{\text{cm}})/(1 - \beta_{\text{cm}})] \right) \end{aligned}$$

$\tilde{c} = (1 - \cos \theta)c$ (where θ is the angle between two particles), $t_{\gamma\gamma}$ is the two-photon annihilation time, $\sigma_{\gamma\gamma}$ is the two-photon annihilation cross section, $t_{\text{esc}}^{\text{nb}} = R_w/c$ is the photon escape time from the PWN, $\beta_{\text{cm}} = \sqrt{1 - 4m_e^2 c^4/S_m}$, and S_m is the Mandelstam variable (Mandelstam 1958). We use the continuous energy-loss approximation for the IC process to save time, and assume $E_e = (E_\gamma + E_\gamma')/2$ for pairs produced by photon annihilation. We solve the above equations using the constant electron injection with $\dot{n}_{E_e}^{\text{inj}}$ determined from Equation 2.21. We also consistently calculate the energy spectrum and emission from previously injected "relic" electrons. To simplify our calculations, we use a one-zone model.

For initial conditions, we set $n_{E_e}^e = 0$ and $n_{E_\gamma}^\gamma$ to a blackbody spectrum with T_{SN} . High-energy photons are produced from these injected non-thermal electrons. The calculation is performed during the dynamical time t_{dyn} , and we obtain quasi-steady-state spectra. The differential luminosity before attenuation, which is related to $n_{E_\gamma}^\gamma$, is

$$E_\gamma L_{E_\gamma} = \frac{(E_\gamma^2 n_{E_\gamma}^\gamma) \mathcal{V}_w}{t_{\text{esc}}^{\text{nb}}} \quad (2.63)$$

which gives observed x-ray and gamma-ray fluxes. $\mathcal{V}_w = (4/3)\pi R_w^3$ here is the volume of the PWN.

Two-photon Annihilation in Embryonic PWNe

The quasi-thermal and synchrotron emission can prevent gamma rays from leaving the PWN via annihilation, so we must take gamma-ray attenuation (and subsequent

regeneration via pair creation) into account. For a thermal photon spectrum, using the SN photon density $n_\gamma^{\text{SN}} = 2\zeta(3)(k_B T_{\text{SN}})^3 / (\pi^2 \hbar^3 c^3)$, the pair-production optical depth is

$$\tau_{\gamma\gamma_{\text{SN}}}^{\text{ej}} \approx \frac{3}{16} \sigma_T n_\gamma^{\text{SN}} R_{\text{ej}} \mathcal{G} \left(x = \frac{m_e^2 c^4}{E_\gamma k_B T_{\text{SN}}} \right) \simeq 2.0 \times 10^4 \left(\frac{k_B T_{\text{SN}}}{1 \text{ eV}} \right)^3 \left(\frac{V_{\text{ej}}}{5000 \text{ km s}^{-1}} \right) t_7, \quad (2.64)$$

where $\mathcal{G}(x) \equiv \mathcal{F}(x)/\zeta(3)$ and $\mathcal{F}(x)$ is defined in Dermer et al. (2012). In this expression, $\mathcal{G}(x)$ peaks at around at

$$E_{\gamma\gamma}^{\text{typ}} \approx \frac{m_e^2 c^4}{2k_B T_{\text{SN}}} \simeq 130 \text{ GeV} \left(\frac{k_B T_{\text{SN}}}{1 \text{ eV}} \right)^{-1}. \quad (2.65)$$

When the target photons are from synchrotron emission with a power-law spectrum with $n_E^{\text{syn}} \propto E^{-\beta}$, the pair production optical depth in the PWN is estimated to be

$$\begin{aligned} \tau_{\gamma\gamma_{\text{syn}}}^{\text{nb}} &\approx 0.2 \sigma_T (E_\gamma n_E^{\text{syn}}) R_w, & (2.66) \\ &\simeq 3.1 \times 10^{-3} \gamma_{b,5}^{-2} P_{i,-2.5} B_{\text{dip},14}^{-2} \epsilon_{B,-2}^{-1/2} \epsilon_e \left(\frac{V_{\text{ej}}}{5000 \text{ km s}^{-1}} \right)^{1/2} \frac{t_7^{-3/2}}{(1+Y)} \left(\frac{E_\gamma}{E_{\gamma\gamma}^{\text{typ}}} \right)^{\beta-1}, & (2.67) \end{aligned}$$

where $R_w \approx R_{\text{ej}} = V_{\text{ej}} t$ is used for analytical estimates. The typical energy $E_{\gamma\gamma}^{\text{typ}}$ is

$$E_{\gamma\gamma}^{\text{typ}} \approx \frac{m_e^2 c^4}{E_{\text{syn}}^b} \simeq 4.1 \times 10^{-2} \text{ GeV} \gamma_{b,5}^{-2} P_{i,-2.5} \epsilon_{B,-2}^{-1/2} \left(\frac{V_{\text{ej}}}{5000 \text{ km s}^{-1}} \right)^{3/2} t_7^{3/2}. \quad (2.68)$$

We calculate electromagnetic cascades for emission generated in the PWN, and we take into account further attenuation by SN photon fields by multiplying by $e^{-(\tau_{\gamma\gamma}^{\text{ej}} + \tau_{\gamma\gamma}^{\text{nb}})}$.

TeV gamma rays are prevented from leaving the PWN in the early phase due to SN photons in the optical or infrared bands, but are expected to escape in a few years. GeV photons can escape much earlier but are still strongly attenuated for around the first 30 days.

Matter Attenuation in the Stellar Material

Photons which escape from the PWN can be significantly attenuated in the ejecta, which is accounted for as a post-process. At energies below ~ 10 keV, photoelectric absorption dominates; in the soft x-ray band, ionization breakout emission can provide an interesting signal (Metzger et al. 2014); and at high energies, Compton scattering and Bethe-Heitler (BH) pair production dominate. The optical depth is $\tau = \tau_{\text{pe}} + \tau_{\text{comp}} + \tau_{\text{BH}}$, where the three optical depths are for photoelectric absorption, Compton scattering, and BH pair production. With a mass attenuation coefficient κ , τ is generally expressed as $\kappa \rho R$, where ρ is the density and R is the path length. The bound-free opacity $\kappa_{\text{bf}} \simeq 2.37 \text{ cm}^2 \text{ g}^{-1} (Z/6)^3 (E_\gamma/10 \text{ keV})^{-3}$ gives conservative estimates of x-ray emission.

The Compton optical depth in the ejecta is

$$\tau_{\text{comp}}^{\text{ej}} \approx \kappa_{\text{comp}} \rho_{\text{ej}} R_{\text{ej}} = \frac{(3 - \delta) M_{\text{ej}} \sigma_{\text{comp}}}{4\pi \mu_e m_u R_{\text{ej}}^2}, \quad (2.69)$$

where $\kappa_{\text{comp}} = \sigma_{\text{comp}} / (\mu_e m_u)$. The mass-energy transfer coefficient is

$$K_{\text{comp}} \sigma_{\text{comp}} = \frac{3}{4} \sigma_T \left[\frac{2(1+x)^2}{x^2(1+2x)} - \frac{1+3x}{(1+2x)^2} - \frac{(1+x)(2x^2-2x-1)}{x^2(1+2x)^2} - \frac{4x^2}{3(1+2x)^3} - \left(\frac{1+x}{x^3} - \frac{1}{2x} + \frac{1}{2x^3} \right) \ln(1+2x) \right], \quad (2.70)$$

where $x \equiv E_\gamma / (m_e c^2)$ and K_{comp} is the gamma-ray inelasticity. This formula is obtained from the known KN cross section and kinematics.

For a nucleus with mass number A and atomic number Z , the BH process on a nuclear scale is $\sigma_{\text{BH}} = Z^2 \sigma_{\text{BH}}^{(p)}$. Taking contributions from both nuclei and electrons into account, with $\mu_e \approx 2$,

$$\tau_{\text{BH}}^{\text{ej}} \approx \frac{(3 - \delta) M_{\text{ej}} (Z_{\text{eff}} + 1) \sigma_{\text{BH}}^{(p)}}{8\pi m_u R_{\text{ej}}^2}, \quad (2.71)$$

where Z_{eff} is the effective atomic number, which depends on the chemical composition of the ejecta. For $X_{\text{H}} = 0.6$, $X_{\text{He}} = 0.3$, $X_{\text{C}} = 0.1$, $Z_{\text{eff}} \approx 2.5$, while $Z_{\text{eff}} \approx 7$ for $X_{\text{CO}} = 1$. The mass energy-transfer coefficient at high energies is approximately

$$K_{\text{BH}} \sigma_{\text{BH}} = \frac{x-2}{x} \sigma_{\text{BH}}, \quad (2.72)$$

although this neglects contributions from electron-positron annihilation. This model uses a cross section derived from the Born approximation (Chodorowski et al. 1992), but a simpler formula, useful for analytical estimates, is

$$\sigma_{\text{BH}}^{(p)} \approx \frac{3\alpha_{\text{em}} \sigma_T}{8\pi} \left(\frac{28}{9} \ln(2x) - \frac{218}{27} \right), \quad (2.73)$$

which gives $\sigma_{\text{BH}} \sim Z^2 10^{-26} \text{ cm}^2$ at GeV energies. Note that $\sigma_{\text{BH}}^{(p)} \sim \alpha_{\text{em}} \sigma_T$, where $\alpha_{\text{em}} \simeq 1/137$ is the fine-structure constant. At GeV energies, $\tau_{\text{BH}}^{\text{ej}}$ is estimated as

$$\tau_{\text{BH}}^{\text{ej}} \simeq 0.57 \left(\frac{Z_{\text{eff}} + 1}{3} \right) \left(\frac{M_{\text{ej}}}{5M_\odot} \right) \left(\frac{V_{\text{ej}}}{5000 \text{ km s}^{-1}} \right)^{-2} t_7^{-2} \quad (2.74)$$

which implies significant BH attenuation at early times.

In the small inelasticity limit, a particle loses K_γ per interaction, so the survival fraction is $(1 - K_\gamma)^{\max[\tau, \tau^2]}$, where $\max[\tau, \tau^2]$ is the number of scatterings. In the large inelasticity limit, as in the attenuation case, the survival fraction is given by $e^{-\tau}$. Combining the two limits gives a hard x-ray/gamma ray escape fraction of

$$f_{\text{esc}} = e^{-\tau} + (1 - e^{-\tau})(1 - K_\gamma)^{\max[\tau, \tau^2]} \quad (2.75)$$

GeV-TeV gamma rays cannot leave the ejecta until a few months after the explosion. GeV gamma ray escape is allowed at

$$t_{\gamma\text{-bo}} \simeq 88 \text{ days} \left(\frac{Z_{\text{eff}} + 1}{3} \right)^{1/2} \left(\frac{M_{\text{ej}}}{5M_\odot} \right)^{1/2} \left(\frac{V_{\text{ej}}}{5000 \text{ km s}^{-1}} \right)^{-1} \quad (2.76)$$

In the Thomson limit, the gamma-ray flux at E_{IC}^b for $t \gtrsim t_{\text{SD}}$ is roughly

$$F_{\text{IC}}^b \sim 3.7 \times 10^{-8} \text{ GeV cm}^{-2} \text{ s}^{-1} B_{\text{dip},14}^{-2} \epsilon_e \frac{Y}{1+Y} \left(\frac{Z_{\text{eff}} + 1}{3} \right)^{-1} \\ \times \left(\frac{M_{\text{ej}}}{5M_{\odot}} \right)^{-1} \left(\frac{V_{\text{ej}}}{5000 \text{ km s}^{-1}} \right)^2 \left(\frac{d}{16.5 \text{ Mpc}} \right)^{-2} \left(\frac{t}{t_{\gamma-\text{bo}}} \right)^{-2} \quad (2.77)$$

Note that the ejecta becomes optically thin to Thomson scattering at

$$t_{\text{HX-bo}} \simeq 420 \text{ days} \left(\frac{2}{\mu_e} \right)^{1/2} \left(\frac{M_{\text{ej}}}{5M_{\odot}} \right)^{1/2} \left(\frac{V_{\text{ej}}}{5000 \text{ km s}^{-1}} \right)^{-1} \quad (2.78)$$

The synchrotron flux at late times is estimated to be

$$F_{\text{syn}}^b \sim 2.6 \times 10^{-12} \text{ erg cm}^{-2} \text{ s}^{-1} B_{\text{dip},14}^{-2} (1+Y)^{-1} \left(\frac{2}{\mu_e} \right)^{-1} \\ \times \left(\frac{M_{\text{ej}}}{5M_{\odot}} \right)^{-1} \left(\frac{V_{\text{ej}}}{5000 \text{ km s}^{-1}} \right)^2 \left(\frac{d}{16.5 \text{ Mpc}} \right)^{-2} \left(\frac{t}{t_{\text{HX-bo}}} \right)^{-2} \quad (2.79)$$

It is worth noting that low-energy photons with low K_{γ} can escape earlier after experiencing multiple scatterings.

In the radio band, where we have synchrotron radiation, the important attenuation or suppression processes are the Razin effect, free-free absorption, and synchrotron self-absorption. The Razin effect (Razin 1960) is a low-energy cut-off of synchrotron emission due to the suppression of relativistic beaming. In a medium, the critical angle for the beaming effect is

$$\theta_b \sim \sqrt{1 - n_r^2 \beta^2} \quad (2.80)$$

where n_r is the refractive index of the medium and β is v_e/c (Rybicki & Lightman 1979). If n_r is close to unity, then θ_b depends mostly on β , which is the vacuum case. If n_r deviates strongly from unity, then

$$\theta_b \sim \sqrt{1 - n_r^2} = \frac{\Omega_p}{\Omega}, \quad (2.81)$$

where

$$\Omega_p = \sqrt{\frac{4\pi n_e e^2}{m_e}} \quad (2.82)$$

is the plasma frequency of the medium. The Razin frequency, where this effect becomes prevalent, is (Ginzburg & Syrovatskii 1965; Murase et al. 2014)

$$\Omega_R = \frac{4\pi e c n_e}{B}. \quad (2.83)$$

At higher frequencies, θ_b decreases until it becomes $1/\gamma$, the vacuum value. At lower frequencies, the synchrotron spectrum will experience a quasi-exponential cutoff due to the increase in θ_b (Boischoit & Clavelier 1967).

Synchrotron emission can be reabsorbed by neighboring electrons within the PWN, causing the region to become optically thick to its own radiation at low frequencies;

this is called self-absorption (Yang et al. 2016). This can be expressed as the brightness temperature

$$T_b = \frac{I_\nu c^2}{2k_B \nu^2}, \quad (2.84)$$

where I_ν is the specific synchrotron intensity, approaching the electron temperature

$$T_e = \left(\frac{2\pi m_e c \nu}{eB} \right)^{1/2} \frac{m_e c^2}{3k_B} = 1.18 \times 10^6 \text{ K} \left(\frac{\nu}{\text{Hz}} \right)^{1/2} \left(\frac{B}{\text{G}} \right)^{-1/2}. \quad (2.85)$$

Setting them equal gives the spectral index for self-absorbed radiation,

$$I_\nu = \frac{2k_B T_e \nu^2}{c^2} \propto \nu^{5/2} B^{-1/2}. \quad (2.86)$$

In general, the self-absorption optical depth is (Murase et al. 2016)

$$\tau_{\text{sa}}^{\text{nb}} = R_w \int d\gamma_e \frac{dn_e^{\text{nb}}}{d\gamma_e} \sigma_{\text{sa}}(\nu, \gamma_e), \quad (2.87)$$

where the self-absorption cross-section is (Ghisellini & Svensson 1991)

$$\sigma_{\text{sa}}(\nu, \gamma_e) = \frac{1}{2m_e \nu^2 \gamma_e p_e} \frac{\partial}{\partial \gamma_e} [\gamma_e p_e j_{\text{syn}}(\nu, \gamma_e)], \quad (2.88)$$

where j_{syn} is the synchrotron emissivity and p_e is the electron momentum.

Photons can be absorbed by electrons in the presence of an ion in an inverse process of bremsstrahlung, known as free-free absorption. From Kirchhoff's law, $j_\nu = 4\pi \kappa_\nu^{\text{abs}} B_\nu(T)$, we get

$$\kappa_\nu^{\text{abs}} \propto \rho T^{-1/2} \nu^{-3} (1 - e^{-h\nu/k_B T}), \quad (2.89)$$

where the factor $T^{-1/2}$ appears because a larger ion thermal velocity will lead to a higher chance of absorption (Ostlie & Carroll 1996). A more complete calculation, accounting for stimulated emission, gives (Shu 1991)

$$\rho \kappa_{\nu, ff} = \sum_i n_{Z_i} n_e \left(\frac{2m_e}{3\pi k_B T} \right)^{1/2} \left(\frac{4\pi Z_i^2 e^6}{2m_e^2 c h \nu^3} \right) g_{ff}(\nu) (1 - e^{-h\nu/k_B T}), \quad (2.90)$$

where $g_{ff}(\nu)$ is a quantum-mechanical correction called the Gaunt factor (Gaunt 1930). This clearly depends on chemical composition, so we use X and Z : the mass fractions of hydrogen and all elements heavier than helium (usually called the metallicity), respectively. A numerical fit of the frequency integral of Equation 2.90 yields Kramer's Law (Kramers 1923; Shu 1991) in the form

$$\kappa_{ff} = 4 \times 10^{22} \text{ cm}^2 \text{ g}^{-1} g_{ff}(1-Z)(1+X) \left(\frac{\rho}{\text{g cm}^{-3}} \right)^{1/2} \left(\frac{T}{\text{K}} \right)^{-7/2}. \quad (2.91)$$

The resulting optical depth is (Murase et al. 2017b)

$$\tau_{ff} = 8.4 \times 10^{-28} T_{e4}^{-1.35} \nu_{10}^{-2.1} \int dr n_e n_i \bar{Z}^2. \quad (2.92)$$

where \bar{Z} is the effective charge of the ejecta. Using (Murase et al. 2017a)

$$n_i = n_e = \frac{3M_{\text{ej}}}{4\pi R_{\text{ej}}^3 \bar{A} m_H}, \quad (2.93)$$

where \bar{A} is the mean nuclear number of the ejecta, and setting $\tau_{ff} = 1$ gives the radio escape time

$$t_{\text{rad-bo}} \sim 30 \text{ yr } T_{e,4}^{-0.27} v_{10}^{-0.42} \left(\frac{M_{\text{ej}}}{5M_{\odot}} \right)^{2/5} \left(\frac{V_{\text{ej}}}{5000 \text{ km s}^{-1}} \right)^{-1} \left(\frac{Z}{4.5} \right)^{2/5} \left(\frac{\bar{A}}{16} \right)^{-1/5}. \quad (2.94)$$

2.2 Dust

In the late phase after a pulsar-driven supernova explosion, dust particles can form by the nucleation of gas molecules into a mesoscopic grain and grow via the further accretion of un-nucleated gas. Without an external energy source, this dust will quickly cool and its emission will not be detectable. However, in the presence of a pulsar, dust that is not sublimated can emit at a higher blackbody temperature, perhaps at a detectable flux. The thermodynamics based model we use for dust nucleation and accretion was developed by Nozawa & Kozasa (2013) for a supernova with a simple power law temperature and concentration evolution, but can be used with our more complicated evolution; we present this model in Section 2.2.1. The criteria for sublimation was developed by Waxman & Draine (2000) for use in a gamma ray burst, but can also be used in a spherical explosion; we present this criteria in Section 2.2.2. Finally, the dust emission is thermal and we derived the formulas based on simple optical depth and blackbody considerations; we present these in Section 2.2.3.

2.2.1 Dust Formation

The model for dust formation is the steady-state model, first developed by Kozasa & Hasegawa (1987) by introducing the concept of a key species or key molecule, which has the lowest collisional frequency among gaseous reactants, and then generalized by Nozawa & Kozasa (2013), whose formulation we take here. In this formulation, collisions between gaseous key molecules and clusters of n key molecules, which we refer to as n -mers, control the reaction kinetics.

Introduction

As the gas cools, dust condensation proceeds via the formation of clusters and subsequent attachment of key molecules to those clusters. The time evolution of the concentration of n -mers $c(n, t) = c_n$ is given by

$$\frac{dc_n}{dt} = J_n(t) - J_{n+1}(t) \text{ for } 2 \leq n \leq n_*, \quad (2.95)$$

where $J_n(t)$ is the net current density from $(n-1)$ -mer to n -mer. We consider that any cluster composed of more than n_* key molecules can be treated as a macroscopic dust grain.

The growth rate of grains, which we assume are spherical, is given by

$$\frac{da}{dt} = s\zeta \left(\frac{k_B T_{\text{gas}}}{2\pi m_1} \right)^{\frac{1}{2}} c_1 \left(1 - \frac{1}{S} \right), \quad (2.96)$$

where m_1 is the mass of the key molecule, a is the grain radius, s is the sticking probability of the key molecule onto grains, ζ is the volume of the condensate per key molecule, k_B is the Boltzmann constant, T_{gas} is the gas temperature, and S is the supersaturation ratio

$$\ln S = \frac{1}{k_B T_{\text{gas}}} (\dot{g}_c - \Delta \dot{g}_{\text{gas}}) + \ln \left(\frac{p_1}{p_s} \right) + \ln \Xi \quad (2.97)$$

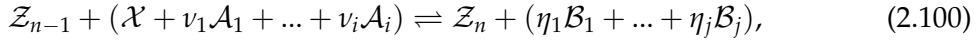
$$= \frac{A}{T_{\text{gas}}} - B + \ln \left(\frac{c_1 k_B T_{\text{gas}}}{p_s} \right) + \ln \Xi, \quad (2.98)$$

where A and B are thermodynamic constants given in Nozawa et al. (2003), p_s is the standard thermodynamic pressure $1 \text{ bar} = 10^6 \text{ Ba}$, \dot{g}_c and $\Delta \dot{g}_{\text{gas}}$ are defined later, and

$$\Xi = \frac{\prod_{k=1}^i (p_k^A / p_s)^{\nu_k}}{\prod_{k=1}^j (p_k^B / p_s)^{\eta_k}}, \quad (2.99)$$

where ν_k and η_k are the stoichiometric coefficients and p_k^A and p_k^B ($k = 1 - i$ and $1 - j$ respectively) are the partial pressures for the gaseous reactants and products, \mathcal{A}_k and \mathcal{B}_k , respectively, in the chemical reaction below.

For dust nucleation, we consider the general chemical reaction



where \mathcal{Z}_n is an n -mer cluster generated from the nucleation of n key molecules \mathcal{X} . From now, we denote quantities of the reactants and products with superscript A and B , similar to p_k^A and p_k^B in Equation 2.99.

Formation of a Dimer

Since collisions of key molecules control the kinetics of the chemical reaction, the current density for the formation of a dimer, $J_2(t)$, can be expressed

$$J_2 = \alpha_1 c_1^2 - \beta_2 c_2 \left(\frac{\sum_{k=1}^j (c_k^B)^{\eta_k}}{\sum_{k=1}^i (c_k^A)^{\nu_k}} \right)^2, \quad (2.101)$$

with α and β being the forward and backward reaction coefficients. This form is based on detailed balance, where

$$\frac{\alpha_1}{\beta_2} = K = \dot{c}_2 \left(\frac{\sum_{k=1}^j (\dot{c}_k^B)^{\eta_k}}{\sum_{k=1}^i (\dot{c}_k^A)^{\nu_k}} \right)^2, \quad (2.102)$$

in chemical equilibrium. This allows the current density to be expressed

$$J_2 = \alpha_1 c_1^2 \left(c_1 - c_2 \frac{c_1}{\dot{c}_2 b^2} \right), \quad (2.103)$$

where

$$b = \frac{c_1 \sum_{k=1}^i (c_k^A / \dot{c}_k^A)^{\nu_k}}{\dot{c}_1 \sum_{k=1}^j (c_k^B / \dot{c}_k^B)^{\eta_k}} = \frac{p_1 \sum_{k=1}^i (p_k^A / \dot{p}_k^A)^{\nu_k}}{\dot{p}_1 \sum_{k=1}^j (p_k^B / \dot{p}_k^B)^{\eta_k}}, \quad (2.104)$$

where \hat{c}_k^A and \hat{c}_k^B (\hat{p}_k^A and \hat{p}_k^B) are the concentrations (gas pressures) of the k th gaseous reactants and products, respectively, in the gas in thermodynamic equilibrium at a temperature T . The factor $c_1/\hat{c}_2 b^2$ can be rewritten as

$$\frac{p_s}{\hat{p}_2} \left(\frac{\hat{p}_1}{p_s} \right)^2 \left(\frac{\sum_{k=1}^i (\hat{p}_k^A / p_s)^{\nu_k}}{\sum_{k=1}^j (\hat{p}_k^B / p_s)^{\eta_k}} \right)^2 = \frac{c_1 \Pi}{\hat{c}_2 b^2} \left(\frac{p_1 \Xi}{p_s} \right)^{2 - \frac{1}{\omega}}, \quad (2.105)$$

where

$$\Pi = \left(\frac{\prod_{k=1}^i (c_k^A / c_1)^{\nu_k}}{\prod_{k=1}^j (c_k^B / c_1)^{\eta_k}} \right)^{\frac{1}{\omega}} \quad (2.106)$$

and

$$\omega = 1 + \sum_{k=1}^i \nu_k - \sum_{k=1}^j \eta_k. \quad (2.107)$$

We apply the law of mass action, which states that the rate of a chemical reaction is directly proportional to the product of the activities or concentrations of the reactants, to find

$$\frac{p_s}{\hat{p}_2} \left(\frac{\hat{p}_1}{p_s} \right)^2 \left(\frac{\sum_{k=1}^i (\hat{p}_k^A / p_s)^{\nu_k}}{\sum_{k=1}^j (\hat{p}_k^B / p_s)^{\eta_k}} \right)^2 = \exp \left(\frac{1}{k_B T_{\text{gas}}} (\hat{g}_2 - 2\Delta \hat{g}_{\text{gas}}) \right), \quad (2.108)$$

with

$$\Delta \hat{g}_{\text{gas}} = \hat{g}_1 + \sum_{k=1}^i \nu_k \hat{g}_k^A - \sum_{k=1}^j \eta_k \hat{g}_k^B, \quad (2.109)$$

where \hat{g}_k^A and \hat{g}_k^B are the chemical potentials of k th gaseous reactants and products at a standard pressure p_s , respectively. Using this, Equation 2.105 can be rewritten

$$\frac{c_1 \Pi}{\hat{c}_2 b^2} = \exp \left(\frac{1}{k_B T_{\text{gas}}} (\hat{g}_2 - 2\Delta \hat{g}_{\text{gas}}) - \left(2 - \frac{1}{\omega} \right) \left[\ln \left(\frac{p_1}{p_s} \right) + \ln \Xi \right] \right) \quad (2.110)$$

$$= \exp(\gamma_2) \quad (2.111)$$

where

$$\gamma_2 = \frac{1}{k_B T_{\text{gas}}} \left[\hat{g}_2 - \left(2 - \frac{1}{\omega} \right) \hat{g}_c - \frac{1}{\omega} \Delta \hat{g}_{\text{gas}} \right] - \left(2 - \frac{1}{\omega} \right) \ln S \quad (2.112)$$

where \hat{g}_c is the chemical potential of the bulk condensate at p_s . Finally, this allows us to rewrite Equation 2.103 as

$$J_2 = \alpha_1 c_1^2 \left(c_1 - c_2 \frac{1}{\Pi} \exp(\gamma_2) \right), \quad (2.113)$$

Steady State Approximation

For $3 \leq n \leq n_*$, the current density $J_n(t)$ is

$$J_n(t) = \alpha_{n-1}c_{n-1}c_1 - \beta_n c_n \frac{\sum_{k=1}^j (c_k^B)^{\eta_k}}{\sum_{k=1}^i (c_k^A)^{\nu_k}}, \quad (2.114)$$

$$= \alpha_{n-1}c_1 \left(c_{n-1} - c_n \frac{\dot{c}_{n-1}}{\dot{c}_n b} \right). \quad (2.115)$$

Rewriting in a similar way as Equations 2.110 and 2.113 gives

$$\frac{\dot{c}_{n-1}}{\dot{c}_n b} = \exp \left[\frac{1}{k_B T_{\text{gas}}} (\dot{g}_n - \dot{g}_{n-1} - \Delta \dot{g}_{\text{gas}}) - \ln \left(\frac{p_1}{p_s} \right) + \ln \Xi \right] \quad (2.116)$$

and

$$J_n = \alpha_{n-1}c_1 ((c_{n-1} - c_n \exp(\gamma_n))). \quad (2.117)$$

In the steady state approximation, the current density J_n is independent of n , being equal to the steady-state nucleation rate J_s . Using this equivalency, Equations 2.103 and 2.115 lead to the following relations, respectively:

$$\frac{J_s}{\alpha_1 c_1^2} = 1 - \frac{c_2}{\dot{c}_2 b^2} \quad (2.118)$$

$$\frac{J_s}{\alpha_{n-1} c_1 \dot{c}_{n-1}} = \frac{c_{n-1}}{\dot{c}_{n-1}} - \frac{c_n}{\dot{c}_n b} \text{ for } n \geq 3. \quad (2.119)$$

By summing up these two equations multiplied by $1/b^{n-1}$, J_s can be derived from

$$J_s \left(\frac{1}{\alpha_1 c_1^2} + \sum_{i=2}^n \frac{1}{\alpha_i c_1 \dot{c}_i b^i} \right) = 1 - \frac{c_n}{\dot{c}_n b^n}. \quad (2.120)$$

Using Equations 2.110 and 2.116, $1/\dot{c}_n b^n$ can be rewritten

$$\frac{1}{\dot{c}_n b^n} = \frac{1}{c_1 \Pi} \exp \left[\frac{1}{k_B T_{\text{gas}}} (\dot{g}_n - n \Delta \dot{g}_{\text{gas}}) - \left(n - \frac{1}{\omega} \right) \left(\ln \left(\frac{p_1}{p_s} \right) + \ln \Xi \right) \right] \equiv \frac{1}{c_1 \Pi} \exp(\gamma'_n) \quad (2.121)$$

with

$$\gamma'_n = \frac{1}{k_B T_{\text{gas}}} \left[(\dot{g}_n - \left(n - \frac{1}{\omega} \right) \dot{g}_c - \frac{1}{\omega} \Delta \dot{g}_{\text{gas}}) - \left(n - \frac{1}{\omega} \right) \ln S \right]. \quad (2.122)$$

Since the right-hand side of Equation 2.120 goes to zero as $n \rightarrow \infty$ if $S > 1$, J_s for large n becomes

$$\frac{1}{J_s} = \frac{1}{\alpha_1 c_1^2} + \sum_{i=2}^{\infty} \frac{1}{\alpha_i c_1 \dot{c}_i b^i} = \frac{1}{\alpha_1 c_1^2} + \sum_{i=2}^{\infty} \frac{1}{\alpha_i c_1^2 \Pi} \exp(\gamma'_i). \quad (2.123)$$

The summation can be replaced by an integration if $1/\alpha c_1^2 \ll 1$, which gives

$$\frac{1}{J_s} \simeq \frac{1}{c_1^2 \Pi} \int_2^{\infty} \frac{1}{\alpha_i} \exp(\gamma'_i) di. \quad (2.124)$$

In principle, the nucleation rate J_s can be calculated once the chemical potentials of the n -mers are given, but unfortunately these potentials are only available for small

($n \lesssim 5$) clusters for a few materials of interest (e.g., Goumans & Bromley 2012). Therefore, we must use the capillary approximation, which allows us to estimate the chemical potential of an n -mer in terms of the chemical potential and surface energy of a monomer in the bulk condensate (Abraham 1974; Blander & Katz 1972). This approximation expresses \dot{g}_n as

$$\dot{g}_n = 4\pi a_o^2 \sigma_{\text{ten}} (n-1)^{2/3} + (n-1)\dot{g}_c + \dot{g}_1 \quad (2.125)$$

for a single element grain (e.g., Yasuda & Kozasa 2012), where σ_{ten} is the surface tension of the bulk condensate and $a_o = (3\zeta/4\pi)^{1/3}$ is the hypothetical grain radius per key molecule, which are both given or calculated in Nozawa et al. (2003). In a multi-element grain, where the factor $1/\omega$ represents the contribution of the key molecule to the change of chemical potential, a slightly more complicated expression arises:

$$\dot{g}_n = 4\pi a_o^2 \sigma_{\text{ten}} \left(n - \frac{1}{\omega}\right)^{2/3} + \left(n - \frac{1}{\omega}\right)\dot{g}_c + \frac{1}{\omega}\Delta\dot{g}_{\text{gas}}. \quad (2.126)$$

Using this approximation, γ'_n from Equation 2.124 can be expressed as

$$\gamma'_n = \mu \left(n - \frac{1}{\omega}\right)^{2/3} - \left(n - \frac{1}{\omega}\right) \ln S, \quad (2.127)$$

where $\mu = 4\pi a_o^2 \sigma_{\text{ten}} / kT_{\text{gas}}$. This has a maximum at n_{crit} , which is given by

$$\left(n_{\text{crit}} - \frac{1}{\omega}\right)^{1/3} = \frac{2}{3} \frac{\mu}{\ln S}. \quad (2.128)$$

Thus, Equation 2.124 can be integrated with the saddle-point method, resulting in a nucleation rate

$$J_s = s_{n_{\text{crit}}} \zeta \left(\frac{2\sigma_{\text{ten}}}{\pi m_{n_{\text{crit}},1}}\right)^{\frac{1}{2}} \frac{n_{\text{crit}}^{2/3}}{(n_{\text{crit}} - 1/\omega)^{2/3}} c_1^2 \Pi \exp\left(-\frac{4}{27} \frac{\mu^3}{(\ln S)^2}\right). \quad (2.129)$$

and, for $n_{\text{crit}} \gg 1$,

$$J_s = s \zeta \left(\frac{2\sigma_{\text{ten}}}{\pi m_1}\right)^{\frac{1}{2}} c_1^2 \Pi \exp\left(-\frac{4}{27} \frac{\mu^3}{(\ln S)^2}\right). \quad (2.130)$$

This steady state nucleation closely approximates the non-steady state model in Nozawa & Kozasa (2013) if

$$\Lambda = \frac{\tau_{\text{sat}}}{\tau_{\text{coll}}} = \left(\frac{d \ln S}{dt}\right)^{-1} \left(s 4\pi a_o^2 \tilde{c}_1 \sqrt{\frac{k_B T_{\text{gas}}}{2\pi m_1}}\right) \quad (2.131)$$

$$\sim \frac{C}{\gamma - 1} \left(\frac{s}{1.0}\right) \left(\frac{\tilde{c}_1}{10^8 \text{ cm}^{-3}}\right) \left(\frac{T_{\text{gas}}}{2000 \text{ K}}\right)^{\frac{3}{2}} \left(\frac{t}{300 \text{ days}}\right) \quad (2.132)$$

is greater than ~ 30 at the time at dust formation onset. Here, C is a constant that depends on grain composition (1.94×10^3 for C grains and 1.15×10^3 for MgSiO₃ grains; here we use 1.5×10^3 for everything), and \tilde{c}_1 is the gas concentration if no dust is formed. This expression assumes a temperature evolution of

$$T_{\text{gas}} = T_{\text{gas},0} \left(\frac{t}{t_0} \right)^{-3(\gamma-1)}, \quad (2.133)$$

but ours is much more complicated due to the pulsar's energy injection. Therefore, we need to approximate γ in this expression. If $\Lambda < 30$, then the steady state model we use predicts earlier formation and smaller overall grain size (see Nozawa & Kozasa (2013) Figures 4 and 5 for examples); this usually happens with lower density ejecta.

Cluster Formation

Once J_s is calculated, dividing by \tilde{c}_1 gives us I_s , which is used to calculate

$$\frac{dK_i}{dt} = \begin{cases} I_s(t)n_*^{\frac{i}{3}} + \frac{i}{a_0} \left(\frac{da}{dt} \right) K_{i-1} & \text{for } i = 1 - 3 \\ I_s(t) & \text{for } i = 0. \end{cases}$$

Here K_0 represents the number density of dust grains ($K_0 = n_{\text{dust}}/\tilde{c}_1$), and K_3 represents the number fraction of key molecules locked in dust grains. Therefore, we can calculate the condensation efficiency $f_{\text{con}}(t)$ and average radius $a_{\text{ave}}(t)$ by

$$f_{\text{con}} = K_3, \quad (2.134)$$

$$a_{\text{ave}} = a_0 \left(\frac{K_3}{K_0} \right)^{\frac{1}{3}}. \quad (2.135)$$

2.2.2 Criteria for Dust Sublimation

Once the gas has cooled enough for dust to form, the dust can still be sublimated by the PWN optical-UV emission. If we assume that the cloud is optically thin in the optical-UV band, then a dust grain must be in radiative equilibrium between absorbing PWN emission and emitting thermally in the IR. The equation for this equilibrium is

$$\frac{L_{\text{opt/UV}}}{4\pi\sigma r^2} Q_{\text{opt/UV}} \pi a^2 = \langle Q \rangle_T 4\pi a^2 \sigma T_{\text{dust}}^4 \quad (2.136)$$

where $L_{\text{opt/UV}}$ is the non-thermal luminosity in the band between 1-7.5 eV, σ is the Stefan-Boltzmann constant, r is the radius of the dust grain's position, $Q_{\text{opt/UV}}$ is the absorption efficiency factor averaged over the optical/UV spectrum, which we assume is ≈ 1 since the grain radii should be $\gtrsim 10^{-5}$ cm, and finally

$$\langle Q \rangle_T = \frac{B_\nu(T_{\text{dust}}) Q_{\text{abs},\nu} d\nu}{B_\nu(T_{\text{dust}}) d\nu} \quad (2.137)$$

$$\approx \frac{Da_{-5}(T_{\text{dust}}/2300 \text{ K})}{1 + Da_{-5}(T_{\text{dust}}/2300 \text{ K})}, \quad (2.138)$$

where $a_{-5} = a/10^{-5}$ and D is a constant (0.3 for C dust grains, 0.03 for silicates; we use 0.1 for all grains) (Draine & Lee 1984). Dust will be sublimated if its equilibrium temperature is greater than the critical temperature T_c for supersaturation, which can be calculated by setting $S = 1$ in Equation 2.98. From Equation 2.136, the critical radius for dust sublimation is

$$R_c = \left(\frac{L_{\text{opt/UV}} Q_{\text{opt/UV}}}{16\pi\sigma T_c^4 \langle Q \rangle_{T_c}} \right)^{\frac{1}{2}}. \quad (2.139)$$

Dust will be sublimated out to R_c , and if $R_c < R_{\text{ej}}$, then no dust can be formed at all due to sublimation from the PWN emission.

2.2.3 Dust Emission

Once dust can start to form without being sublimated, it emits thermally in the infrared. The optical-UV optical depth

$$\tau_{\text{opt/UV}} = \int_{R_c}^{R_{\text{ej}}} n_{\text{dust}} \pi a^2 dr \quad (2.140)$$

$$= n_{\text{dust}} \pi a^2 (R_{\text{ej}} - R_c) \quad (2.141)$$

is key to determine whether the dust emission is isothermal or not.

If $\tau_{\text{opt/UV}} \gg 1$, then all the emission will be absorbed in a thin shell just outside R_c and will emit just below T_c with a blackbody luminosity

$$L_\nu = 4\pi R_c^2 Q(a) \pi \frac{2h\nu^3}{c^2} \frac{1}{e^{\frac{h\nu}{k_B T_c}} - 1}, \quad (2.142)$$

where $Q(a)$ is the frequency-dependent dust emissivity (Tóth et al. 2013)

$$Q(a) = \left(\frac{2\pi a \nu}{c} \right)^\beta, \quad 1 \leq \beta \leq 2. \quad (2.143)$$

Since the re-emission is longer wavelength than the absorbed PWN emission, and longer the typical size of the dust grains, the rest of the dust will appear optically thin for this re-emission, and the blackbody emission at T_c will be directly observable.

If $\tau_{\text{opt/UV}} \ll 1$, then all dust grains will be in thermal equilibrium with temperatures given by Equation 2.136, and the emission in each radial shell will have luminosity

$$dL_\nu = 4\pi r^2 n_{\text{dust}} 4\pi a^2 Q(a) \pi \frac{2h\nu^3}{c^2} \frac{1}{e^{\frac{h\nu}{k_B T(r)}} - 1} dr, \quad (2.144)$$

and the overall luminosity can be obtained by integrating over r from R_c to R_{ej} . This integral is possible to do analytically, and a full derivation is given in Appendix A. The final expression is

$$L_\nu = \frac{64\pi^3 n_{\text{dust}} Q(a) k_B^6 T_c^3 R_c^3}{h^5 \nu^3 c^2} \sum_{n=1}^6 \frac{120x^{(6-n)}}{(6-n)!} \text{Li}_n(e^{-x}) \Bigg|_{x=\frac{h\nu}{k_B T(R_{\text{ej}})}}^{x=\frac{h\nu}{k_B T_c}}, \quad (2.145)$$

where $\text{Li}_s(z)$ is a polylogarithmic function of order s .

When $\tau_{\text{opt/UV}} \sim 1$, the spectrum of the emission is difficult to derive without a full treatment of multiple scattering. For simplicity, we use Equation 2.142 for $\tau_{\text{opt/UV}} > 1$ and Equation 2.145 for $\tau_{\text{opt/UV}} \leq 1$. From energy conservation, we know that the total power radiated from dust should be constant for any $\tau_{\text{opt/UV}} > 1$, so Equation 2.142 represents the best possible case for detection, as the frequency range of the isothermal emission will be smaller than a non-isothermal spectrum.

Chapter 3

Radio Emission from Embryonic SLSN Remnants

There have been previous arguments that Type-I SLSNe are powered by central engines which inject energy for a long period of time after the core-collapse of the progenitor star. A popular hypothesis is that the engine is a rapidly-rotating pulsar with a magnetic field between $10^{13} - 10^{15}$ G, but quasi-thermal optical emission can not differentiate this from other possible engines. Murase et al. (2016) proposed that radio/submm emission from non-thermal positron-electron pairs in the newborn PWN can be used to identify and characterize pulsars in the supernovae they power. Here, we focus on six bright newborn SLSN-I remnants, and examine the constraints placed by radio and submm emission. We find that the Atacama Large Millimeter/submillimetre Array (ALMA) can detect the submm PWN emission from most of them in a few years after the explosion, while the Jansky Very Large Array (VLA) can detect the radio PWN emission in a few decades. Follow-up observations could help solve the parameter degeneracy problem in the pulsar-powered SN model and could give clues about young neutron stars scenarios for SLSNe-I and FRBs.

This chapter is based on Omand et al. (2017), and the work was done in collaboration with Kazumi Kashiyama and Kohta Murase.

3.1 Introduction

SLSNe are extremely rare, but are the most luminous optical/UV transients associated with the deaths of massive stars (e.g., Gal-Yam 2012). They are divided into two broad groups based on the presence of hydrogen in the observed spectra. The ones with hydrogen (Type-II) are likely powered by the circumstellar shock between the SN ejecta and the hydrogen-rich envelope (e.g., Chevalier & Irwin 2011; Smith & McCray 2007), while the ones devoid of hydrogen (Type-I) are thought to originate from massive Wolf-Rayet progenitors and be driven by a central engine, either a rapidly-rotating pulsar (e.g., Kasen & Bildsten 2010; Woosley 2010) or an accreting black hole (Dexter & Kasen 2013).

The pulsar-driven model is useful for explaining the diversity of explosions associated with the deaths of massive stars (see Chapter 1). Models have used pulsars with millisecond periods and strong magnetic fields to power GRBs, HNe, and broad-line Type-Ibc SNe (e.g., Thompson et al. 2004). The GRB-SN was extended to more luminous types after the discovery of an SLSN-like optical counterpart to an ultra-long GRB (Greiner et al. 2015; Metzger et al. 2015). Stripped-envelope SNe, including ordinary Type-Ibc SNe, may also be powered by pulsars with high magnetic fields. The magnetar formation rate is estimated to be $\sim 10\%$ of the core-collapse SN rate

(Keane & Kramer 2008), and the observed Galactic magnetars with slow rotation periods now could be explained by the formation of highly magnetic NSs with relatively low initial spin periods of $\gtrsim 10$ ms (Kashiyama et al. 2016). In order for us to better understand how rapidly-rotating pulsars and magnetars are formed, it is important to understand the diversity of Type-I and stripped-envelope SNe (SLSNe, HNe, and Type-Ibc SNe).

SNe can generally be powered by the decay of radioactive nuclei, but this leads to a parameter degeneracy when only using optical/UV light curve information. Thus, non-thermal emission can be a useful tool to find hidden compact objects, and galactic PWNe are known to efficiently accelerate electrons and positrons (e.g., Gaensler & Slane 2006; Tanaka & Takahara 2010), which makes non-thermal PWN emission a smoking gun for detection of a nascent neutron star.

If spin-down energy is efficiently converted into radiation, as required by the pulsar-powered SN model, it is natural that they would be luminous in the x-ray and gamma-ray bands. The model predicts synchrotron x-rays from leptons accelerated by the PWN provide the most promising signals, with both soft x-ray (Metzger et al. 2014) and hard x-ray (Kashiyama et al. 2016) emission being detectable by current x-ray telescopes such as *Swift* and *NuSTAR*. Searches for x-ray PWN emission have been done previously, and some tentative candidates have been proposed (Margutti et al. 2017b; Perna et al. 2008; Perna & Stella 2004). However, the detectability of the x-ray emission, especially in the soft x-ray band, depends on the plasma properties of the SN ejecta, and the current x-ray measurements are not very constraining. Higher energy gamma-rays, which are produced via inverse-Compton scattering with thermal SN photons (Kotera et al. 2013; Murase et al. 2015), are a more direct probe for a hidden pulsar, but detection of these signals is more challenging.

Radio emission is an alternate probe of particle acceleration in young PWNe within the SN ejecta. Murase et al. (2016) calculated synchrotron emission from young PWNe and various effects of gamma-ray and radio attenuation, and also considered the connection to FRBs. Murase et al. (2016) showed that quasi-steady radio/submm emission from PWNe embedded in SN remnants should be detectable with current facilities such as ALMA and VLA. Since young NSs are thought to also be candidate progenitors of FRBs, follow-up observations searching for persistent radio/submm counterparts of FRBs in SN remnants were proposed to investigate a possible link. Recent observations of the repeating FRB 121102 led to the localization of its host galaxy and the discovery of a persistent radio counterpart, which was seen by VLA and the European Very Long Baseline Interferometry (VLBI) Network (Chatterjee et al. 2017; Marcote et al. 2017; Tendulkar et al. 2017).

The host galaxy of FRB 121102 is a low-metallicity star-forming, which is similar to observed hosts of SLSN-I (Chatterjee et al. 2017; Metzger et al. 2017; Tendulkar et al. 2017). Also, the flux of the persistent radio counterpart of FRB 121102 is broadly consistent with PWN emission from a decades old pulsar-driven SLSN (Kashiyama & Murase 2017; Metzger et al. 2017; Murase et al. 2016). These similarities motivate follow-up radio observations of known pulsar-driven SN candidates targeting the radio PWN emission, and SLSN-I are among the most interesting objects.

In this chapter, we study radio/submm emission from embryonic SLSN remnants for a few decades after the explosion. First, we select some of the brightest known SLSN-I and fit the quasi-thermal optical light curves using the pulsar-driven model (Section 3.2). Then, using the obtained model parameters (initial NS rotation period, initial magnetic field strength of the NS, and ejecta mass), we calculate radio/submm emission from the PWN (Section 3.3). We show the detectability of the PWN emission with VLA and ALMA and discuss possible constraints on the pulsar-driven model.

Name	RA	Dec	z	D_L (Gpc)	Band	References
iPTF13ajg	16:39:03.95	+37:01:38.4	0.7403	4.6736	R	(Vreeswijk et al. 2014)
SN2012il	09:46:12.91	+19:50:28.7	0.175	0.8686	r	(Inserra et al. 2013)
SN2013dg	13:18:41.35	-07:04:43.0	0.1918	0.9615	r	(Nicholl et al. 2014)
SN2010gx	11:25:46.71	-08:49:41.4	0.2297	1.1766	r'	(Pastorello et al. 2010)
SN2011ke	13:50:57.77	+26:16:42.8	0.1428	0.6950	V	(Inserra et al. 2013)
SN2015bn	11:33:41.57	+00:43:32.2	0.1136	0.5427	V	(Nicholl et al. 2016b)

TABLE 3.1: Properties of the SLSNe selected for this study.

3.2 Pulsar-driven Super-luminous Supernovae

In the pulsar-driven model, the source of the energy injected into the SN ejecta is the rotational energy of the newborn pulsar, which manifests as a strongly magnetized relativistic wind. The injected pulsar wind drives forward and reverse shocks, and the reverse shock region is often called a nebula or PWN. In the PWN, the wind dissipates and the electrons and positrons are accelerated to ultra-relativistic energies. The non-thermal emission from these electrons and positrons, as well as heavier leptons, has been studied for many years (e.g., Gaensler & Slane 2006; Tanaka & Takahara 2010). Modeling the Galactic PWNe has shown that most of the spin-down energy is used to accelerate particles, and the accelerated positrons and electrons lose energy via non-radiative adiabatic cooling as well as synchrotron emission and inverse Compton scattering, which gives rise to a broadband spectrum from the radio band to gamma-rays (See Chapter 1).

A natural assumption is that the pulsar wind dissipation and resulting particle acceleration occurs in the early phase of the PWN. However, this initial non-thermal emission is completely down-scattered or absorbed, and diffuses out of the SN ejecta as quasi-thermal SN emission observable in the optical band (Kasen & Bildsten 2010; Woosley 2010). The initial spin period and dipole magnetic field strength of the pulsar can be inferred from the optical light curve (e.g., Inserra et al. 2013; Nicholl et al. 2013; Pastorello et al. 2010). Radio emission can only escape the PWN and dense SN ejecta without severe attenuation after a significant amount of time. In the pulsar-driven model for SNe and SLSNe, radio emission can start to escape at a timescale of around 10 years and submm emission can start to escape at a timescale of around one or two years (See Equation 2.94).

3.2.1 Supernova Samples

We retrieve SLSN data from the Open Supernova catalog¹ (Guillochon et al. 2017), and select sample Type-Ic SLSN which have data points on both sides of the light curve maximum in a single band. There are six SLSNe that fit this criteria; their properties are summarized in Table 3.1 and their light curves are shown in Figure 3.1.

3.2.2 Modeling of Optical Light Curves

To calculate optical light curves, we use the model from Section 2.1.1, which is based heavily on Kashiyama et al. (2016). The model allows us to numerically calculate broadband emission, which accounts for electromagnetic and gravitational wave radiation due to the spin-down of the pulsar, acceleration of the ejecta through the magnetized wind of the PWN, and radioactive decay of ^{56}Ni and ^{56}Co . The model

¹<https://sne.space/>

is calibrated against the classical Arnett model (Arnett 1982) without a pulsar engine, and thus gives similar results (see Kashiyama et al. 2016, Figure 16). Thermalization of non-thermal photons is also taken into account by approximating the results of Murase et al. (2015), which takes simplified particle creation and pair cascades into account.

We vary three model parameters: the initial spin period P of the NS, the initial magnetic field $B_{13} = B/(10^{13} \text{ G})$ of the NS, and the supernova ejecta mass M_{ej} . Other parameters in the model, which we fix for this study, are the ejected nickel mass M_{Ni} , the SN energy E_{SN} , and the ejecta opacity κ ; we set these to $0.1 M_{\odot}$, 10^{51} erg , and 0.1 g cm^{-2} respectively. Changing the ejected nickel mass makes very little difference to the light curve unless $M_{\text{Ni}} \gtrsim 1 M_{\odot}$, and $0.1 M_{\odot}$ is more typical of core collapse supernovae (see, e.g., Drout et al. 2011); the initial explosion energy is typical for ordinary supernovae, but irrelevant in this case, since the energy deposition into the ejecta will be dominated by the rotational energy of the pulsar, which will inject $\gtrsim 10^{52} \text{ erg}$ within a few weeks of the explosion; and the ejecta opacity is still uncertain, but the line opacity implies a value of $0.01\text{-}0.2 \text{ g cm}^{-2}$ at all times, so our value is not off by more than a factor of a few at any time (Inserra et al. 2013; Kleiser & Kasen 2014). We fit the light curves to the model by eye. The fit does not correct for extinction; the known $E(B - V)$ values are all $\lesssim 0.04$ (Guillochon et al. 2017) and the host galaxy extinction is expected to be low, since most SLSN reside in low metallicity dwarf galaxies (Lunnan et al. 2014). The expected luminosity change would be at most 0.15 mag, which will not significantly affect the resulting parameters. Our fits are based on only the brightest 1.5 magnitudes due to the model's low reliability at later times (see Section 2.1.1 for details).

We investigate a parameter range of $M_{\text{ej}} \geq 1.0 M_{\odot}$ and $P \geq 1.0 \text{ ms}$. The mass condition is a reasonable limit for core collapse supernovae while the period condition is close to the mass-shedding limit for neutron stars (Watts et al. 2016). We found that all the sample SLSNe can be fit by a model with $P = 1.0 \text{ ms}$ as shown in Figure 3.1. Coresponding (B_{13}, M_{ej}) are given in Table 3.1, and they range from $B_{13} \sim 1 - 15$ and $M_{\text{ej}} \sim 5 - 15 M_{\odot}$.

However, since $(P, B_{13}, M_{\text{ej}})$ suffer from parameter degeneracy, the SLSN data can be fit by models with a longer initial spin period. The spin-down luminosity of the pulsar is sensitive to the initial spin period; since the peak SN luminosity is determined by the spin-down luminosity at the diffusion time, with $L_{\text{SN}} \propto P^{-1} B^{-2} M_{\text{ej}}^{-3/2}$ if $t_{\text{dif}} \geq t_{\text{SD}}$ and $L_{\text{SN}} \propto P^{-4} B^2$ if $t_{\text{dif}} \leq t_{\text{SD}}$ (See Equations 2.39 and 2.41), a slower period results in a dimmer SN in both cases. A slower spin also suppresses acceleration of the ejecta and results in a longer diffusion time, with $t_{\text{dif}} \propto P^{1/2} M_{\text{ej}}^{3/4}$, thus leading to the peak time of the supernova being longer. These effects, resulting from an increased spin period, can be compensated for by changing the magnetic field and SN ejecta mass.

In Table 3.1, we also show the slowest spin model the fits each light curve. The slowest spin periods that give a reasonable fit to the data range from 1.1 to 4.1 ms depend on SNe; a larger period would either bring the luminosity too low, or bring the magnetic field or ejecta mass low enough where the shape of the light curve would become inconsistent with the observed ones (Figure 3.2).

Our fitting parameters for SN2012il, SN2011ke, and SN2010gx are different from the the ones found in Inserra et al. (2013). Their best-fit models have a larger B field by a factor of ~ 10 and a larger P by a factor of \sim a few. One reason for this discrepancy is that Inserra et al. (2013) uses the classical dipole spin-down formula and we use a formula motivated by numerical simulations (Equation 2.2). The latter gives a factor

Name	B_{13} at 1 ms	$M_{\text{ej}} (M_{\odot})$ at 1 ms	P_{max} (ms)	B_{13} at P_{max}	$M_{\text{ej}} (M_{\odot})$ at P_{max}
iPTF13ajg	1.6	5.0	1.1	1.3	3.5
SN2012il	8.0	7.0	2.4	3.0	1.0
SN2013dg	13.0	14.0	4.1	4.0	1.4
SN2010gx	4.5	10.0	1.6	3.5	3.5
SN2011ke	7.5	9.5	2.4	2.9	1.3
SN2015bn	2.1	17.0	1.4	1.0	5.0

TABLE 3.2: Model parameters of each SN that fit the light curve data. Periods were investigated from 1.0 ms to P_{max} , with any period above P_{max} either not having enough luminosity, having too slow a decline, or having a shape inconsistent with the observed data. Data and fits for $P = 1.0$ ms are shown in Fig. 3.1.

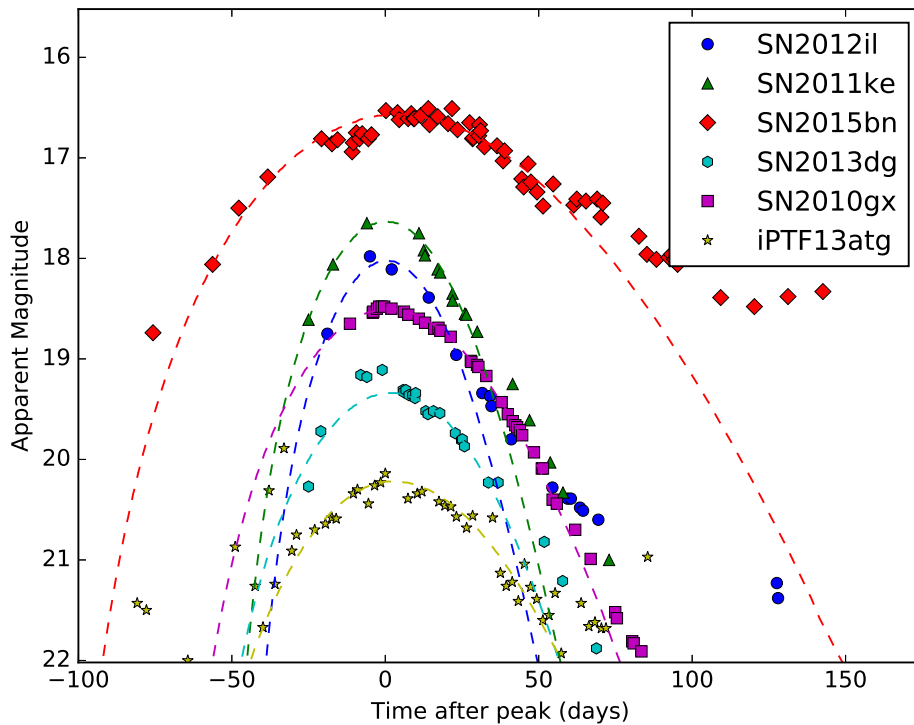


FIGURE 3.1: SN data (points) and modeled optical light curve (dashed lines) for each SN, using their $P = 1$ ms parameter sets given in Table 3.1.

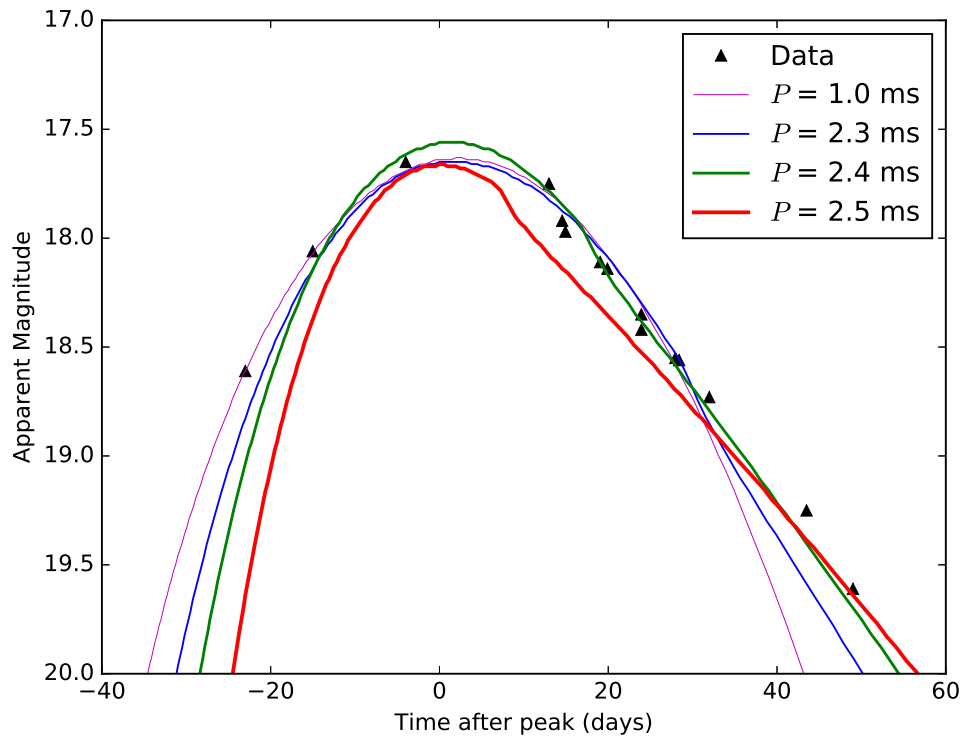


FIGURE 3.2: SN data (points) and modeled optical light curves for SN2011ke, using $(P, B_{13}, M_{\text{ej}}) = (1.0 \text{ ms}, 7.5, 9.5 M_{\odot}), (2.3 \text{ ms}, 3.7, 2 M_{\odot}), (2.4 \text{ ms}, 2.9, 1.3 M_{\odot}),$ and $(2.5 \text{ ms}, 2.1, 0.8 M_{\odot})$. The $P = 1.0, 2.3,$ and 2.4 ms models are considered good fits, while the $P = 2.5$ ms model is not wide enough at the peak and declines too slowly. There are no parameter sets with $P = 2.5$ ms that generate a model that fits the data, so 2.4 ms is considered to be P_{max} .

$3(1 + C \sin^2 \chi_\mu) / 2 \sin^2 \chi_\mu \sim 5$ larger spin-down luminosity than the former for fixed (P, B) (see Kashiyama et al. (2016) and Section 2.1.1 for a discussion). Another reason is that the optical depth of the ejecta in our model is smaller than theirs by a factor of ~ 1.5 for a given M_{ej} , κ , and ejecta radius, which is caused by a different assumption of the SN ejecta profile; their ejecta has a homogeneous core surrounded by a homologous envelope with $\rho \propto v_{\text{ej}}^{-10}$ where v_{ej} is the local velocity of the ejecta, while we only consider a homologous core with $\rho \propto v_{\text{ej}}^{-1}$ (see, e.g., Kasen & Bildsten 2010). These differences should be seen as an inherent uncertainty in the pulsar-driven model.

Testing the pulsar-driven model from only optical/UV light curves is extremely difficult, since the light curve can be produced by a combination of energy sources; this means other engines, such as a black hole accretion disk, are not excluded (Dexter & Kasen 2013). We do not investigate problem any further here; instead we calculate radio and submm non-thermal emission consistently within our framework, and examine possible constraint imposed by multi-wavelength observations.

3.3 Predictions for Radio Emission

In this section, we calculate radio synchrotron emission from pulsar-driven SLSNe using the model parameters determined in Section 3.2. We calculate the early PWN emission in Section 3.3.1 and discuss radio emission from the ejecta forward shock in Section 3.3.2. The radio PWN emission has been calculated previously (see Gaensler & Slane 2006; Tanaka & Takahara 2010, and references therein), but we take into account dynamics of the PWN and SN as well as pair cascades and external attenuation based on Murase et al. (2015, 2016) (See Section 2.1.2).

3.3.1 Radio Emission from Embryonic Nebulae

Over the course of the expansion, non-thermal emission begins to escape the SN ejecta. The timescale for escape is sensitive to photon energy because the opacity and absorption process within the ejecta depends on energy, e.g., bound-free absorption for soft x-rays, inelastic Compton scattering for hard x-rays and MeV gamma-rays, the Bethe-Heitler process for GeV gamma-rays, and photon-photon pair annihilation for higher energy photons.

The details of the PWN spectrum depend on both the injection history of positrons and electrons into the PWN and the ionization state of the ejecta, which are both uncertain for young pulsar-powered SNe. Our model of the injection spectrum is based on Galactic PWNe such as the Crab PWNe (e.g., Tanaka & Takahara 2010), which has a broken power law spectrum with a peak Lorentz factor of $\gamma_{e^\pm, b} = 10^5$ and spectral indices of $q_1 = 1.5$ and $q_2 = 2.5$ (See Equation 2.21).

Since the spectrum lies in the fast cooling regime, where the cooling time of the electrons and positrons with $\gamma_{e^\pm, b}$ is much shorter than the dynamical time, our results are not very sensitive to the spectral indices. The equipartition parameter for the magnetic field energy is assumed to be $\epsilon_B = 0.01$, and the rest of the spin-down energy is assumed to accelerate electrons and positrons, i.e., $\epsilon_e = 0.99$; these assumptions are based on detailed modeling of Galactic PWNe (Tanaka & Takahara 2010, 2013). To take free-free absorption and the Razin effect into account within the SN ejecta we assume a singly-ionized, oxygen-rich ejecta with an electron temperature of $T_e = 10^4$ K, a mean nuclear number of $\bar{A} = 16$, and an effective atomic number of $\bar{Z} = 4.5$ (See Equations 2.92 and 2.94), which takes into account the charge shielding effect; the assumption on the metal abundance is based on the results of previous

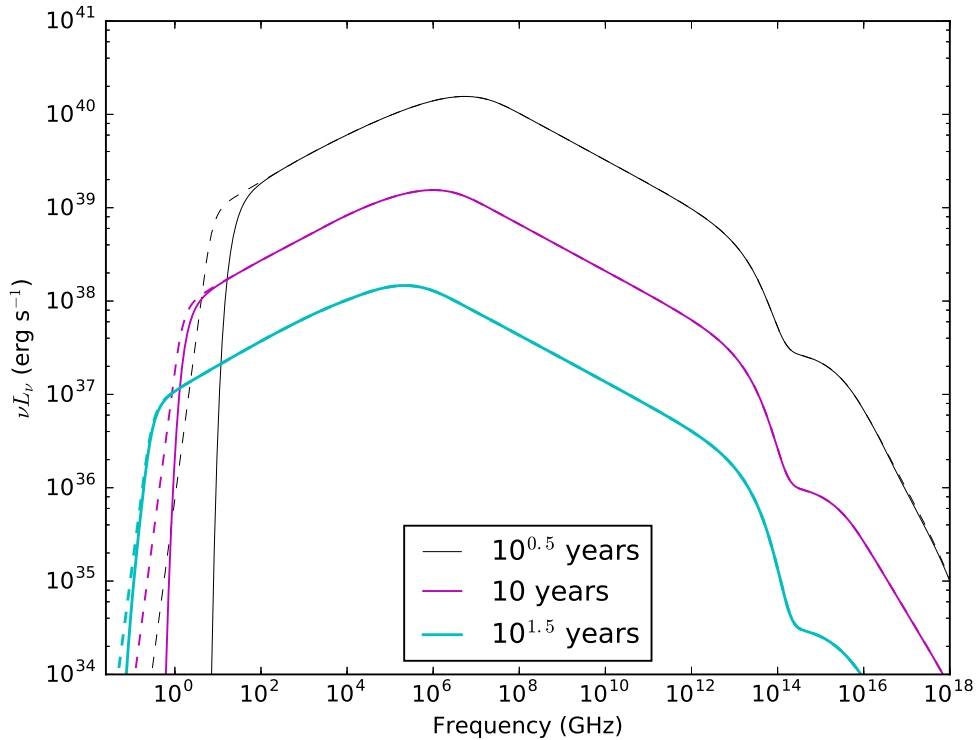


FIGURE 3.3: Broadband spectra from SN2011ke with $P = 1$ ms after $10^{0.5}$, 10, and $10^{1.5}$ years. The solid lines take absorption processes for radio waves into account while the dashed lines do not.

nucleosynthesis studies (e.g., Maeda et al. 2002). Although the effect is difficult to calculate consistently, the ionization state can be maintained x-ray radiation from the PWN. Although recent observations of PS1-14bj have found strong [O III] in the nebular spectra at $t \sim 0.5$ yr (Lunnan et al. 2016), which suggests a doubly-ionized state, the neutralization of the free electrons may proceed efficiently in the SN ejecta for $t \gtrsim 1$ yr. In this sense, the single-ionization assumption will overestimate free-free absorption, giving us a conservative estimate of the radio flux.

The pulsar spin-down, ejecta dynamics, and PWN dynamics are done as shown in Section 2.1.1, while other physical effects are calculated based on Section 2.1.2. After calculating spin-down, and ejecta and PWN dynamics, we solve a kinetic equation for electrons and positrons in the PWN, taking into account synchrotron and inverse Compton radiation, adiabatic cooling, and pair cascades.

The broadband spectra from SN2011ke with $P = 1$ ms at $10^{0.5}$, 10, and $10^{1.5}$ years are shown in Fig. 3.3. The spectrum has two components: the broken power-law spectrum up to $\nu \lesssim 10^{14}$ GHz from electron/positron synchrotron emission, and the higher frequency bump from inverse Compton scattering of thermal photons in the SN ejecta. The peak frequency of the νF_ν spectrum corresponds to the synchrotron frequency of electrons or positrons with $\gamma_{e^\pm, \text{peak}}$. As time increases, the spectrum becomes softer and flux becomes smaller due to the decline of energy injection and adiabatic energy loss of the PWN. The low frequency cutoff also moves to lower frequencies as time increases due to the decreasing radio/submillimetre opacity. Each SN spectrum is qualitatively similar, so only SN2011ke is shown.

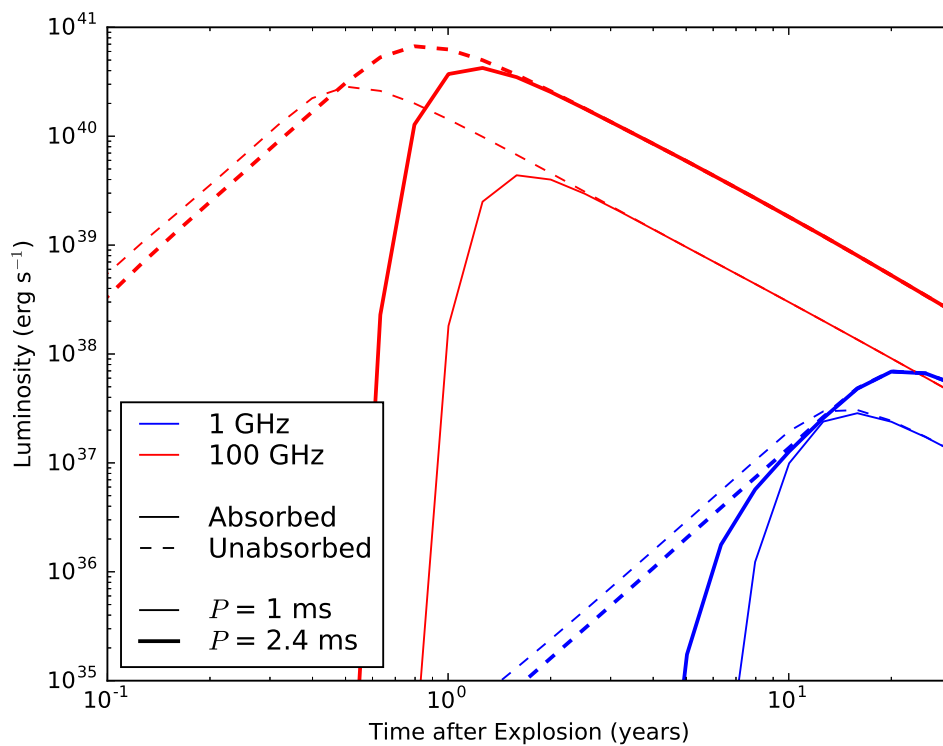


FIGURE 3.4: Intrinsic radio and submillimetre light curves from the pulsar wind nebula from SN2011ke at 1 GHz (blue) and 100 GHz (red). The thick and thin solid lines show the $P = 1$ ms and $P = P_{\text{max}} = 2.4$ ms cases, respectively, including the absorption processes in the PWNe and SN ejecta. The dashed lines are the unabsorbed light curves.

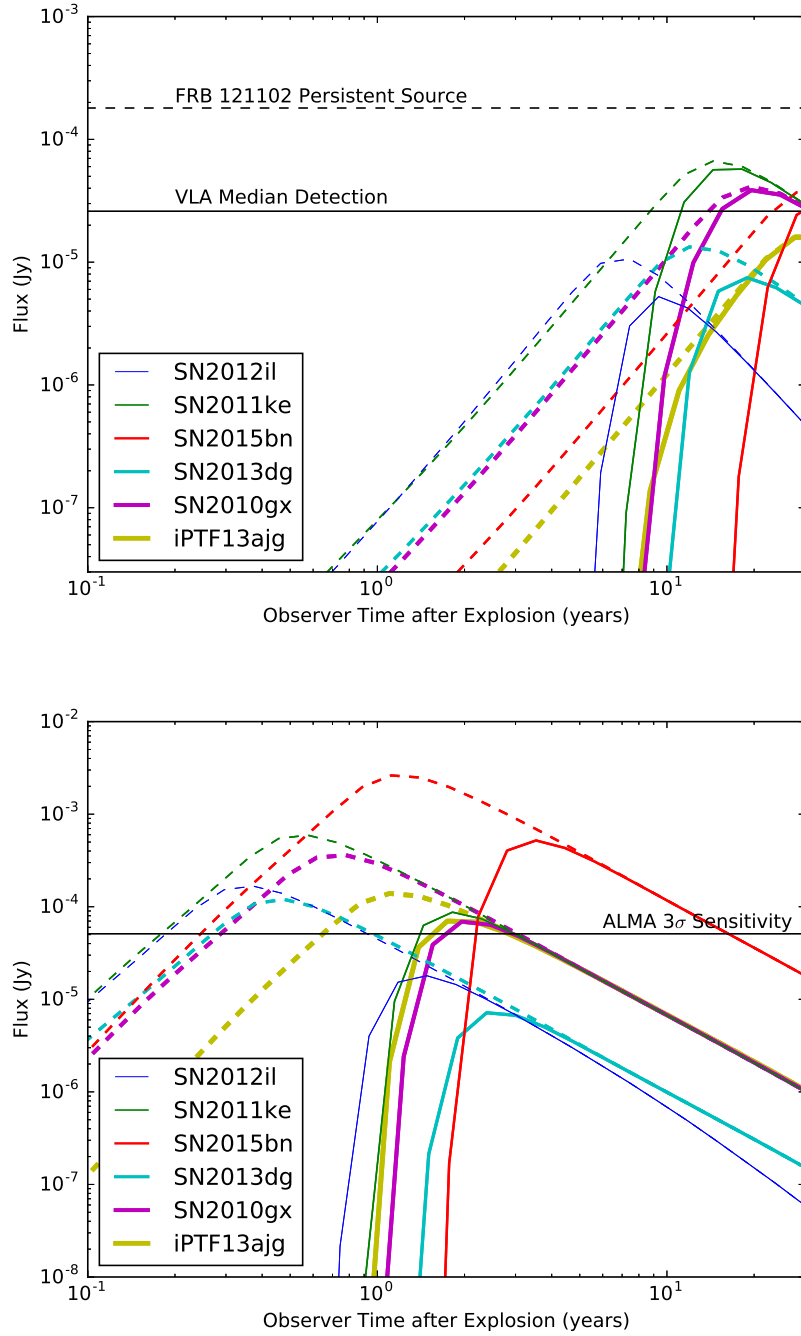


FIGURE 3.5: Predicted observable light curves from the pulsar wind nebula from each SN at 1 GHz (above) and 100 GHz (below) using the $P = 1$ ms parameters. The solid lines indicate the light curve with maximum absorption, while the dashed lines indicate the light curve with no absorption. The horizontal solid black lines indicate the median VLA detection of $26 \mu\text{Jy}$ (top) and the 3σ detection limit of $51 \mu\text{Jy}$ from ALMA (bottom) taken from (Chatterjee et al. 2017), although these fluxes were at 3 GHz and 230 GHz respectively. The dashed black line indicates the $180 \mu\text{Jy}$ flux of the persistent source of FRB 121102 at $D_L = 972$ Mpc.

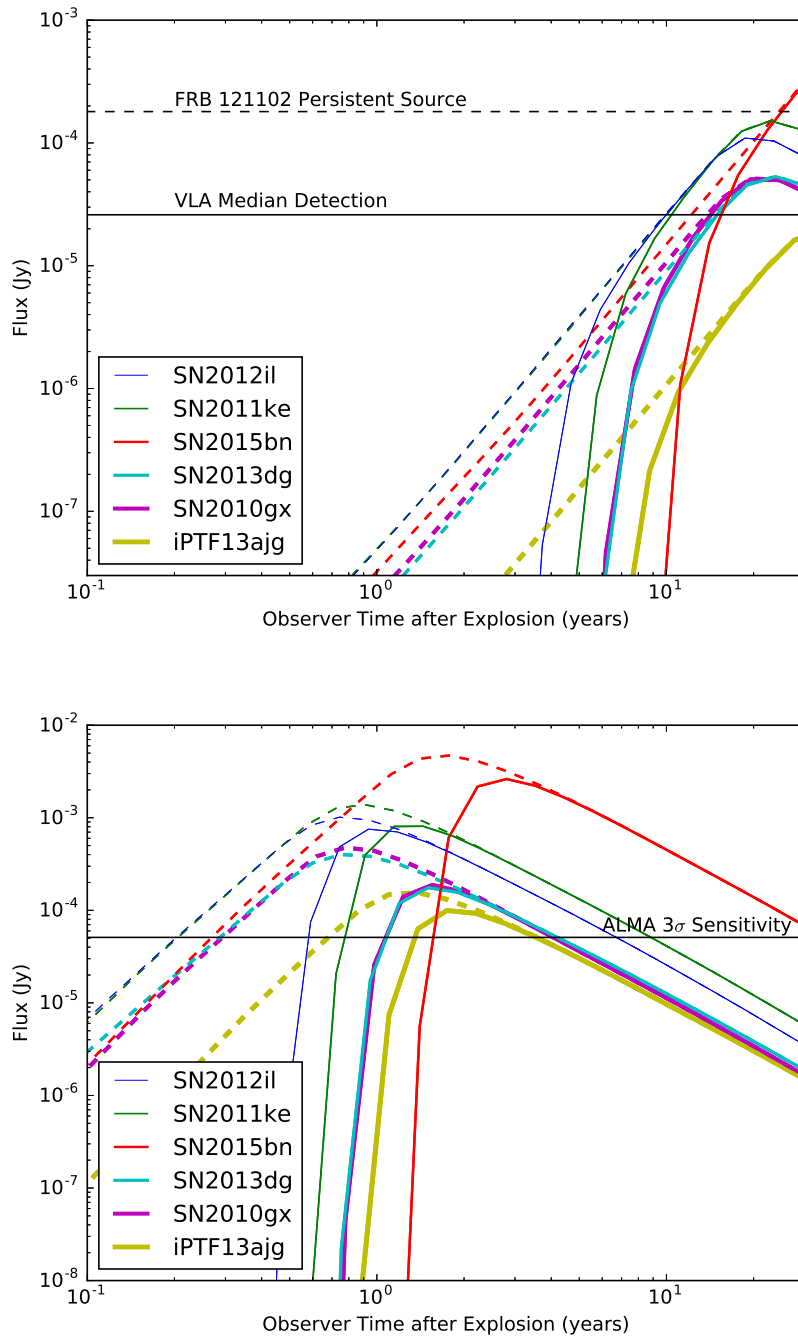


FIGURE 3.6: The same as Figure 3.5, but for the P_{\max} parameter sets from Table 3.2.

Hereafter, we focus on radio PWNe which radiate synchrotron emission from relativistic electrons and positrons accelerated by the nebulae. The cooling time of these high-energy particles is shorter than the dynamical time of the system. At later times, low-energy electrons and positrons do not have enough time to cool and they start to get accumulated in the PWN. These "relic" particles injected previously can also contribute to radio emission, which is calculated consistently in our model.

Fig. 3.4 shows intrinsic light curves at the 100 GHz (red) and 1 GHz (blue) band for SN2011ke. The solid lines include all the absorption processes while the dashed lines show the emission with no absorption in the SN ejecta (though the synchrotron-self absorption is included). The time of the unabsorbed light curve peak is determined from when the radio frequency becomes comparable to the synchrotron self-absorption frequency, while the time of the absorbed light curve peak is determined from free-free absorption. The absorption processes become irrelevant ~ 1 and ~ 10 yrs after the explosion for ~ 100 and ~ 1 GHz band, respectively, as the post-peak decline becomes essentially due to the spin-down of the pulsar.

In the same figure, we show the dependence of the radio PWN emission on the model parameters. The solid thick and thin lines correspond to the fastest ($P = 1$ ms) and slowest ($P = P_{\max} = 2.4$ ms) spinning models allowed for SN2011ke, respectively. As shown in Table 3.2, the P_{\max} set requires a smaller magnetic field, which lengthens the spin-down time, thus keeping the spin-down luminosity relatively high for a longer time. The slow-rotating case also requires a smaller ejecta mass, so the PWN and ejecta become transparent earlier. Consequently, the peak luminosity of the slow-rotating case is brighter than the fast-rotating case by a factor of $\lesssim 10$.

The light curves, as they would be observed from Earth, are shown in Figure 3.5 for both the 1 GHz and 100 GHz bands using the $P = 1$ ms parameter sets. The solid lines indicate the light curve with absorption, while the dashed lines indicate the light curve without absorption. For the 1 GHz band, VLA's 26 μJy median flux density from 68 background sources around the persistent source is shown, and for the 100 GHz band the 51 μJy 3σ detection limit from ALMA is shown.² The 1 GHz radio emission from some of the SLSNe reach the VLA sensitivity within 10-20 years and remain detectable until at least 30 years after the explosion. The signal may be detectable earlier if absorption is suppressed by effects such as mass-shedding via Rayleigh-Taylor instabilities. In the 100 GHz band with our nominal absorption, several SLSNe have a peak submillimetre flux just above the ALMA detection limit, while SN2015bn peaks at a full order of magnitude higher than the limit, although it peaks later than the other supernovae due to its higher ejecta mass. If emission at the peak time is observed due to the suppression of absorption, submillimetre signals could be detectable from 2-7 months until 1-2 years after the explosion, except for SN2015bn, which can be detected until around 15 years after the explosion. Motivated by a possible connection between pulsar-powered SNe and FRBs (Murase et al. 2016), we show the 180 μJy flux of the persistent source of FRB 121102 with a dashed black line in the VLA band (Chatterjee et al. 2017).

In Figure 3.6 we show radio and submillimetre light curves for each SN, using their P_{\max} parameter sets from Table 3.2. At 1 GHz, all SNe show a flux peak at later times than in the $P = 1$ ms case, with a timescale of ~ 20 -30 years that is not heavily affected by absorption. Even including absorption in the ejecta, only iPTFajg is not

²Note that these limits actually come from the 3 GHz and 230 GHz band of VLA and ALMA, respectively.

detectable by VLA. Around its peak, SN2015bn is well above the FRB 121102 persistent source flux and SN2011ke is only slightly below, at ~ 445 and $152 \mu\text{Jy}$ respectively. Unfortunately, our calculations only go to 10^9 s (~ 30 years), so we can't give a precise timescale for how long the emission will be detectable; however, it becomes detectable at ~ 10 -20 years depending on the supernova and in the case of SN2015bn, is still increasing at 30 years. Given this, 1 GHz emission from SN2015bn may be detectable for 70-100 years or longer after the explosion. At 100 GHz, all the sample SLSNe are detectable regardless of the absorption in the ejecta. Even with maximum absorption, the emission is detectable from 9 months to 2 years until 3-30 years after the explosion, and with no absorption, they become detectable from 2-7 months depending on the supernova. Regardless of absorption, SN2015bn has the highest peak flux, while iPTF13ajg has the lowest.

3.3.2 Radio Emission from Ejecta Forward Shocks

So far we have only considered non-thermal emission from PWNe associated with pulsar-driven SLSNe. But, we can also expect synchrotron emission from electrons accelerated by the SN forward shock. Here, we estimate this emission using a standard model (e.g., Chevalier 1998; Nakar & Piran 2011).

With the model parameters in Table 3.2, the central pulsar spins down on a timescale of a few months after the explosion. A large fraction of the initial rotation energy is converted into the kinetic energy of the SN ejecta, which is $E_K \sim 2 \times 10^{52}$ erg $(P/1 \text{ ms})^{-2}$ (See Equation 1.14). The typical ejecta velocity is $v_{ej} \approx (2E_K/M_{ej})^{1/2} \sim 0.06 \times c (P/1 \text{ ms})^{-1} (M_{ej}/5 M_\odot)^{-1/2}$. Here, the peak of the radio light curve with $\nu \gtrsim$ GHz corresponds to the deceleration time of the SN ejecta, $t_{dec} \sim 100 \text{ yr} (M_{ej}/5 M_\odot)^{1/3} (n/1 \text{ cm}^{-3})^{-1/3}$, where n is the number density of the interstellar medium (See Equation 1.7). Thus, the peak flux is estimated to be around $65 \mu\text{Jy} (\nu/1.5 \text{ GHz})^{-3/4}$ for a luminosity distance of $D_L = 300$ Mpc. In this estimate, we assume the power-law index of accelerated electrons is $p = 2.5$, the magnetic field amplification efficiency is $\epsilon_B = 0.1$, and the electron acceleration efficiency is $\epsilon_e = 0.1$; the flux decreases as ϵ_B and ϵ_e decrease. Before the peak, the flux is $\propto t^3$. The parameter set for this estimate is optimistic; for example, the kinetic energy would be smaller for a slower rotating pulsar. If we compare this emission from the forward shock to the emission from the PWN (Figures 3.5 and 3.6), we can conclude that the PWN emission likely dominates the forward shock emission until at least a few decades after the explosion.

It is worth noting that radio emission from electrons accelerated by the forward shock is more important in the presence of circumstellar material. Type-II SLSNe, which are believed to be interaction-powered, are expected to be particularly strong radio sources in 1-10 year time scales (Murase et al. 2014; Petropoulou et al. 2016).

3.4 Summary and Discussion

In this chapter, we investigated non-thermal radio and submillimetre emission from pulsar-driven SLSNe within a few decades of the explosion. We found that the PWNe emission will likely dominate the emission from the ejecta forward shock. Additionally, we have shown that follow-up observations of SLSNe with ALMA and VLA in ~ 1 and ~ 10 yr time scales are promising for relatively nearby events at $D_L \lesssim 1$ Gpc. Detections would support the pulsar-driven model for SLSNe and help solve the model parameter degeneracy, while non-detections would constrain the magnetar paradigm for the different classes of stripped-envelope SNe.

We assumed a simple one-dimensional for the evolution of the PWN and SN ejecta. External absorption is taken into account, assuming an oxygen-rich ejecta in a singly-ionized state. We should note that these predictions are subject to non-negligible uncertainties. Synchrotron self-absorption is relevant at lower frequencies, and this is taken into account in our calculations. Radio emission can also be absorbed by the free-free absorption and the Razin effect in the SN ejecta. These processes are sensitive to the ionization state of the ejecta, and the ionization is caused by x-ray emission from PWNe and a reverse shock induced by the SN ejecta. Our nominal parameters could overestimate the radio absorption and thus underestimate the observable flux. For example, the neutralization of the SN ejecta may proceed efficiently before the ionization state decouples from the ejecta evolution a few years after the explosion (e.g., Hamilton & Sarazin 1984). Also, the ejecta being pushed by the strongly magnetized pulsar wind could lead to a Rayleigh-Taylor instability, which would make ejecta more patchy and clumpy (e.g., Arons 2003; Blondin et al. 2001; Chen et al. 2016; Chevalier 2005; Chevalier & Fransson 1992; Suzuki & Maeda 2017), as opposed to the spherically symmetric ejecta in our model. Because of this, a portion of the PWN may be more easily observed due to reduced optical depths, even if the average ionization degree of the ejecta is high. If the wind bubble, which is surrounded by the PWN and mixed with shocked ejecta, is largely blown out, the nebula radius rapidly increases, and the resulting spectra become similar to those of Galactic PWNe.

Searching for radio and submillimetre non-thermal emission from SLSNe is also of interest to test the possible connection between young NSs and FRBs. Here, we have found that the radio emission from an embryonic SLSN remnant about a few decades old is broadly consistent with the flux of the persistent radio counterpart of FRB 121102. It is also interesting that young NS scenarios for pulsar-driven SNe and FRBs predicted the existence of bright quasi-steady radio emission before the host galaxy of FRB 121102 was detected (Murase et al. 2016).

The PWN emission does not always have to be powered by the spin-down energy of the pulsar. Beloborodov (2017) argued that the energy can instead be supplied via the magnetic activity of a magnetar associated with an FRB. Although this differs from our model, if the injected energy integrated over time is similar, both models can lead to similar nebular emission (although they can be distinguished by a long-term follow-up observation of the SLSNe with ALMA and VLA from ~ 1 to 10 yrs), keeping the consistency with the FRB-SLSN connection.

Chapter 4

Preliminary Results: Thermal PWN Re-emission from Dust Grains

We studied the direct detectability of PWN emission in Chapter 3, and now we introduce and discuss an indirect detection method: re-emission from dust grains. We use a steady-state model to study the growth of dust grains in the ejecta of a pulsar-powered supernova, and examine sublimation of smaller grains and re-emission from larger grains due to PWN emission. We consider dust compositions based on those expected for a variety of progenitors of Type Ic, Ib, and IIb supernovae, including SLSNe, and calculate the properties of C, MgSiO₃, and MgO grains in their ejecta. We find that dust is always optically thick from a few months after formation, and re-emits at a temperature between 1500-2000 K. For the cases of SN2015bn and SN2016ard, which we propose to study in Chapter 5, we find that the dust emission is not detectable at all, although this may be due to an unphysical part of our model. Apart from fixing this, the next steps include realistically calculating absorption, calculating emission using more parameter sets, and diagnosing our model to test its accuracy.

This project has been done in collaboration with Kazumi Kashiyama.

4.1 Introduction

In the expanding ejecta of a supernova, dust grains condense from cooling metal-rich gas. These newly formed grains are injected into the interstellar medium (ISM), where they cause interstellar extinction and diffuse infrared emission, catalyze H₂ formation, and serve as building blocks for planets and smaller rocky bodies.

In particular, the origin of dust has been fiercely debated since the discoveries of a huge amount of dust grains at redshifts higher than $z = 5$ (Gall et al. 2011). In the early universe, core-collapse SNe from massive stars are likely to be the dominant source of dust (Dwek et al. 2007). Infrared-submillimeter studies of SN1987A (Dwek & Arendt 2015; Indebetouw et al. 2014; Lakićević et al. 2012; Matsuura et al. 2011, 2015), SNR G54.1+0.3 (Temim et al. 2017), Cas A (Barlow et al. 2010; Sibthorpe et al. 2010), and the Crab Nebula (Gomez et al. 2012), as well as emission-line asymmetry studies of SN 1980K, SN1993, and Cas A (Bevan et al. 2017), have reported a subsolar mass of cool dust formed in the ejecta which have not yet been destroyed by the hot gas from the supernova reverse shock (Micelotta et al. 2016). What fraction of the dust can survive the shock depends on their sizes after formation (e.g., Nozawa et al. 2006, 2007), so understanding both the mass and size of dust produced in supernovae is important.

Dust formation in SN ejecta has mainly been studied with classical nucleation theory and its extension (Bianchi & Schneider 2007; Kozasa et al. 1989, 1991; Nozawa et al. 2010, 2003, 2011, 2008; Todini & Ferrara 2001). In this theory, dust condensation is described by the formation of stable seed nuclei and their growth, where the

	High Density	Low Density
Nozawa's T, c evolution	$M_{\text{ej}} = 50 M_{\odot}, f_C = 0.25$	$M_{\text{ej}} = 5 M_{\odot}, f_C = 2 \times 10^{-3}$
Our T, c evolution	$M_{\text{ej}} = 5 M_{\odot}, f_C = 0.15$	$M_{\text{ej}} = 5 M_{\odot}, f_C = 3 \times 10^{-4}$

TABLE 4.1: Initial parameters corresponding to high and low density cases discussed by Nozawa & Kozasa (2013), which have $c_1 = 10^8$ and 10^5 at the onset of dust formation, for the different. We get within a factor of 1.5.

formation rate is derived by assuming the nucleation current to be in a steady-state (Nozawa & Kozasa 2013). This theory has allowed us to predict the size distribution and mass of condensing grain species, and these results have nicely explained the mass of dust formed in SN1987A (Kozasa et al. 1991) and the formation and evolution processes of dust in Cas A (Nozawa et al. 2010).

We use this steady-state model, which is overviewed in Section 2.2, to study dust formation and emission in pulsar-driven supernovae. So far, this type of system has only been discussed in the context of gamma-ray bursts, and only the sublimation of previously formed dust was studied (Waxman & Draine 2000). The PWN emission delays the formation of dust due to the added energy injection and is capable of sublimating dust as it forms, leading to longer formation times and the possible non-production of dust at all. However, once dust has formed, the grains can absorb emission in the optical/UV band, greatly increasing their temperature compared to the case without a central pulsar. These hot dust grains will re-emit in the infrared, and this emission might be detectable with telescopes like Herschel, Spitzer, and the James Webb Space Telescope (JWST). This gives an indirect signal, to compliment the direct radio detection discussed in Chapter 3, by which we can detect newborn pulsars.

In Section 4.2, we test our code without a central pulsar and compare the results to Nozawa & Kozasa (2013). Then, in Section 4.3, we describe how we perform the study, which parameters we use, and the composition of the initial supernova gas. In Section 4.4, we describe the results that we have been able to acquire up to this point. Finally, in Section 4.5, we describe how to finish and further improve the study.

4.2 Reproducing Previous Results

We first tested our code for dust formation, based on the model from Section 2.2.1, by simulating carbon grain formation with the power law temperature evolution from Nozawa & Kozasa (2013), given in Equation 2.133, as well as their concentration evolution

$$\tilde{c}_1 = c_{1,o} \left(\frac{t}{t_o} \right)^{-3}. \quad (4.1)$$

This is not a useful evolution in the big picture, since there is no way to incorporate the pulsar, but is a useful diagnostic for our code.

We use the high and low density cases discussed by Nozawa & Kozasa (2013), which have $c_1 = 10^8$ and 10^5 at the onset of dust formation. Since we start our simulations well before dust begins to form and our parameters are magnetic field B , pulsar initial rotation period P , ejecta mass M_{ej} , and carbon mass fraction f_C (ie. the mass of carbon in the ejecta is $M_{\text{ej}}f_C$), we can not set the exact concentration at the onset of formation, so we use parameters that give us within a factor of 1.5 of $c_1 = 10^8$ and 10^5 at the onset of dust formation. The parameters are shown in Table 4.1. We take $s = 0.8$

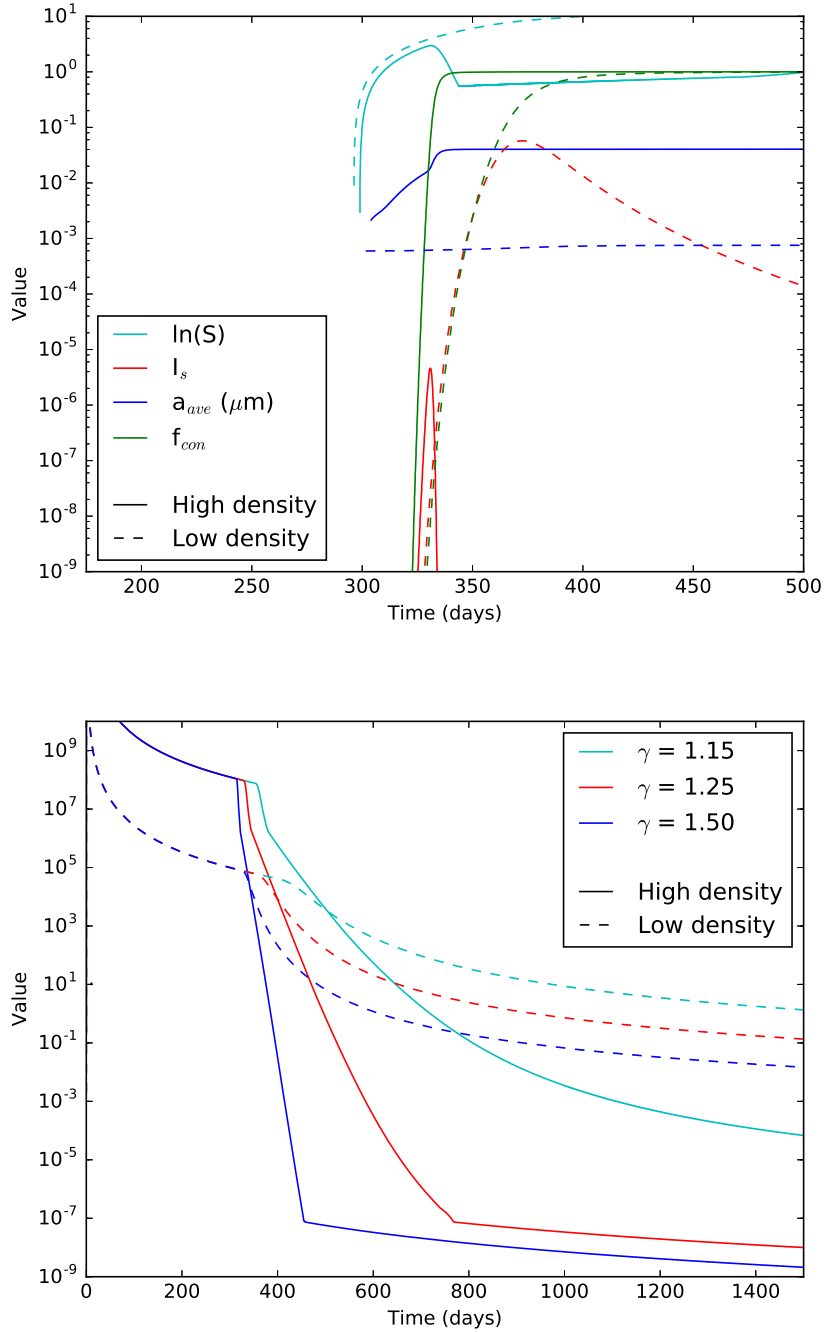


FIGURE 4.1: Summarizing our results with the temperature and concentration evolution from Nozawa & Kozasa (2013). Top: $\ln(S)$, I_s , f_{con} and a_{ave} for the high and low density cases with $t_o = 300$ days and $\gamma = 1.25$. Bottom: The gas concentrations for both cases using $\gamma = 1.15, 1.25,$ and 1.50 .

and $n_* = 100$, the sticking probability of a colliding gas molecule and the minimum number of molecules for a cluster to be considered a dust grain respectively, for all calculations; as long as n_* is large enough, the results do not qualitatively change - this is discussed in Appendix B of Nozawa & Kozasa (2013). When comparing to previous results, the pulsar is given a negligible field to effectively turn it off.

We plot $\ln(S)$, I_s , f_{con} and a_{ave} in the top panel of Figure 4.1 for the high and low density cases with $t_o = 300$ days and $\gamma = 1.25$, and we plot the gas concentrations for both cases using $\gamma = 1.15, 1.25$, and 1.50 in the bottom panel of Figure 4.1.

For the high density case, we see a sharp spike in I_s corresponding to the sudden nucleation of dust throughout the ejecta, which causes f_{con} to jump to ~ 1 within a timescale of $\lesssim 30$ days and the gas concentration to drop by about an order of magnitude within the same timescale. After this, the supersaturation ratio drops because of the drop in gas concentration, and this causes I_s to fall to ~ 0 . As time goes on, the nucleated grains grow in size by accreting free key molecules, causing the concentration to drop further, but more slowly than during nucleation. There is also nucleation of new grains as the temperature drops further, but the growth rate is small and concentration evolution is dominated by growth of previously nucleated grains. Once the concentration drops low enough, the grain growth rate and grain nucleation rate both drop to ~ 0 and concentration evolution is simply due to the expansion of ejecta; this phase is visible within 1500 days for $\gamma = 1.25$, and 1.50 , but not for $\gamma = 1.15$.

For the low density case, the nucleation of dust grain is not as sudden, and happens over a timescale of ~ 100 days. I_s reaches its peak about 75 days after t_o , but doesn't drop off very much afterwards. The concentration doesn't drop off nearly as much in this case as the high density case either, leading to this case having much higher gas concentration after the high density's main drop-off. The reason the concentration is high, even though $f_{\text{con}} \sim 1$, is because the dust grains are two orders of magnitude smaller in size than in the high density case.

We then test our own temperature and concentration/volume evolution, which is given by accounting for energy entering the ejecta and the dynamics of the pulsar wind nebula (PWNe) pushing the ejecta (See Section 2.1.1). We again plot $\ln(S)$, I_s , f_{con} and a_{ave} for the high and low density cases in the top panel of Figure 4.2, but since γ is no longer a parameter the bottom panel only shows the high and low density cases. The results are very similar to the $\gamma = 1.50$ case, with a steep drop and quick leveling in gas concentration for the high density case and a slow decline for the low density case. We see $\ln(S)$ fall and then rise again at high density; this second rise corresponds to the point when grain growth ceases, and concentration evolution becomes only due to the expansion of ejecta.

4.3 Study Overview

Once we verified the code to work and give similar results to Nozawa & Kozasa (2013), we tested the formation of dust for two initial dust compositions (mass fractions are given in Table 4.2), which we call the B and S compositions. These compositions are based off of recent radiative transfer simulations of various types of supernovae with various types of progenitors, which account for nuclear fusion during the explosion (Dessart et al. 2011, 2012, 2015, 2017; Vlasov et al. 2016). The B composition is similar to that of a small (ZAMS mass of 15-25 M_\odot) Wolf-Rayet star in a binary with roughly solar metallicity; one would expect about 3-5 M_\odot of ejecta in this case. The S composition is also fairly similar to a low metallicity Wolf-Rayet star without a binary companion with a ZAMS mass of around 25 M_\odot ; the ejecta mass in this case would be

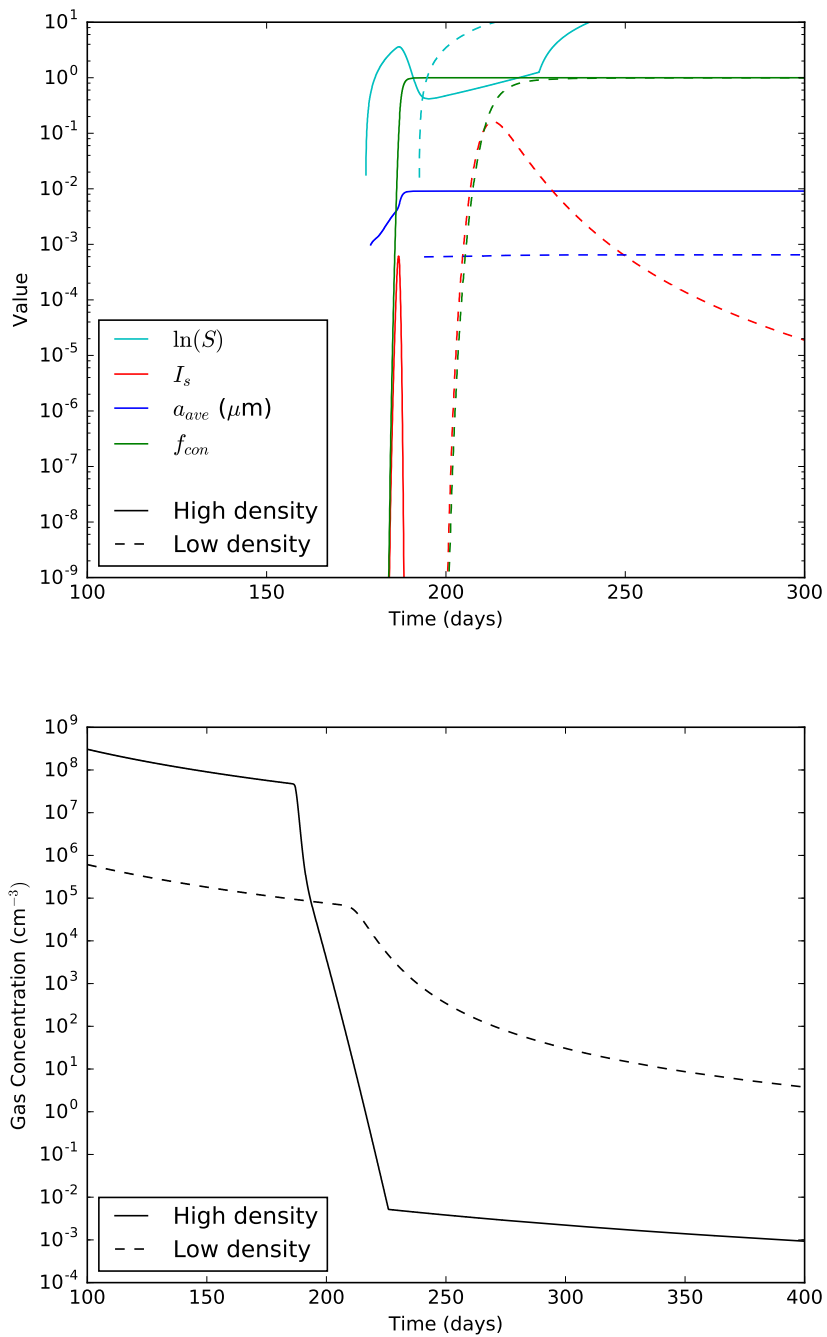


FIGURE 4.2: Summarizing our results with our temperature and concentration evolution. Top: $\ln(S)$, I_s , f_{con} and a_{ave} for the high and low density cases. Bottom: The gas concentrations for both cases.

Composition	f_C	f_O	f_{Mg}	f_{Si}
B	0.1	0.3	0.03	0.03
S	0.3	0.6	0.05	0

TABLE 4.2: Initial mass fractions of the different gaseous elements in the ejecta.

Grain Type	$C_{(s)}$	$MgSiO_{3(s)}$	$MgO_{(s)}$
Key Species	$C_{(g)}$	$Mg_{(g)}$	$Mg_{(g)}$
$A/10^4$ (K)	8.64726	25.0129	11.9237
B	19.0422	72.0015	33.1593
a_o (Å)	1.281	2.319	1.646
σ_{ten} (erg cm ⁻²)	1400	400	1100

TABLE 4.3: The properties of the dust grains considered in this study. The subscript (s) and (g) represent solids and gasses respectively. Since Mg and Si have the same concentration in the B composition, either one can be used as the key species. Values are taken from Nozawa et al. (2003).

$\sim 15 M_{\odot}$. The S composition is similar to that of a large solar metallicity Wolf-Rayet star with ZAMS mass of around $60 M_{\odot}$ evolved without a binary companion; one would expect about 5-7 M_{\odot} of ejecta in this case.

The biggest differences between the two are the lack of Si in the S composition and the lower overall numbers in the B composition. While the Si mass fraction is not zero in real SNe, the simulations give a mass fraction of about 10 times lower than that of Mg for the S composition progenitor; this is small enough where we expect MgO grains to be formed in much greater quantity than $MgSiO_3$ or Mg_2SiO_4 , so we neglect Si completely for the S composition. The B composition has lower numbers because a large fraction of the gas is still He, which doesn't form dust and is thus neglected in this study. The large fraction of He means that observed SNe with the B composition would be either Type Ib or IIb, depending on if any H gas still remained as well, while observed SNe with the S composition would be seen as Type Ic.

We examine two different types of dust growth for each composition. For the B composition we examine the formation of C and $MgSiO_3$ grains, which we expect to be formed preferentially over Mg_2SiO_4 by about a factor of 3 (Nozawa et al. 2010). For the S composition, since there is not enough Si to form large quantities of $MgSiO_3$ or Mg_2SiO_4 , we examine growth of C and MgO grains. The physical properties of each dust grain used in the calculation are listed in Table 4.3. We assume for the B composition that the concentrations of Mg and Si gas remain equal, and we assume that the number of oxygen atoms remains fixed, since the ejecta is oxygen dominated and grain formation will not significantly affect the concentration.

We ignore the formation of CO molecules, even though in oxygen-rich ejecta (which both compositions have) it is expected that carbon dust will not form due to the formation of CO molecules. Since our model is a one-zone model, including CO formation would mean we never form any carbon dust. In more complicated models, supernovae have both an oxygen-rich shell where silicate and Mg-molecule-based dust formation is dominant and a carbon-rich shell where carbon dust formation is dominant (e.g., Nozawa et al. 2010, 2008) - our model gives us the best possible case for carbon dust formation. For most supernovae, we would only expect carbon dust formation in the carbon-dominant shell, which surrounds the oxygen-rich shell and

ID	Composition	$M_{\text{ej}} M_{\odot}$	f_L
B5-1	B	5	1
B5-0p75	B	5	0.75
B15-1	B	15	1
S5-1	S	5	1

TABLE 4.4: The four sets of ejecta and PWNe parameters we study. f_L is a multiplying factor for the PWNe flux.

usually contains $\sim 50\%$ of the carbon atoms, but in SLSNe, turbulent mixing mixes the gas and homogenizes the ejecta, meaning that carbon dust will not form.

We perform a parameter study for the initial pulsar rotation period P and the initial magnetic field B . The power law index for the PWNe emission is -0.5 , which agrees with the one found in Chapter 3 between 10^8 and 10^{14} GHz. However, the overall flux is multiplied by the factor f_L , which is analogous to changing the power law spectrum, since only the total luminosity in the optical band is important for dust temperature and sublimation (Section 2.2.2). We investigate four sets of ejecta and PWNe parameters, shown in Table 4.4; they will give us qualitative information on the effect of changing ejecta mass, the PWNe spectrum, and the composition as well as being case studies for typical binary Wolf-Rayet progenitors (B5-1) and low metallicity single progenitors (B15-1), while S5-1 will be a case study for large solar metallicity single progenitors.

4.4 Preliminary Results

Figure 4.3 show the pulsar conditions where dust can be formed for each parameter set. Carbon is always formed in a larger parameter range than MgSiO_3 and MgO due to its higher critical temperature. All four models have a region where no dust is formed around $P = 1$ ms and B_{13} between 0.1 and 1; the lack of formation is due to continuous sublimation of grains as they form. This region is surrounded by a parameter space where only carbon dust can form, but not MgSiO_3 or MgO , with the size of this region depending largely on the model. The maximum period for this region increases almost as a power law with increasing field until a fairly sharp cutoff at $B_{13} \sim 10$. At large spin periods and either high or low magnetic fields, both types of dust can be formed. This is because with low fields, the spin-down is slow enough that the luminosity will never be high enough to sublimate the dust, and at high fields, the star spins down so quickly that most of the energy is released before dust ever starts to form, making the late PWN emission less luminous.

When decreasing f_L , both types of dust can form at lower periods due to the lower PWN luminosity not being capable of sublimating the grains as they form. Increasing M_{ej} has the same effect because the PWN emission needs to sublimate more dust grains due to the larger gas concentration, and thus can't always sublimate out to R_{ej} . Changing the composition to S makes carbon grains easier to produce due to their increased concentration, but MgO grains are thermodynamically harder to produce than MgSiO_3 , so the parameter region where they can not be produced is quite large, even extending out to $P \sim 50$ ms at $B_{13} = 10$.

We next examine the effects of changing P and B on temperature and carbon grain optical depth evolution in the B5-1 composition. We select five points: $(P \text{ (ms)}, B_{13}) = (7, 1.0)$, the fiducial point at the edge of the region where MgSiO_3 grains can not be formed; $(7, 0.3)$, which does form MgSiO_3 grains and shows the effect of slightly

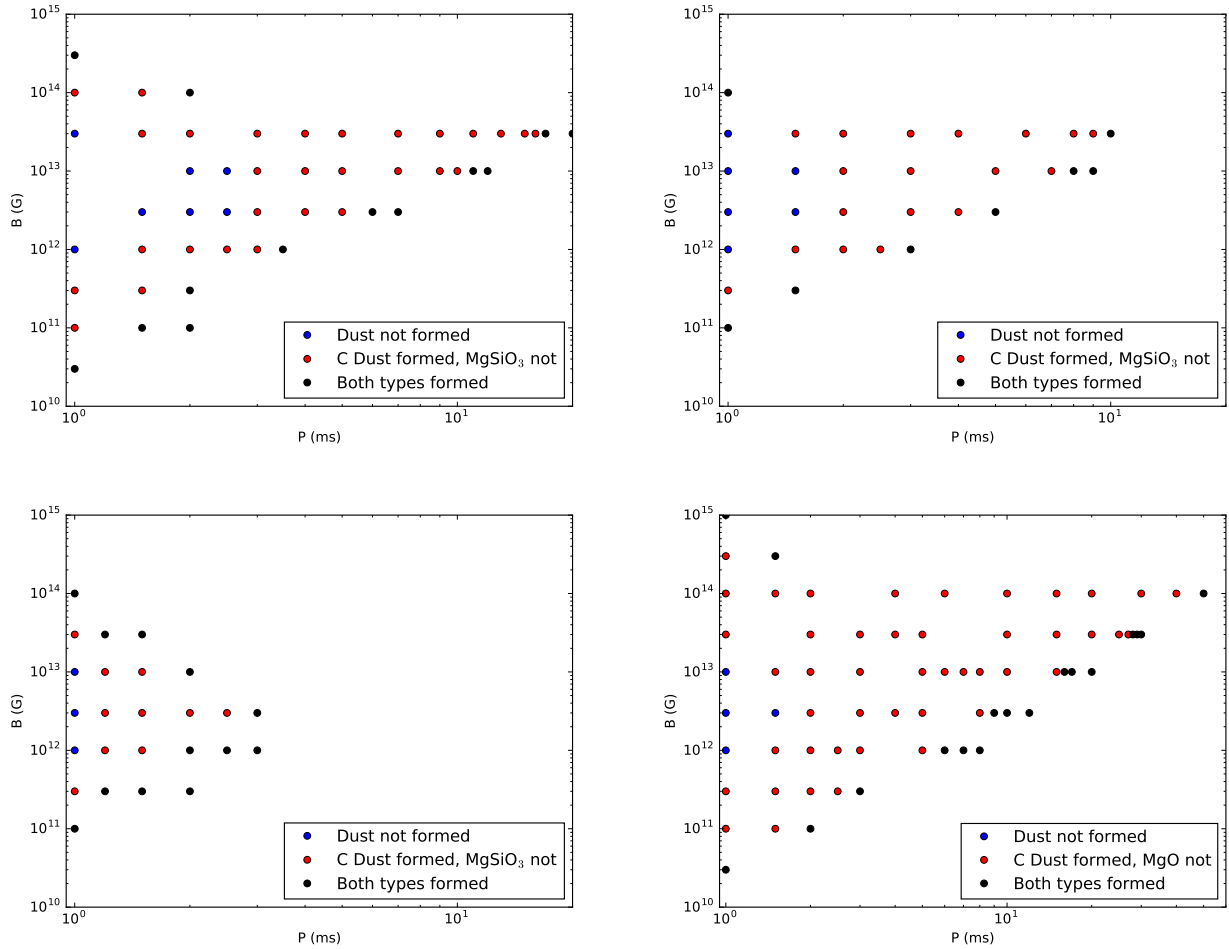


FIGURE 4.3: The parameter regions where each type of dust is formed for the B5-1 (top left), B5-0p75 (top right), B15-1 (bottom left), and S5-1 (bottom right) parameter sets. The blue dots, and the area to their left, indicate a region where no dust is formed; the red dots indicate the region where carbon dust is formed but MgSiO_3 (for the B sets) or MgO (for S5-1) is not, and the black dots, and the area to their right, indicate the region where both dust types are formed. Note that the horizontal scale for the S5-1 diagram is different from the other three.

changing the magnetic field; (11, 1.0), which also forms MgSiO_3 grains and shows the effect of slightly increasing the spin period; (3, 1.0), which is the lowest period with $B_{13} = 1$ where carbon dust grains will form; and (2.5, 1.0), where no dust forms, even though the parameter set is close to (3, 1.0). In the top panel of Figure 4.4, the optical depth for carbon grains is shown. The optical depth is $\gg 1$ once the first nucleation spike is over, although in the (3, 1.0) case the spike lasts for ~ 30 days, meaning that the dust emission will resemble an isothermal blackbody at the critical radius. The first to form carbon dust, at ~ 200 days, are the (7, 0.3) and (11, 1.0) parameter sets, followed by (7, 1.0) at ~ 300 days and (3, 1.0) at ~ 500 days; the closer the parameter sets are to the region where dust doesn't form, the longer it takes to form dust. The gas temperature evolution is also not a reliable measure of long-term dust formation, as the (3, 1.0) and (2.5, 1.0) sets have almost the same gas temperature throughout their evolution, but (2.5, 1.0) never forms dust; this confirms that the controlling factor for long-term dust formation is sublimation via PWN emission.

We also examine the effect of changing the composition on temperature and carbon grain optical depth evolution in Figure 4.5. We chose points at roughly the same position in the phase diagram, where only carbon forms, but MgSiO_3 or MgO would form with a small increase in period or decrease in magnetic field; these points are $(P \text{ (ms)}, B_{13}) = (7, 1.0)$ for B5-1, (1.5, 0.1) for B15-1, (4, 0.3) for B5-0p75, and (15, 1.0) for S5-1. We see that B15-1 forms dust much later and has a slower temperature decrease than the others, at ~ 1000 days compared to the 200-300 days of the other compositions; this is because the ejecta velocity is slower when there is a larger ejecta mass due to the explosion energy remaining fixed, so the evolution of most parameters of the supernova becomes slower overall. We see that all compositions are extremely optically thick after dust nucleation finishes, just like in Figure 4.4, although dust formation takes ~ 50 days in the B15-1 model. We also see a slight difference of the critical temperature between the different models, with B15-1 being about 100 K higher than B5-1 or B5-0p75.

We next investigate possible dust formation in SN2015bn and SN2016ard, the two SLSNe we propose to investigate with ALMA in Chapter 5. We use $f_L = 1$ and the S composition, since they were both observed as Type Ic supernovae. We calculate $P = 1.0$ ms and P_{max} parameter sets as in Chapter 3. For $P = 1.0$ ms, the $(B_{13}, M_{\text{ej}} (M_{\odot}))$ parameter sets are (2.1, 17) for SN2015bn and (6.0, 12) for SN2016ard, while the $(P_{\text{max}} \text{ (ms)}, B_{13}, M_{\text{ej}} (M_{\odot}))$ parameter sets are (1.4, 1.0, 5) for SN2015bn and (2.2, 1.7, 1.5) for SN2016ard. We find that no dust is formed for the P_{max} cases and only carbon dust is formed in the $P = 1.0$ ms cases, and we show the carbon optical depth and temperature evolution in Figure 4.6 and radius evolution in Figure 4.7 for the $P = 1.0$ ms cases. We find that both supernovae produce extremely optically thick carbon dust and start to form dust at $\sim 200 - 300$ days, with the more massive SN2015bn ejecta forming dust later. We also find that the critical radius decreases sharply at the beginning of dust formation due to the large increase in dust grain radius a , which affects the dust emissivity; we think this effect is largely artificial, and discuss it more in Section 4.5. After this decrease, R_c increases slowly over time.

We calculate the spectrum of the dust emission with dust emissivity $Q(a)$ calculated using $\beta = 1$ and 2, the minimal and maximal values, for the two SLSNe and compare them to the intrinsic PWN spectrum in Figure 4.8. For both SLSNe, the PWN produces much stronger emission than the dust in both SNe, and the dust is undetectable until at least 30 years after the explosion. However, the reverse shock, which begins at the Sedov phase of the SN (~ 100 years after explosion), will destroy any dust in the ejecta as it passes through; given these results, it is unlikely that we can detect the dust emission at all before it is destroyed by the reverse shock.

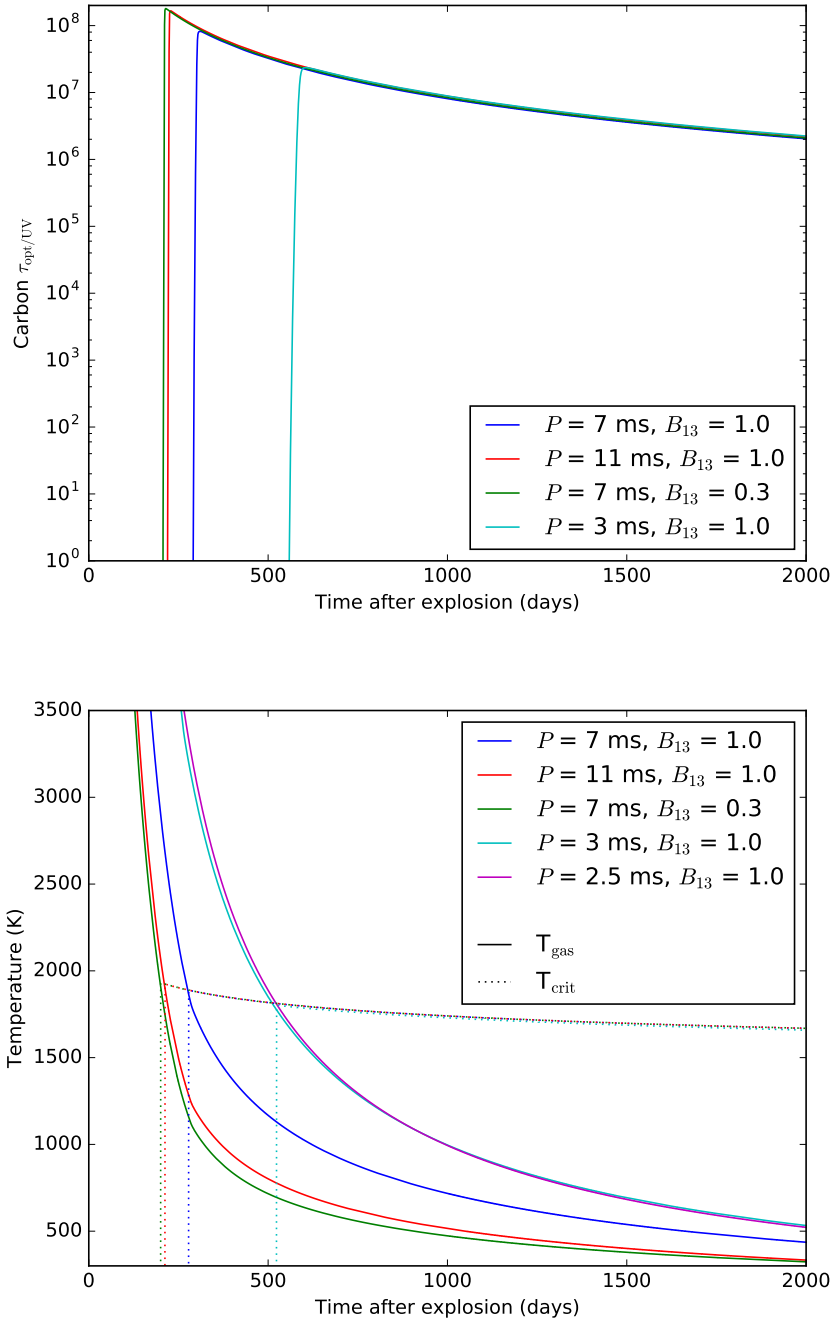


FIGURE 4.4: The carbon grain optical depth (top) and temperature (bottom) evolution for several (P, B_{13}) parameter sets using the B5-1 composition. The solid line in the bottom panel shows the gas temperature and the dotted line shows the dust critical temperature. Since the grains are very optically thick after the first nucleation spike is over, the emission will look like a single blackbody shell at radius R_c emitting at temperature T_c . The dotted vertical lines in the bottom panel shows exactly when dust first starts to form.

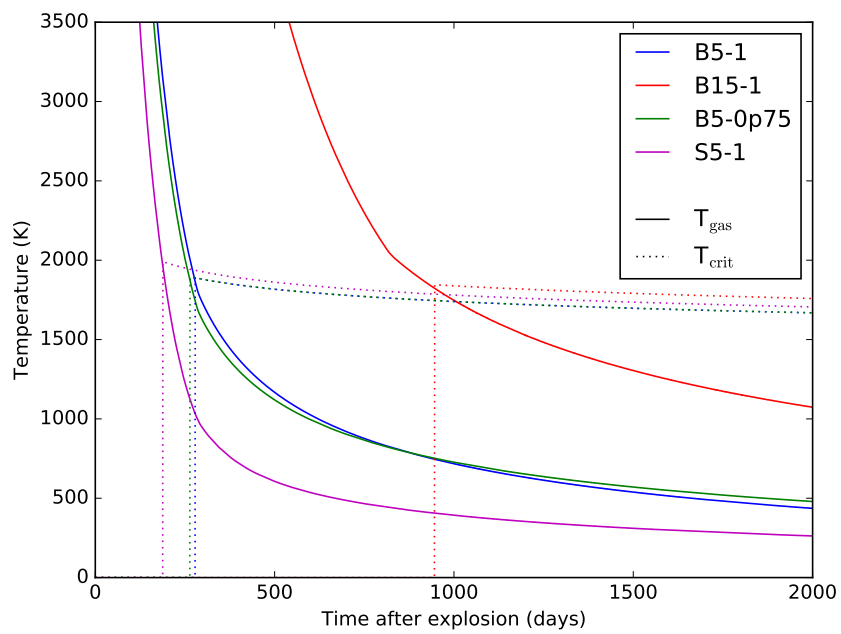
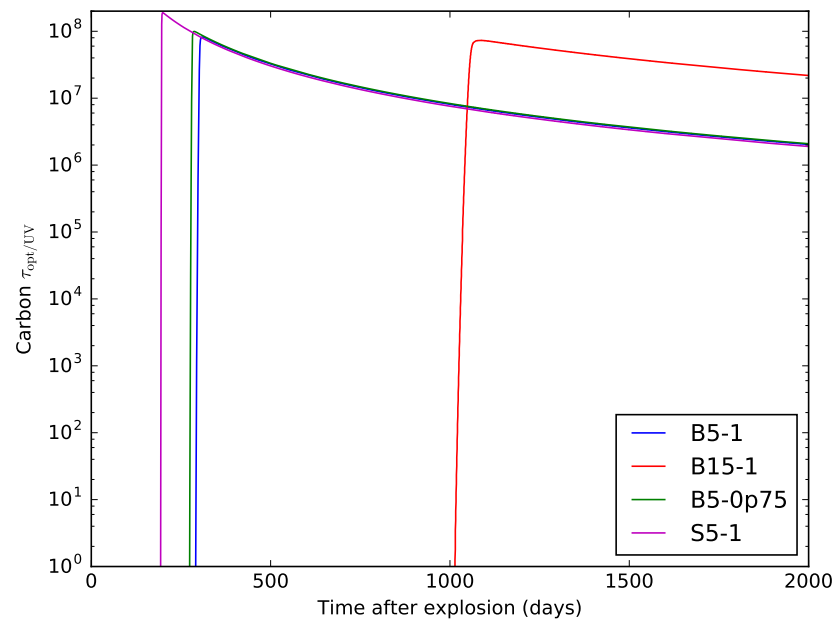


FIGURE 4.5: The same as Figure 4.4, except comparing different compositions.

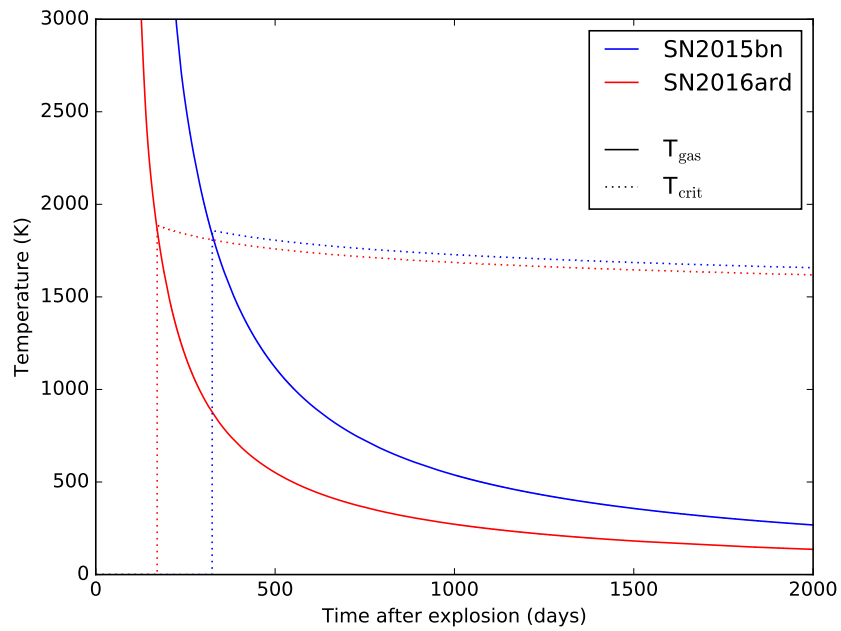
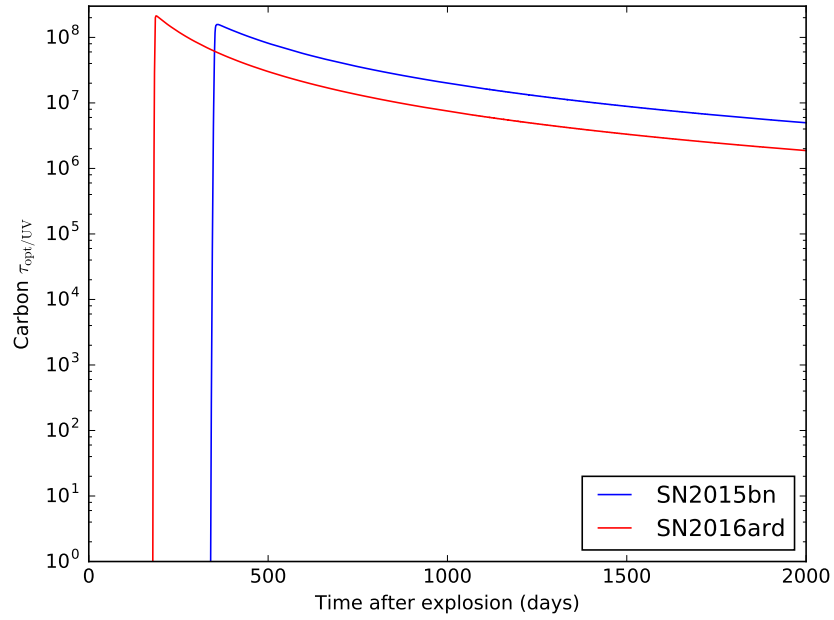


FIGURE 4.6: The same as Figure 4.4, except for the two SLSNe investigated in Chapter 5.

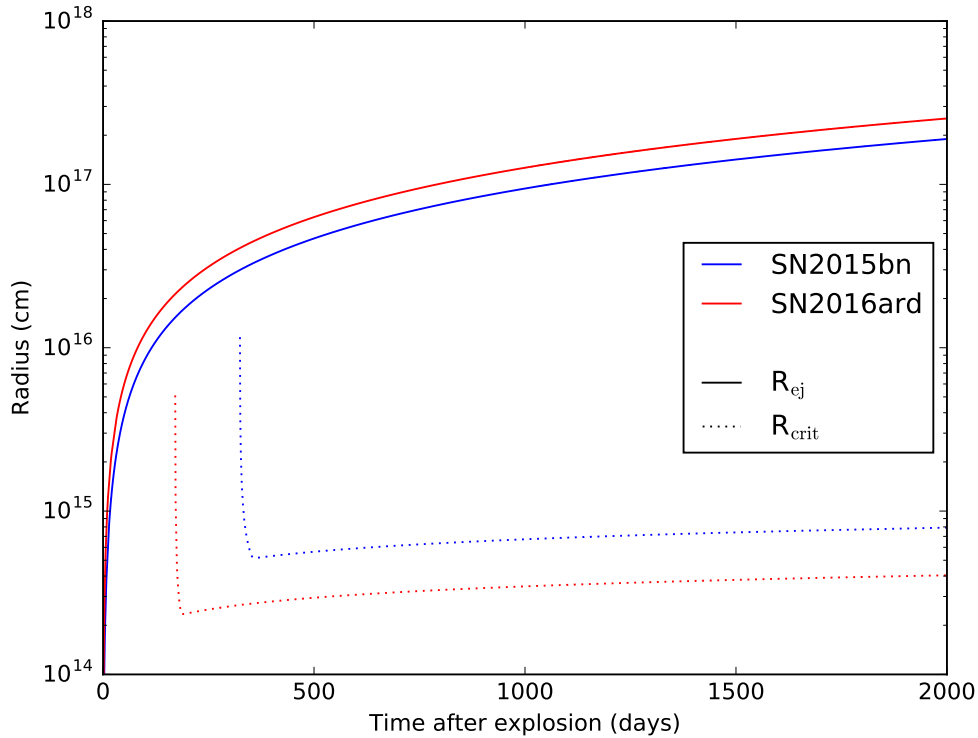


FIGURE 4.7: The ejecta radius and critical sublimation radius of the two SLSNe investigated in Chapter 5.

4.5 What Next?

In looking at the dust emission in Figure 4.8, one might wonder why if all the energy in the 1 – 7.5 eV band is being absorbed (not shown in the Figure, but included in the model), why is the dust emission not very luminous; these results seem to not conserve energy. There are a few possible reasons for this; the first is that the way our model treats formation as one-zone and sublimation/emission as two-zone artificially inflates the dust emissivity $Q(a)$ of unformed dust. Since dust grains are very small when they start to form, $\langle Q \rangle_T$ is small and the dust is likely to be sublimated by the PWN emission, while the grains are much more difficult to sublimate once the dust is fully grown. Since our model assumes that dust everywhere has the same a value, this results in a sharp, artificial decrease in R_c soon after dust begins to form; this is visible in Figure 4.7. If this decrease was not present, R_c would be larger by about a factor of 20, and the dust emission would be more luminous by about a factor of 400, making it detectable after less than a decade. Another possible reason for energy loss is the energy used to sublimate dust grains at $R < R_c$. As dust formation is favoured via entropy, the photodissociation of the inner dust grains must continuously keep energy from leaving the system as thermal radiation from the outer grains. A final possibility is that the calculated R_c , even after the $Q(a)$ correction, would be less than R_{PWN} , which is unphysical; however, increasing R_c to $\geq R_{\text{PWN}}$ would also decrease the emission temperature, meaning the total power radiated would be the same, but the emission would be at lower wavelength. The first priority for continuing this study is making sure all the energy is accounted for and that our model does not have unphysical features.

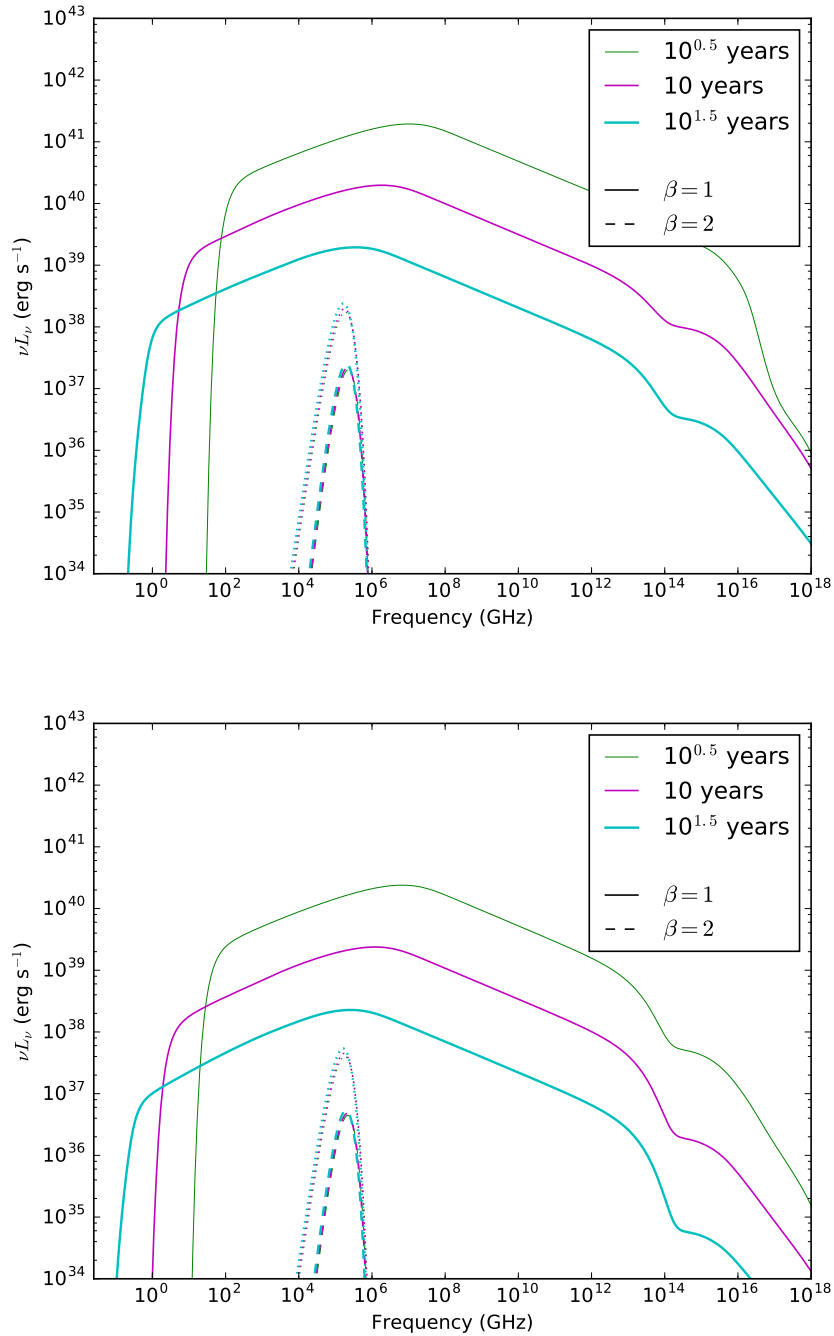


FIGURE 4.8: Broadband PWN spectra for SN2015bn (top) and SN2016ard (bottom) compared to their dust emission with dust emissivity $Q(a)$ calculated using $\beta = 1$ (dashed) and $\beta = 2$ (dotted), the minimal and maximal values. The PWN produces much stronger emission than the dust in both SNe, and the dust is undetectable until at least 30 years after the explosion.

Once this is accounted for, there are plenty of other things that need to be done. All the plots shown are for carbon dust only, which we do not even expect to form in SLSNe because of the formation of CO molecules, and so similar plots need to be made for MgSiO_3 and MgO using all the compositions. Dust emission should be calculated for a number of different compositions and parameter sets and compared to PWNe spectra to ascertain the possibility of detecting the dust emission. The absorption of UV and optical photons should be accounted for more realistically instead of assuming that all radiation is absorbed in a particular band, which will involve calculating a size distribution for the dust grains, which may be dependant on the position in the SN ejecta. Finally, we want to calculate Λ from Equation 2.131, which indicates if the steady state model agrees with the more accurate non-steady state model, to determine if our application of this model leads to accurate results.

Chapter 5

Proposal: ALMA Observations of SN2015bn and SN2016ard

This chapter is based on our Cycle 5 proposal for the Atacama Large Millimeter/submillimetre Array (ALMA), which was accepted with B priority. These observations have the potential to provide hints on the origin of super-luminous supernovae (SLSNe) that may be applicable to other interesting high-energy phenomena, such as Fast Radio Bursts (FRBs). However, these observations may not unambiguously confirm the magnetar model, even if synchrotron radiation is detected, and it is not obvious which system parameters would be constrained from the ALMA in a model-independent way. Nevertheless, these observations are a critical test for the pulsar-driven model, as this is the first attempt at detecting early submm PWN emission, and a successful detection would be strong evidence for the model as well as detection of the youngest known pulsar to date; studying this system would give a lot of insight into early pulsar evolution and its impact on the surrounding SN. These observations should take place this winter.

The team for this proposal consists of Kohta Murase, Kazumi Kashiyama, Hiroshi Nagai, Casey Law, Geoffrey Bower, Raffaella Margutti, Ryan Chornock, Deanna Coppejans, Derek Fox, Peter Mészáros, and myself.

5.1 Overview

Our aim is to measure the continuum spectra of SLSNe 1-3 years after their explosions. In particular, we will observe SN2015bn and SN2016ard in frequency bands 3 (84-116 GHz) and 6 (211-275 GHz). This study will provide a critical test for the rapidly-rotating pulsar model for SLSNe and possibly reveal their connections to FRBs.

The most popular theoretical model to explain the quasi-thermal optical emission of Type-I SLSNe is the rapidly-rotating pulsar model, in which the optical emission is powered by a millisecond pulsar with a strong magnetic field of $\sim 10^{13} - 10^{15}$ G. The predicted smoking gun for this model is non-thermal synchrotron emission in the radio/submillimetre band (See Chapter 3). A successful detection with ALMA would be the first evidence for a pulsar-like central engine and would also be a clue to the progenitors of FRBs, while non-detections would impose severe constraints on the pulsar-driven model for SLSNe.

The detectability of PWN emission in the GHz band is limited by strong free-free absorption in the supernova ejecta during the first \sim decade after the explosion. However, ALMA observations at around 100 GHz overcome the absorption problem, which provides a unique opportunity to detect the PWN emission. The emission is extragalactic and non-thermal, so observations with a great sensitivity of $\sim 100 \mu\text{Jy}$

are necessary. The emission is predicted to be quasi-steady during a timescale of a few months, and the best SLSN targets have an age of ~ 1 -3 years. Among recent SN, only SN2015bn and SN2016ard are predicted to be observable. Since SN2015bn is one of the brightest SLSNe on record, Cycle 5 observations are essential for accomplishing our goal.

5.2 Scientific Justification

Recent optical transient surveys such as Catalina Real-Time Transient Survey (CRTS), the Palomar Transient Factory (PTF), and Gaia have revealed the diversity of SNe, and SLSNe, which can be more than 100 times more luminous than normal SNe, form an interesting subclass of SNe (Gal-Yam 2012). Type-I SLSNe, which do not show hydrogen lines in their spectra, are particularly interesting and widely modeled using the pulsar-powered model, in which the rotational energy of a newborn, millisecond-rotating pulsar with a magnetic field of $\sim 10^{13} - 10^{15}$ G is the dominant source of energy for the quasi-thermal optical emission in the early phase while the ejecta is still dense enough to absorb and thermalize the photons emitted by the pulsar spin-down (Kashiyama et al. 2016; Nicholl et al. 2013). Type-Ibc SNe and long GRBs are also thought to be powered by pulsars with even stronger fields of $\sim 10^{14} - 10^{16}$ G (Thompson et al. 2004), and naturally, a connection between these events and SLSNe has been proposed (Greiner et al. 2015; Metzger et al. 2015). The newborn pulsar idea is particularly interesting because it predicts a grand-unified picture where SLSNe, stripped-envelope SNe, and GRBs all have the same object as a central engine.

To test this model and reveal the possible link between SNe and GRBs, it is imperative to detect smoking gun signals of newborn neutron stars. However, this is difficult to achieve using only optical observations. In this model, the light curves of the SNe can be modelled by adjusting the pulsar magnetic field B and initial rotation period P , as well as the ejecta mass M_{ej} , but there is a large degeneracy in the parameters (Kashiyama et al. 2016). Non-thermal signals serve as a new probe of central engines hidden within the ejecta, which solve the above degeneracy problem. It is known that galactic PWNe such as the Crab nebula are extremely efficient accelerators of electrons and positrons, injecting as much as 99% of their energy into these particles (Gaensler & Slane 2006; Tanaka & Takahara 2010). Broadband non-thermal emission from PWNe has been observed from many Galactic pulsars, which suggests most of the magnetic energy is used for particle acceleration. Therefore, non-thermal synchrotron emission from nascent PWNe should be a more direct signal, and can be used as a smoking gun for the pulsar-driven supernova model. In this model, optical radiation is explained through the conversion of the non-thermal energy into thermal radiation.

The picture in this model is as follows. After the supernova explosion, a strongly magnetized pulsar may be left as a compact remnant, a fraction of which will have the ~ 1 -10 ms initial spin period required for a SLSN. As the pulsar spins down, the rotational energy is extracted in the form of a magnetized relativistic wind, forming a newborn PWN. Observations of nearby Galactic PWNe suggest that most of the spin-down energy must be dissipated inside or around the termination shock (Gaensler & Slane 2006), in the form of highly relativistic electrons and positrons with a Lorentz factor $\gamma_e \sim 10^5 - 10^6$. Because of this, nascent PWNe are expected to be sources of x-rays and gamma-rays from months to years after the explosion (Murase et al. 2015). Additionally, ~ 1 -10 years after the explosion, quasi-steady synchrotron emission has been predicted to be detectable at submillimeter frequencies (See Chapter 3). Chapter

Name	Redshift	RA	Dec	$P_{-3}, B_{13}, M_{\text{ej}}$ (min)	$P_{-3}, B_{13}, M_{\text{ej}}$ (max)
SN2015bn	0.1136	11:33:41.57	+00:43:32.2	1.0, 2.1, 17	1.4, 1.0, 5
SN2016ard	0.2	14:10:44.56	-10:09:35.42	1.0, 6.0, 12	2.2, 1.7, 1.5

TABLE 5.1: Parameters of Targeted SNe ($P = 10^{-3}P_{-3}$ s, $B = 10^{13}B_{13}$ G, and M_{ej} in unit of M_{\odot}).

3 also shows that radio emission from a forward shock with the ambient circumstellar material is negligible for Type-I SLSNe with such ages, and this additional component has a rising light curve with $\propto t^3$. Submillimeter ALMA observations are preferable to lower-frequency radio observation, such as those by VLA, since lower-frequency radio emission is more greatly affected by free-free and synchrotron absorption (Murase et al. 2016).

The importance of non-thermal signatures from newborn pulsars has been further highlighted by the discovery of FRBs. Recent observations of the repeating FRB 121102 have established FRBs to be extragalactic (Chatterjee et al. 2017; Marcote et al. 2017), implying that they are the most luminous radio transients in the Universe. The most common model progenitors for FRBs are magnetars and rapidly-rotating pulsars. Radio and submillimeter synchrotron emission was predicted from the nebulae (Murase et al. 2016) before the discovery of the persistent emission associated with FRB 121102 (Kashiyama & Murase 2017; Marcote et al. 2017). The physical setup in that model is essentially the same as the pulsar-driven SLSN model, and both are preferentially hosted by dwarf, star-forming galaxies (Chatterjee et al. 2017; Nicholl et al. 2017d), so there is a strong possibility of a connection between FRBs and pulsar-driven SLSNe (Marcote et al. 2017; Murase et al. 2016).

To summarize, non-thermal emission from newborn neutron stars is promising, and ALMA’s submillimeter observations should give us a crucial test of the pulsar-driven scenario for SLSNe, and reveal the possible connection among SLSNe, GRBs, Type-Ibc SNe, and FRBs.

5.3 Description of Proposed Observations

We propose to observe two specific objects, SN2015bn and SN2016ard, which have both had about 1-2 years elapse since the explosion. SN2015bn is one of the brightest Type-I SLSNe on record, and its predicted non-thermal flux is higher than $\sim 300 \mu\text{Jy}$ (Figure 5.1, top), even in the $P = 1$ ms case, which gives the most pessimistic flux. For a 5σ detection, we request a sensitivity of $200 \mu\text{Jy}$, which corresponds to observation times of 0.4 hrs with band 3 and 0.5 hrs with band 6. We hope for a time interval of less than 1-2 weeks. The 100 GHz emission is predicted to be intrinsically brighter (compare dashed blue/red curves of Figure 5.1), but the observed 230 GHz flux could be higher due to smaller attenuation (compare solid red/blue curves of Figure 5.1). The detectability of this source is not as sensitive to uncertainty if multiple bands are used. The nebular emission is predicted to have a flat synchrotron spectrum, $F_{\nu} \propto \nu^{-0.5} - \nu^0$, which can be useful to discriminate it from thermal or dust origin, which has $F_{\nu} \propto \nu^2 - \nu^4$. The other proposed target, SN2016ard, requires a longer exposure time due to its larger distance. For a 5σ detection, we request a sensitivity of $30 \mu\text{Jy}$, which corresponds to observation times of 6.2 hrs with band 3 and 12.8 hrs with band 6.

We request quasi-single epoch observations for Cycle 5. The PWN emission is quasi-steady but will decline slowly over the timescale of a few months, which can

be tested once a source is detected. Future multi-epoch observations will allow us to better discriminate the nebular synchrotron emission from other possibilities such as dust emission, active galactic nuclei (Doi et al. 2011), and possible ejecta interactions with the ambient material.

The reason for selecting SN2015bn and SN2016ard is as follows. We performed detailed calculations of submillimeter emission from 10 recent bright SLSNe with good quality optical light curve data. (Six are shown in Chapter 3, and we modelled four additional SLSNe that occurred in 2015 and 2016.) Through modelling the optical light curves, we extracted spin-down parameters B and P and the ejecta mass M_{ej} , which we then used in the submillimeter calculation. We finally found that only two sources, SN2015bn and SN2016ard, have the potential to be detected by ALMA.

5.4 Feasibility

The detectability of submillimeter emission from SLSNe depends on B , P , M_{ej} , which are determined from modelling the optical emission (see Table 5.1). As in Chapter 3, we fit the light curves of SN2015bn and SN2016ard, then calculated submillimeter synchrotron emission from the time-evolving PWNe, considering all relevant radiative processes such as synchrotron self-absorption, the Razin effect, and free-free absorption. The observable flux densities are predicted to be $\sim 400 - 3000 \mu\text{Jy}$ for SN2015bn and $\sim 30 - 600 \mu\text{Jy}$ for SN2016ard (see Figure 5.1), which should be reached with 5σ significance by the proposed integration time. These are both extragalactic point sources, and their coordinates put them well inside the ALMA field of view.

The unique capabilities of ALMA add other strong advantages to this proposal. Firstly, submillimeter emission can largely avoid the strong attenuation in the ejecta at early times, which is a large problem with observations at lower frequencies such as those in the VLA band. Secondly, Target-of-Opportunity observations by ALMA are not necessary, because although SNe themselves are month-timescale transients, radio and submillimeter emission lasts longer, even up to decades in some cases. Therefore, sequential observations can be planned later. Finally, thanks to the great sensitivity of ALMA, even non-detections give severe constraints on the pulsar-driven model and its parameters. Together with the optical and X-ray information, the simple rapidly-rotating pulsar model for SLSNe can be ruled out by non-detections from ALMA.

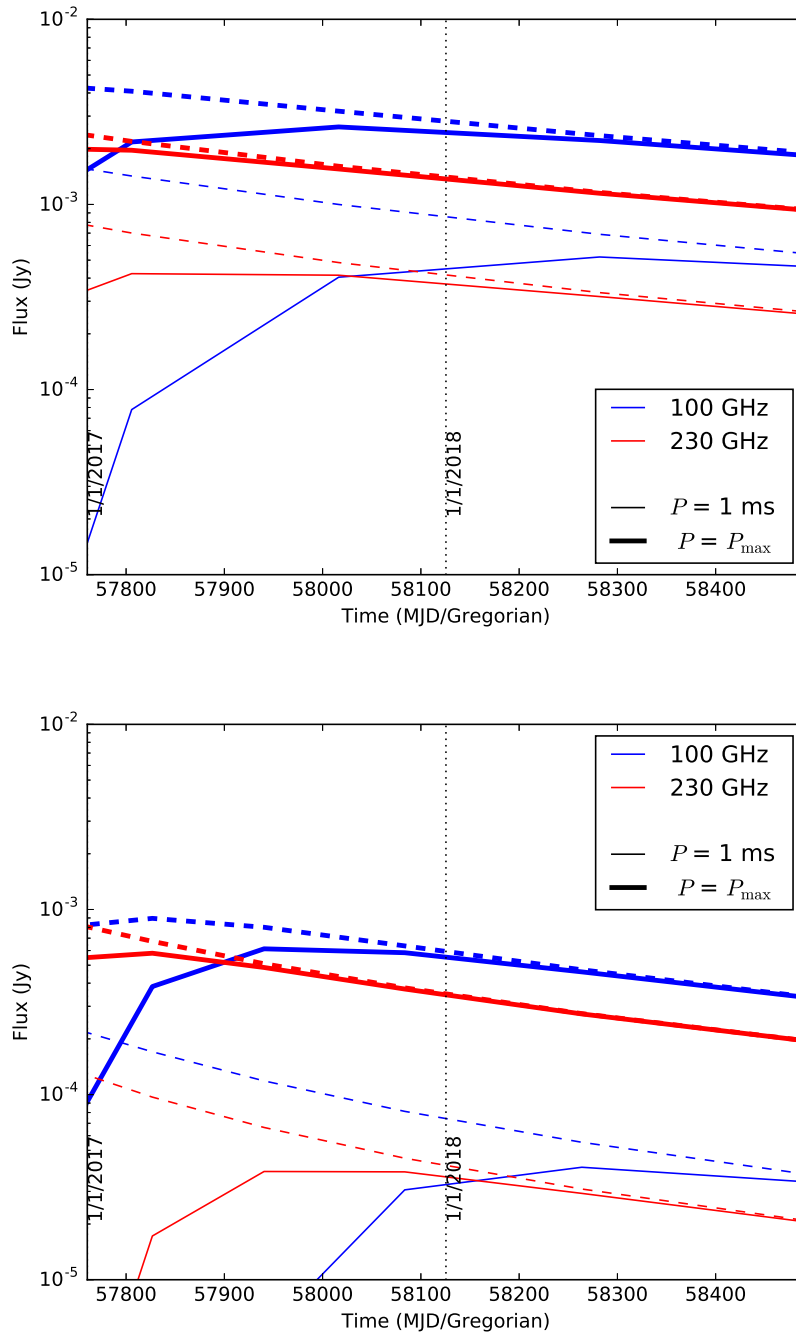


FIGURE 5.1: Synchrotron emission predicted for SN2015bn (top) and SN2016ard (bottom). The thin (thick) curves correspond to the minimum (maximum) flux predictions (see Table 5.1 for the used parameters). Solid (dashed) curves are with (without) free-free absorption in the SN ejecta.

Chapter 6

Concluding Remarks

The observations proposed in Chapter 5 will be an interesting turning point for the pulsar-driven SN community, as this is by far the most studied model for SLSNe and the optical emission from most SLSNe can be fit with the pulsar-driven model (Nicholl et al. 2017c).

If a detection is made for both supernovae, this will be incredibly strong evidence for the pulsar-driven model, as there are few processes that could explain a synchrotron source with the luminosity we predict associated with a supernova remnant. Follow-up multiwavelength observations of confirmed and potential candidate SNe could give us far greater insight into the formation and early life of a pulsar, how the magnetic field is generated, and the early, and expectedly violent, behaviour of the PWN. An example of something we could learn is the electron injection spectrum in early times; we used a spectrum based from the Crab Nebula (Equation 2.21) because these observations are all we have now, but this nebula is still almost 1000 years old, while our detected PWNe would be 2-3 years old.

If a detection is not made for either supernovae, then we should abandon the pulsar-driven model, as these two sources are almost surely not pulsar-powered, or at least work on other models as feverishly as we currently work on the pulsar-driven model. The logical next step is to try and predict unique emission or unique behaviour from another model, like from a black-hole accretion disk or collapsar, calculate emission predictions, and propose observations of interesting candidates, much like we did here.

If the detection is made for only one of the sources, then we have a very curious situation. Since our observations should cover the entire parameter space in the pulsar-driven model, it is unlikely that the emission would simply be too faint to see. In this case, we should conclude that only some SLSNe are powered by pulsars and some by other energy sources; this conclusion is not ruled out by the other scenarios either, which is why the sample size should be increased regardless of the outcome. From here, theorists should focus on what optical and spectral properties in the early emission could differentiate a pulsar-driven supernova from other energy sources, how the rates are affected by having multiple energy sources, and still, how to uniquely detect each energy source.

Some recent studies present interesting constraints or opportunities. X-ray and gamma-ray studies of many SLSNe put strong constraints on pulsar parameters (Margutti et al. 2017a; Renault-Tinacci et al. 2017), with the x-ray study favoring large fields and ejecta masses (closer to our $P = 1$ ms scenario). The excess ultraviolet radiation from nearby Type-I SLSN Gaia2016apd (also known as SN2016eay) (Yan et al. 2017a) has been said to be consistent with both the magentar model (Kangas et al. 2017; Nicholl et al. 2017b) and the circumstellar interaction model normally used for Type-II SLSNe (Tolstov et al. 2017). Another interesting recently observed source is SN2017egm, which is the closest observed SLSN at $z \sim 0.03$ and located in a massive, metal-rich

spiral galaxy (Chen et al. 2017; Dong et al. 2017), although it may have originated from a young, sub-solar metallicity environment in that galaxy (Izzo et al. 2017); it is also consistent with the pulsar-driven model (Nicholl et al. 2017a). Unfortunately, both Gaia2016apd and SN2017egm lie outside the field of view of ALMA, so follow-up observations will have to be done with a different telescope; however they may still be detectable with something like the James Clerk Maxwell Telescope (JCMT). Recent surveys have also detected Type-I SLSNe with late $H\alpha$ emission (Yan et al. 2017b), Type-I SLSNe at $z > 1.5$ (Lunnan et al. 2018; Pan et al. 2017), and a strange Type-II SLSNe that also seems to corespond to the pulsar-driven model (Arcavi et al. 2017; Dessart 2018). Recent observations of FRB121102 have detected an extremely large rotation measure (Michilli et al. 2018), which points to a progenitor with an extreme magneto-ionic environment.

To fully understand the emission from pulsar-driven SNe, phenomenological models like those in Section 2.1 will not be sufficient, and full radiative hydrodynamics simulations will be the way forward. One-dimensional simulations have been done for a few years (e.g. Kasen & Bildsten 2010), but may miss multidimensional hydrodynamic instabilities such as Rayleigh-Taylor instabilities (Blondin et al. 2001; Blondin & Ellison 2001; Jun 1998), Richtmyer-Meshkov instabilities (Meshkov 1969; Richtmyer 1960), and non-linear thin shell instabilities (Vishniac 1994). The energy injection itself could also be realized in aspherical ways, such as in an LGRB. Recently, some two-dimensional studies were performed (Chen et al. 2016; Suzuki & Maeda 2017), but they left out important information on dust formation and ionization in the supernova ejecta. In order to fully understand the broadband emission from nascent pulsars and PWNe, the author intends to build the most complete ejecta simulation possible in an effort to push our understanding as far as it can go.

Appendix A

Analytic Integration of Equation 2.144

In solving for the spectrum of radiation for an optically thin dust cloud, we derived Equation 2.144, which has the form

$$dL_\nu = \frac{k_1 r^2 dr}{e^{k_2 \sqrt{r}} - 1}, \quad (\text{A.1})$$

where

$$k_1 = \frac{32\pi^3 n_{\text{dust}} Q(a) h\nu^3}{c^2} \quad (\text{A.2})$$

$$k_2 = \frac{h\nu}{k_b} \left(\frac{16\pi\sigma}{L_{\text{opt/UV}}} \frac{\langle Q \rangle_T}{Q_{\text{opt/UV}}} \right)^{1/4}. \quad (\text{A.3})$$

In this derivation, we take $\langle Q \rangle_T$ to be independent of temperature, and thus radius.

Beginning with Equation A.1, we can rewrite L_ν as

$$L_\nu = \frac{k_1}{k_2^6} \int_{R_c}^{R_{\text{ej}}} (k_2 \sqrt{r})^4 \frac{k_2^2 dr}{e^{k_2 \sqrt{r}} - 1}. \quad (\text{A.4})$$

Substituting $x = k_2 \sqrt{r}$ and working out the differential as

$$\frac{k_2 dr}{2\sqrt{r}} = dx \quad (\text{A.5})$$

$$k_2^2 dr = 2x dx. \quad (\text{A.6})$$

Substituting this into Equation A.4 gives

$$L_\nu = \frac{2k_1}{k_2^6} \int_{x_{R_c}}^{x_{R_{\text{ej}}}} \frac{x^5 dx}{e^x - 1} = \frac{2k_1}{k_2^6} \int_{x_{R_c}}^{x_{R_{\text{ej}}}} \frac{x^5 e^{-x} dx}{1 - e^{-x}}, \quad (\text{A.7})$$

and using the identity

$$\frac{e^{-x}}{1 - e^{-x}} = \sum_{n=1}^{\infty} e^{-nx} \quad (\text{A.8})$$

allows us to write

$$L_\nu = \frac{2k_1}{k_2^6} \sum_{n=1}^{\infty} \int_{x_{R_c}}^{x_{R_{\text{ej}}}} x^5 e^{-nx} dx, \quad (\text{A.9})$$

which can be solved by repeated integration by parts. The solution of the integral is

$$L_\nu = \frac{2k_1}{k_2^6} \sum_{n=1}^{\infty} (-e^{nx}) \left(\frac{x^5}{n} + \frac{5x^4}{n^2} + \frac{20x^3}{n^3} + \frac{60x^2}{n^4} + \frac{120x}{n^5} + \frac{120}{n^6} \right) \Bigg|_{x_{R_c}}^{x_{R_{ej}}}. \quad (\text{A.10})$$

This solution can be expressed as the sum of polylogarithmic functions, where a polylogarithm $\text{Li}_s(z)$ of order s is defined by

$$\text{Li}_s(z) = \sum_{k=1}^{\infty} \frac{z^k}{k^s}, \quad (\text{A.11})$$

allowing us to write, in summation notation,

$$L_\nu = \frac{2k_1}{k_2^6} \sum_{n=1}^6 \frac{120x^{(6-n)}}{(6-n)!} \text{Li}_n(e^{-x}) \Bigg|_{x_{R_c}}^{x_{R_{ej}}}. \quad (\text{A.12})$$

In order to simplify $2k_1/k_2^6$, we use the relation

$$\frac{h\nu}{k_B T} = k_2 \sqrt{r} \quad (\text{A.13})$$

$$\frac{1}{k_2} = \frac{k_B T \sqrt{r}}{h\nu} \quad (\text{A.14})$$

which holds for all radii, including R_c . Using this relation and substituting Equations A.2 and A.3 into Equation A.12, we finally obtain

$$L_\nu = \frac{64\pi^3 n_{\text{dust}} Q(a) k_B^6 T_c^3 R_c^3}{h^5 \nu^3 c^2} \sum_{n=1}^6 \frac{120x^{(6-n)}}{(6-n)!} \text{Li}_n(e^{-x}) \Bigg|_{x_{R_c}}^{x_{R_{ej}}}, \quad (\text{A.15})$$

which is Equation 2.145.

Bibliography

- Abbott, B. P., Abbott, R., Abbott, T. D., et al. 2017a, *ApJ*, 848, L13
- . 2017b, *Physical Review Letters*, 119, 161101
- . 2017c, *ApJ*, 848, L12
- Abdikamalov, E., Ott, C. D., Radice, D., et al. 2015, *ApJ*, 808, 70
- Abdo, A. A., Ackermann, M., Arimoto, M., et al. 2009, *Science*, 323, 1688
- Abraham, F. 1974, Press, New York, 1974
- Adler, S. L. 1971, *Annals of Physics*, 67, 599
- Akiyama, S., Wheeler, J. C., Meier, D. L., & Lichtenstadt, I. 2003, *ApJ*, 584, 954
- Alexander, K. D., Berger, E., Fong, W., et al. 2017, *ApJ*, 848, L21
- Alves, E. P., Grismayer, T., Fonseca, R. A., & Silva, L. O. 2014, *New Journal of Physics*, 16, 035007
- Antoniadis, J., Freire, P. C., Wex, N., et al. 2013, *Science*, 340, 1233232
- Aptekar, R., Frederiks, D., Golenetskii, S., et al. 2001, *The Astrophysical Journal Supplement Series*, 137, 227
- Arcavi, I., Howell, D. A., Kasen, D., et al. 2017, *Nature*, 551, 210
- Argyle, E., & Gower, J. F. R. 1972, *ApJ*, 175, L89
- Arnett, W. D. 1982, *ApJ*, 253, 785
- Arons, J. 1983, *ApJ*, 266, 215
- . 2003, *ApJ*, 589, 871
- Arzoumanian, Z., Chernoff, D. F., & Cordes, J. M. 2002, *ApJ*, 568, 289
- Atoyan, A. M., & Aharonian, F. A. 1996, *MNRAS*, 278, 525
- Atteia, J.-L., Boer, M., Hurley, K., et al. 1987, *The Astrophysical Journal*, 320, L105
- Baade, W. 1938, *ApJ*, 88, 285
- Baade, W., & Zwicky, F. 1934, *Proceedings of the National Academy of Science*, 20, 254
- Baade, W., & Zwicky, F. 1934, *Physical Review*, 46, 76
- Bannister, K. W., Shannon, R. M., Macquart, J.-P., et al. 2017, *ApJ*, 841, L12
- Barat, C., Hayles, R., Hurley, K., et al. 1983, *Astronomy and Astrophysics*, 126, 400

- Barlow, M. J., Krause, O., Swinyard, B. M., et al. 2010, *A&A*, 518, L138
- Barrau, A., Rovelli, C., & Vidotto, F. 2014, *Phys. Rev. D*, 90, 127503
- Bassa, C. G., Tendulkar, S. P., Adams, E. A. K., et al. 2017, *ApJ*, 843, L8
- Bastian, T. S., Benz, A. O., & Gary, D. E. 1998, *ARA&A*, 36, 131
- Begelman, M. C., & Li, Z.-Y. 1992, *ApJ*, 397, 187
- Bégué, D., Burgess, J. M., & Greiner, J. 2017, *ArXiv e-prints*, arXiv:1710.07987
- Beloborodov, A. M. 2017, *ArXiv e-prints*, arXiv:1702.08644
- Berger, E., Fong, W., & Chornock, R. 2013, *ApJ*, 774, L23
- Berger, E., Soderberg, A. M., & Frail, D. A. 2003, *GRB Coordinates Network*, 2014
- Bethe, H. A., Brown, G. E., Applegate, J., & Lattimer, J. M. 1979, *Nuclear Physics A*, 324, 487
- Bevan, A., Barlow, M. J., & Milisavljevic, D. 2017, *MNRAS*, 465, 4044
- Bhattacharya, D., & Soni, V. 2007, *ArXiv e-prints*, arXiv:0705.0592
- Bianchi, S., & Schneider, R. 2007, *MNRAS*, 378, 973
- Bisnovatyi-Kogan, G. S. 1971, *Soviet Ast.*, 14, 652
- Blander, M., & Katz, J. L. 1972, *Journal of Statistical Physics*, 4, 55
- Blandford, R. D., Ostriker, J. P., Pacini, F., & Rees, M. J. 1973, *A&A*, 23, 145
- Blinnikov, S. I., Novikov, I. D., Perevodchikova, T. V., & Polnarev, A. G. 1984, *Soviet Astronomy Letters*, 10, 177
- Blondin, J. M., Chevalier, R. A., & Frierson, D. M. 2001, *ApJ*, 563, 806
- Blondin, J. M., & Ellison, D. C. 2001, *ApJ*, 560, 244
- Blondin, J. M., Mezzacappa, A., & DeMarino, C. 2003, *ApJ*, 584, 971
- Bloom, J. S., Prochaska, J. X., Pooley, D., et al. 2006, *ApJ*, 638, 354
- Bloom, J. S., Giannios, D., Metzger, B. D., et al. 2011, *Science*, 333, 203
- Boër, M., Gendre, B., & Stratta, G. 2015, *ApJ*, 800, 16
- Boggs, S. E., Zoglauer, A., Bellm, E., et al. 2007, *The Astrophysical Journal*, 661, 458
- Bogovalov, S. V., Chechetkin, V. M., Koldoba, A. V., & Ustyugova, G. V. 2005, *MNRAS*, 358, 705
- Boischot, A., & Clavelier, B. 1967, *Astrophys. Lett.*, 1, 7
- Bombaci, I. 1996, *Astronomy and Astrophysics*, 305, 871
- Bonanno, A., Urpin, V., & Belvedere, G. 2005, *A&A*, 440, 199
- Borkowski, J., Gotz, D., Mereghetti, S., et al. 2004, *GRB Coordinates Network*, 2920

- Brahe, T. 1573, Kopenhagen: Laurentius Benedictus
- Bramante, J., & Linden, T. 2014, *Physical Review Letters*, 113, 191301
- Branch, D., & Tammann, G. A. 1992, *ARA&A*, 30, 359
- Brecher, K., Fesen, R. A., Maran, S. P., & Brandt, J. C. 1983, *The Observatory*, 103, 106
- Bromberg, O., & Tchekhovskoy, A. 2016, *MNRAS*, 456, 1739
- Bromberg, O., Tchekhovskoy, A., Gottlieb, O., Nakar, E., & Piran, T. 2017, *ArXiv e-prints*, arXiv:1710.05897
- Brownell, Jr., D. H., & Callaway, J. 1969, *Nuovo Cimento B Serie*, 60, 169
- Brownlee, D. 2003, *Rare Earth: Why complex life is uncommon in the Universe* (Springer)
- Bucciantini, N. 2012, in *IAU Symposium*, Vol. 279, *Death of Massive Stars: Supernovae and Gamma-Ray Bursts*, ed. P. Roming, N. Kawai, & E. Pian, 289–296
- Bucciantini, N., Blondin, J. M., Del Zanna, L., & Amato, E. 2003, *A&A*, 405, 617
- Bucciantini, N., Quataert, E., Arons, J., Metzger, B. D., & Thompson, T. A. 2007, *MNRAS*, 380, 1541
- . 2008, *MNRAS*, 383, L25
- Bucciantini, N., Quataert, E., Metzger, B. D., et al. 2009, *MNRAS*, 396, 2038
- Bucciantini, N., Thompson, T. A., Arons, J., Quataert, E., & Del Zanna, L. 2006, *MNRAS*, 368, 1717
- Buras, R., Rampp, M., Janka, H.-T., & Kifonidis, K. 2006, *A&A*, 447, 1049
- Burgio, G., Baldo, M., Sahu, P., & Schulze, H.-J. 2002, *Physical Review C*, 66, 025802
- Burrows, A., Dessart, L., Livne, E., Ott, C. D., & Murphy, J. 2007a, *ApJ*, 664, 416
- Burrows, A., & Lattimer, J. M. 1986, *ApJ*, 307, 178
- Burrows, A., Livne, E., Dessart, L., Ott, C. D., & Murphy, J. 2006a, *ApJ*, 640, 878
- . 2007b, *ApJ*, 655, 416
- Burrows, D. N., Grupe, D., Capalbi, M., et al. 2006b, *ApJ*, 653, 468
- Caleb, M., Flynn, C., Bailes, M., et al. 2017, *MNRAS*, 468, 3746
- Cameron, P., Chandra, P., Ray, A., et al. 2005, *Nature*, 434, 1112
- Camilo, F., Ransom, S. M., Gaensler, B. M., et al. 2006, *ApJ*, 637, 456
- Campbell, P., Hill, M., Howe, R., et al. 2005, *GRB Coordinates Network*, 2932, 1
- Chamel, N., Haensel, P., Zdunik, J. L., & Fantina, A. 2013, *International journal of modern physics E*, 22, 1330018
- Champion, D. J., Petroff, E., Kramer, M., et al. 2016, *MNRAS*, 460, L30

- Chandrasekhar, S. 1931, *ApJ*, 74, 81
- . 1935, *MNRAS*, 95, 207
- Chatterjee, S., Law, C. J., Wharton, R. S., et al. 2017, *ArXiv e-prints*, arXiv:1701.01098
- Chattopadhyay, T., Misra, R., Chattopadhyay, A. K., & Naskar, M. 2007, *ApJ*, 667, 1017
- Chatzopoulos, E., Wheeler, J. C., & Vinko, J. 2012, *ApJ*, 746, 121
- Chen, K.-J., Woosley, S. E., & Sukhbold, T. 2016, *ApJ*, 832, 73
- Chen, T.-W., Smartt, S. J., Bresolin, F., et al. 2013, *ApJ*, 763, L28
- Chen, T.-W., Schady, P., Xiao, L., et al. 2017, *ApJ*, 849, L4
- Cheng, B., Epstein, R. I., Guyer, R. A., & Young, A. C. 1996, *Nature*, 382, 518
- Cheng, K. S., Ho, C., & Ruderman, M. 1986a, *ApJ*, 300, 500
- . 1986b, *ApJ*, 300, 522
- Chevalier, R. A. 1977, in *Astrophysics and Space Science Library*, Vol. 66, *Supernovae*, ed. D. N. Schramm, 53
- Chevalier, R. A. 1989, *ApJ*, 346, 847
- . 1998, *ApJ*, 499, 810
- . 2005, *ApJ*, 619, 839
- Chevalier, R. A., & Fransson, C. 1992, *ApJ*, 395, 540
- . 1994, *ApJ*, 420, 268
- Chevalier, R. A., & Irwin, C. M. 2011, *ApJ*, 729, L6
- Chin, Y.-N., & Huang, Y.-L. 1994, *Nature*, 371, 398
- Chodorowski, M. J., Zdziarski, A. A., & Sikora, M. 1992, *ApJ*, 400, 181
- Chugai, N. N., & Danziger, I. J. 1994, *MNRAS*, 268, 173
- Clark, D. H., & Stephenson, F. R. 1977, *The historical supernovae*
- Cline, D. B. 1996, *Nuclear Physics A*, 610, 500
- Cline, T. 1980, *Comments on Astrophysics*, 9, 13
- Cline, T., Desai, U., Teegarden, B., et al. 1982, *The Astrophysical Journal*, 255, L45
- Colgate, S. A. 1979, *ApJ*, 232, 404
- Connor, L., Sievers, J., & Pen, U.-L. 2016, *MNRAS*, 458, L19
- Cooke, J., Sullivan, M., Gal-Yam, A., et al. 2012, *Nature*, 491, 228
- Cordes, J. M., & Wasserman, I. 2016, *MNRAS*, 457, 232
- Costa, E., Frontera, F., Heise, J., et al. 1997, *Nature*, 387, 783

- Cowperthwaite, P. S., Berger, E., Villar, V. A., et al. 2017, *ApJ*, 848, L17
- Cox, D. P. 1972, *ApJ*, 178, 159
- Cutler, C. 2002, *Phys. Rev. D*, 66, 084025
- Cutler, C., & Flanagan, É. E. 1994, *Phys. Rev. D*, 49, 2658
- Cutler, C., & Jones, D. I. 2001, *Phys. Rev. D*, 63, 024002
- Dai, Z. G., Wang, J. S., Wu, X. F., & Huang, Y. F. 2016a, *ApJ*, 829, 27
- Dai, Z. G., Wang, S. Q., Wang, J. S., Wang, L. J., & Yu, Y. W. 2016b, *ApJ*, 817, 132
- Dall’Osso, S., Shore, S. N., & Stella, L. 2009, *MNRAS*, 398, 1869
- De Cia, A., Gal-Yam, A., Rubin, A., et al. 2017, *ArXiv e-prints*, arXiv:1708.01623
- De Colle, F., Lu, W., Kumar, P., Ramirez-Ruiz, E., & Smoot, G. 2017, *ArXiv e-prints*, arXiv:1701.05198
- de Jager, O. C., Harding, A. K., Michelson, P. F., et al. 1996, *ApJ*, 457, 253
- de Mink, S. E., & King, A. 2017, *ApJ*, 839, L7
- Del Zanna, L., Amato, E., & Bucciantini, N. 2004, *A&A*, 421, 1063
- DeLaunay, J. J., Fox, D. B., Murase, K., et al. 2016, *ApJ*, 832, L1
- den Hartog, P. R. 2008
- Deng, W., & Zhang, B. 2014, *ApJ*, 783, L35
- Dermer, C. D., Murase, K., & Takami, H. 2012, *ApJ*, 755, 147
- Dessart, L. 2018, *ArXiv e-prints*, arXiv:1801.05340
- Dessart, L., Hillier, D. J., Livne, E., et al. 2011, *MNRAS*, 414, 2985
- Dessart, L., Hillier, D. J., Waldman, R., Livne, E., & Blondin, S. 2012, *MNRAS*, 426, L76
- Dessart, L., Hillier, D. J., Woosley, S., et al. 2015, *MNRAS*, 453, 2189
- Dessart, L., John Hillier, D., Yoon, S.-C., Waldman, R., & Livne, E. 2017, *A&A*, 603, A51
- Dexter, J., & Kasen, D. 2013, *ApJ*, 772, 30
- Doi, A., Nakanishi, K., Nagai, H., Kohno, K., & Kamenno, S. 2011, *AJ*, 142, 167
- Dong, S., Bose, S., Chen, P., et al. 2017, *The Astronomer’s Telegram*, 10498
- Draine, B. T., & Lee, H. M. 1984, *ApJ*, 285, 89
- Drout, M. R., Soderberg, A. M., Gal-Yam, A., et al. 2011, *ApJ*, 741, 97
- Duncan, R. C. 2001, *arXiv preprint astro-ph/0103235*
- Duncan, R. C. 2004, in *Cosmic explosions in three dimensions*, ed. P. Höflich, P. Kumar, & J. C. Wheeler, 285

- Duncan, R. C., & Thompson, C. 1992, *The Astrophysical Journal*, 392, L9
- Durant, M., & van Kerkwijk, M. H. 2006, *ApJ*, 650, 1070
- Dwek, E., & Arendt, R. G. 2015, *ApJ*, 810, 75
- Dwek, E., Galliano, F., & Jones, A. P. 2007, *ApJ*, 662, 927
- Eichler, D., Livio, M., Piran, T., & Schramm, D. N. 1989, *Nature*, 340, 126
- Elenbaas, C., Huppenkothen, D., Omand, C., et al. 2017, *MNRAS*, 471, 1856
- Epstein, R. I., Colgate, S. A., & Haxton, W. C. 1988, *Physical Review Letters*, 61, 2038
- Falcke, H., & Rezzolla, L. 2014, *A&A*, 562, A137
- Feroci, M., Hurley, K., Duncan, R., & Thompson, C. 2001, *The Astrophysical Journal*, 549, 1021
- Fewell, M. P. 1995, *American Journal of Physics*, 63, 653
- Fishman, G. J., & Meegan, C. A. 1995, *ARA&A*, 33, 415
- Flanagan, É. É., & Hughes, S. A. 1998, *Phys. Rev. D*, 57, 4535
- Frail, D., Kulkarni, S., & Bloom, J. 1999, *Nature*, 398, 127
- Frail, D. A., Kulkarni, S. R., Nicastro, L., Feroci, M., & Taylor, G. B. 1997, *Nature*, 389, 261
- Frail, D. A., Kulkarni, S. R., Sari, R., et al. 2001, *ApJ*, 562, L55
- Fraley, G. S. 1968, *Ap&SS*, 2, 96
- Frederiks, D., Aptekar, R., Cline, T., et al. 2008, in *American Institute of Physics Conference Series*, Vol. 1000, *American Institute of Physics Conference Series*, ed. M. Galassi, D. Palmer, & E. Fenimore, 271–275
- Frontera, F., & Piro, L. 1999, *A&AS*, 138, 395
- Fujimoto, S.-i., Nishimura, N., & Hashimoto, M.-a. 2008, *ApJ*, 680, 1350
- Fuller, J., & Ott, C. D. 2015, *MNRAS*, 450, L71
- Gaensler, B., Kouveliotou, C., Gelfand, J., et al. 2005, *Nature*, 434, 1104
- Gaensler, B. M., & Slane, P. O. 2006, *ARA&A*, 44, 17
- Gajjar, V., Siemion, A. P. V., MacMahon, D. H. E., et al. 2017, *The Astronomer's Telegram*, 10675
- Gal-Yam, A. 2012, *Science*, 337, 927
- Gal-Yam, A., & Leonard, D. C. 2009, *Nature*, 458, 865
- Gal-Yam, A., Mazzali, P., Ofek, E. O., et al. 2009, *Nature*, 462, 624
- Galama, T. J., Vreeswijk, P. M., van Paradijs, J., et al. 1998, *Nature*, 395, 670
- Gall, C., Hjorth, J., & Andersen, A. C. 2011, *A&A Rev.*, 19, 43

- Gaunt, J. A. 1930, *Philosophical Transactions of the Royal Society of London Series A*, 229, 163
- Gehrels, N., Sarazin, C. L., O'Brien, P. T., et al. 2005, *Nature*, 437, 851
- Gelfand, J. D., Slane, P. O., & Zhang, W. 2009, *ApJ*, 703, 2051
- Gendre, B., Stratta, G., Atteia, J. L., et al. 2013, *ApJ*, 766, 30
- Geng, J. J., & Huang, Y. F. 2015, *ApJ*, 809, 24
- Ghisellini, G., & Svensson, R. 1991, *MNRAS*, 252, 313
- Giacconi, R., Gursky, H., Paolini, F. R., & Rossi, B. B. 1962, *Physical Review Letters*, 9, 439
- Ginzburg, V., & Syrovatskii, S. 1965, *Annual Review of Astronomy and Astrophysics*, 3, 297
- Ginzburg, V. L., & Syrovatskii, S. I. 1965, *ARA&A*, 3, 297
- Göğüş, E., Kouveliotou, C., Woods, P. M., et al. 2001, *The Astrophysical Journal*, 558, 228
- Göğüş, E., Woods, P. M., Kouveliotou, C., et al. 1999, *The Astrophysical Journal Letters*, 526, L93
- . 2000, *The Astrophysical Journal Letters*, 532, L121
- Gold, T. 1968, *Nature*, 218, 731
- Goldreich, P., & Julian, W. H. 1969, *ApJ*, 157, 869
- Goldreich, P., & Reisenegger, A. 1992, *ApJ*, 395, 250
- Goldreich, P., & Weber, S. V. 1980, *ApJ*, 238, 991
- Golenetskii, S., Ilyinskii, V., & Mazets, E. 1984
- Gomez, H. L., Krause, O., Barlow, M. J., et al. 2012, *ApJ*, 760, 96
- Gotthelf, E. V., Vasisht, G., Boylan-Kolchin, M., & Torii, K. 2000, *ApJ*, 542, L37
- Gottlieb, O., Nakar, E., Piran, T., & Hotokezaka, K. 2017, *ArXiv e-prints*, arXiv:1710.05896
- Götz, D., Mereghetti, S., Molkov, S., et al. 2006, *Astronomy & Astrophysics*, 445, 313
- Goumans, T. P. M., & Bromley, S. T. 2012, *MNRAS*, 420, 3344
- Greiner, J., Mazzali, P. A., Kann, D. A., et al. 2015, *Nature*, 523, 189
- Gruzinov, A. 2005, *Physical Review Letters*, 94, 021101
- Gu, W.-M., Dong, Y.-Z., Liu, T., Ma, R., & Wang, J. 2016, *ApJ*, 823, L28
- Gualtieri, L., Ciolfi, R., & Ferrari, V. 2011, *Classical and Quantum Gravity*, 28, 114014
- Guillochon, J., Parrent, J., Kelley, L. Z., & Margutti, R. 2017, *ApJ*, 835, 64

- Gupta, Y., Mitra, D., Green, D. A., & Acharyya, A. 2005, *Current Science*, 89, 853
- Gutenberg, B., & Richter, C. F. 1956, *Annals of Geophysics*, 9, 1
- Haensel, P., & Bonazzola, S. 1996, *A&A*, 314, 1017
- Haensel, P., Potekhin, A. Y., & Yakovlev, D. G. 2007, *Neutron stars 1: Equation of state and structure*, Vol. 326 (Springer Science & Business Media)
- Hakkila, J., Giblin, T. W., Roiger, R. J., et al. 2003, *ApJ*, 582, 320
- Hallinan, G., Corsi, A., Mooley, K. P., et al. 2017, *ArXiv e-prints*, arXiv:1710.05435
- Hamilton, A. J. S., & Sarazin, C. L. 1984, *ApJ*, 287, 282
- Hamuy, M., Phillips, M. M., Suntzeff, N. B., et al. 1996, *AJ*, 112, 2391
- Hamuy, M., Maza, J., Phillips, M. M., et al. 1993, *AJ*, 106, 2392
- Hankins, T. H., Kern, J. S., Weatherall, J. C., & Eilek, J. A. 2003, *Nature*, 422, 141
- Harada, A., Nagakura, H., Iwakami, W., & Yamada, S. 2017, *ApJ*, 839, 28
- Harding, A. K., Baring, M. G., & Gonthier, P. L. 1997, *The Astrophysical Journal*, 476, 246
- Harding, A. K., & Lai, D. 2006, *Reports on Progress in Physics*, 69, 2631
- Harding, A. K., & Muslimov, A. G. 1998, *ApJ*, 508, 328
- Haxton, W. C. 1988, *Physical Review Letters*, 60, 1999
- Hayakawa, T., Iwamoto, N., Kajino, T., et al. 2006, *ApJ*, 648, L47
- Hessels, J. W., Ransom, S. M., Stairs, I. H., et al. 2006, *Science*, 311, 1901
- Hewish, A., Bell, S. J., Pilkington, J., Scott, P., & Collins, R. 1968, *Nature*, 217, 709
- Hewish, A., & Okoye, S. 1965, *Nature*, 207, 59
- Heyl, J. S., & Kulkarni, S. 1998, *The Astrophysical Journal Letters*, 506, L61
- Hirofani, K. 2006, *ApJ*, 652, 1475
- Horváth, I. 1998, *ApJ*, 508, 757
- Horváth, I., Balázs, L. G., Bagoly, Z., Ryde, F., & Mészáros, A. 2006, *A&A*, 447, 23
- Horvath, I., Toth, B. G., Hakkila, J., et al. 2017, *ArXiv e-prints*, arXiv:1710.11509
- Huggins, W. 1866, *MNRAS*, 26, 275
- Hulse, R. A., & Taylor, J. H. 1975, *ApJ*, 195, L51
- Hurley, K., Cline, T., Mazets, E., et al. 1999, *Nature*, 397, 41
- Hurley, K., Berger, E., Castro-Tirado, A., et al. 2002, *ApJ*, 567, 447
- Hurley, K., Boggs, S. E., Smith, D. M., et al. 2005, *Nature*, 434, 1098
- Inan, U., Lehtinen, N., Lev-Tov, S., et al. 1999, *Geophysical Research Letters*, 26, 3357

- Inan, U. S., Lehtinen, N. G., Moore, R., et al. 2007, *Geophysical research letters*, 34
- Indebetouw, R., Matsuura, M., Dwek, E., et al. 2014, *ApJ*, 782, L2
- Inserra, C., Bulla, M., Sim, S. A., & Smartt, S. J. 2016a, *ApJ*, 831, 79
- Inserra, C., Smartt, S. J., Jerkstrand, A., et al. 2013, *ApJ*, 770, 128
- Inserra, C., Smartt, S. J., Gall, E. E. E., et al. 2016b, *ArXiv e-prints*, arXiv:1604.01226
- Inserra, C., Nicholl, M., Chen, T.-W., et al. 2017, *MNRAS*, 468, 4642
- Ioka, K., Hotokezaka, K., & Piran, T. 2016, *ApJ*, 833, 110
- Ioka, K., & Nakamura, T. 2017, *ArXiv e-prints*, arXiv:1710.05905
- Ivezic, Z., Tyson, J., Abel, B., et al. 2008, *arXiv preprint arXiv:0805.2366*
- Iwamoto, K., Mazzali, P. A., Nomoto, K., et al. 1998, *Nature*, 395, 672
- Iwamoto, K., Nakamura, T., Nomoto, K., et al. 2000, *ApJ*, 534, 660
- Izzo, L., Thöne, C. C., García-Benito, R., et al. 2017, *ArXiv e-prints*, arXiv:1708.03856
- Janka, H.-T. 2012, *Annual Review of Nuclear and Particle Science*, 62, 407
- Janka, H.-T., Langanke, K., Marek, A., Martínez-Pinedo, G., & Müller, B. 2007, *Phys. Rep.*, 442, 38
- Johnston, S., & Romani, R. W. 2004, in *IAU Symposium*, Vol. 218, *Young Neutron Stars and Their Environments*, ed. F. Camilo & B. M. Gaensler, 315
- Jun, B.-I. 1998, *ApJ*, 499, 282
- Kalogera, V., & Baym, G. 1996, *The Astrophysical Journal Letters*, 470, L61
- Kangas, T., Blagorodnova, N., Mattila, S., et al. 2017, *MNRAS*, 469, 1246
- Kardashev, N. S. 1964, *AZh*, 41, 807
- Kasen, D., & Bildsten, L. 2010, *ApJ*, 717, 245
- Kasen, D., Woosley, S. E., & Heger, A. 2011, *ApJ*, 734, 102
- Kashiyama, K., Ioka, K., & Mészáros, P. 2013, *ApJ*, 776, L39
- Kashiyama, K., & Murase, K. 2017, *ApJ*, 839, L3
- Kashiyama, K., Murase, K., Bartos, I., Kiuchi, K., & Margutti, R. 2016, *ApJ*, 818, 94
- Katz, J. I. 2002, *The biggest bangs : the mystery of gamma-ray bursts, the most violent explosions in the universe*
- . 2016, *Modern Physics Letters A*, 31, 1630013
- Keane, E. F., & Kramer, M. 2008, *MNRAS*, 391, 2009
- Kennel, C. F., & Coroniti, F. V. 1984, *ApJ*, 283, 710
- Kepler, J. 1606, *Opera Omnia*, 2

- Khokhlov, A. M., Höflich, P. A., Oran, E. S., et al. 1999, *ApJ*, 524, L107
- Kirk, J. G., & Skjæraasen, O. 2003, *ApJ*, 591, 366
- Kirk, J. G., & Skjæraasen, O. 2004, in *IAU Symposium*, Vol. 218, *Young Neutron Stars and Their Environments*, ed. F. Camilo & B. M. Gaensler, 171
- Kisaka, S., Ioka, K., Kashiya, K., & Nakamura, T. 2017, *ArXiv e-prints*, arXiv:1711.00243
- Kiuchi, K., & Yoshida, S. 2008, *Phys. Rev. D*, 78, 044045
- Klebesadel, R., Strong, I., & Olson, R. 1973, L85
- Klebesadel, R. W., Strong, I. B., & Olson, R. A. 1973, *ApJ*, 182, L85
- Klein, O., & Nishina, Y. 1929, *Zeitschrift für Physik*, 52, 853
- Kleiser, I. K. W., & Kasen, D. 2014, *MNRAS*, 438, 318
- Komissarov, S. S., & Barkov, M. V. 2007, *MNRAS*, 382, 1029
- Komissarov, S. S., & Lyubarsky, Y. E. 2004, *MNRAS*, 349, 779
- Kotera, K., Phinney, E. S., & Olinto, A. V. 2013, *MNRAS*, 432, 3228
- Kouveliotou, C., Meegan, C. A., Fishman, G. J., et al. 1993, *ApJ*, 413, L101
- Kouveliotou, C., Norris, J., Cline, T., et al. 1987, *The Astrophysical Journal*, 322, L21
- Kouveliotou, C., Fishman, G., Meegan, C., et al. 1993, *Nature*, 362, 728
- Kouveliotou, C., Dieters, S., Strohmayer, T., et al. 1998, *Nature*, 393, 235
- Kozasa, T., & Hasegawa, H. 1987, *Progress of Theoretical Physics*, 77, 1402
- Kozasa, T., Hasegawa, H., & Nomoto, K. 1989, *ApJ*, 344, 325
- . 1991, *A&A*, 249, 474
- Kozyreva, A., & Blinnikov, S. 2015, *MNRAS*, 454, 4357
- Kramers, H. A. 1923, *The London, Edinburgh, and Dublin Philosophical Magazine and Journal of Science*, 46, 836
- Krolik, J. H., & Piran, T. 2011, *ApJ*, 743, 134
- Kulkarni, S. R., Ofek, E. O., & Neill, J. D. 2015, *ArXiv e-prints*, arXiv:1511.09137
- Kutschera, M., & Wójcik, W. 1989, *Physics Letters B*, 223, 11
- Kuzmin, A. D. 2007, in *WE-Heraeus Seminar on Neutron Stars and Pulsars 40 years after the Discovery*, ed. W. Becker & H. H. Huang, 72
- Lai, D. 2001, *Reviews of Modern Physics*, 73, 629
- Lakićević, M., van Loon, J. T., Stanke, T., De Breuck, C., & Patat, F. 2012, *A&A*, 541, L1
- Lamb, G. P., & Kobayashi, S. 2017, *ArXiv e-prints*, arXiv:1710.05857
- Landau, L. 1957a, *SOVIET PHYSICS JETP-USSR*, 5, 101

- . 1957b, *Soviet Physics JETP-USSR*, 3, 920
- Laros, J., Fenimore, E., Fikani, M., et al. 1986
- Laros, J., Fenimore, E., Klebesadel, R., et al. 1987, *The Astrophysical Journal*, 320, L111
- Lattimer, J. M., & Prakash, M. 2001, *ApJ*, 550, 426
- . 2007, *Phys. Rep.*, 442, 109
- Leloudas, G., Chatzopoulos, E., Dilday, B., et al. 2012, *A&A*, 541, A129
- Leloudas, G., Schulze, S., Krühler, T., et al. 2015, *MNRAS*, 449, 917
- Levan, A. J., Tanvir, N. R., Cenko, S. B., et al. 2011, *Science*, 333, 199
- Levan, A. J., Tanvir, N. R., Starling, R. L. C., et al. 2014, *ApJ*, 781, 13
- Lieb, E. H., & Yau, H.-T. 1987, *ApJ*, 323, 140
- Liebendoerfer, M. 2005, *JRASC*, 99, 140
- Lingam, M., & Loeb, A. 2017, *ApJ*, 837, L23
- Liu, L.-D., Wang, L.-J., Wang, S.-Q., & Dai, Z.-G. 2017, *ArXiv e-prints*, arXiv:1706.01783
- Liu, T., Romero, G. E., Liu, M.-L., & Li, A. 2016, *ApJ*, 826, 82
- Loeb, A. 2016, *ApJ*, 819, L21
- Lorimer, D. R., Bailes, M., McLaughlin, M. A., Narkevic, D. J., & Crawford, F. 2007, *Science*, 318, 777
- Lunnan, R., Chornock, R., Berger, E., et al. 2014, *ApJ*, 787, 138
- . 2016, *ApJ*, 831, 144
- . 2018, *ApJ*, 852, 81
- Lyne, A., Graham-Smith, F., Weltevrede, P., et al. 2013, *Science*, 342, 598
- Lyubarsky, Y. 2014, *MNRAS*, 442, L9
- Lyubarsky, Y., & Kirk, J. G. 2001, *ApJ*, 547, 437
- Lyubarsky, Y. E. 2002, *MNRAS*, 329, L34
- . 2003, *MNRAS*, 345, 153
- Lyutikov, M. 2002, *ApJ*, 580, L65
- Lyutikov, M., Burzawa, L., & Popov, S. B. 2016, *MNRAS*, 462, 941
- MacFadyen, A. I., Ramirez-Ruiz, E., & Zhang, W. 2006, in *American Institute of Physics Conference Series*, Vol. 836, *Gamma-Ray Bursts in the Swift Era*, ed. S. S. Holt, N. Gehrels, & J. A. Nousek, 48–53
- MacFadyen, A. I., & Woosley, S. E. 1999, *ApJ*, 524, 262
- MacFadyen, A. I., Woosley, S. E., & Heger, A. 2001, *ApJ*, 550, 410

- Maeda, K., Nakamura, T., Nomoto, K., et al. 2002, *ApJ*, 565, 405
- Manchester, R., Hobbs, G., Teoh, A., & Hobbs, M. 2005, *VizieR Online Data Catalog*, 7245, 105
- Mandea, M., & Balasis, G. 2006, *Geophysical Journal International*, 167, 586
- Mandelstam, S. 1958, *Physical Review*, 112, 1344
- Mann, A. 2017, *Proceedings of the National Academy of Science*, 114, 3269
- Marcote, B., Paragi, Z., Hessels, J. W. T., et al. 2017, *ApJ*, 834, L8
- Margutti, R., Chornock, R., Metzger, B. D., et al. 2017a, *ArXiv e-prints*, arXiv:1704.05865
- Margutti, R., Metzger, B. D., Chornock, R., et al. 2017b, *ApJ*, 836, 25
- Marschall, L. A. 1988, *The supernova story*
- Marshall, F., & Swank, J. H. 2003, *GRB Coordinates Network*, 1996
- Masui, K., Lin, H.-H., Sievers, J., et al. 2015, *Nature*, 528, 523
- Matheson, H., & Safi-Harb, S. 2010, *ApJ*, 724, 572
- Matheson, T., Garnavich, P., Olszewski, E. W., et al. 2003, *GRB Coordinates Network*, 2120
- Matsuura, M., Dwek, E., Meixner, M., et al. 2011, *Science*, 333, 1258
- Matsuura, M., Dwek, E., Barlow, M. J., et al. 2015, *ApJ*, 800, 50
- Maund, J. R., Wheeler, J. C., Patat, F., et al. 2007, *MNRAS*, 381, 201
- Mazets, E., & Golenetskii, S. 1981, *Astrophysics and Space Science*, 75, 47
- Mazets, E., Golenetskii, S., Il'Inskii, V., Guryan, Y. A., et al. 1979
- Mazets, E., Golenetskii, S., Il'Inskii, V., et al. 1981, *Astrophysics and Space Science*, 80, 3
- Mazzali, P. A., Sullivan, M., Pian, E., Greiner, J., & Kann, D. A. 2016, *MNRAS*, 458, 3455
- McCray, R. 1993, *ARA&A*, 31, 175
- Meegan, C. A., Fishman, G. J., Wilson, R. B., et al. 1992, *Nature*, 355, 143
- Meshkov, E. E. 1969, *Fluid Dynamics*, 4, 101
- Mestel, L., & Takhar, H. S. 1972, *MNRAS*, 156, 419
- Meszáros, P., & Rees, M. J. 1993, *ApJ*, 418, L59
- Mészáros, P., & Ventura, J. 1979, *Physical Review D*, 19, 3565
- Metzger, B. D., Berger, E., & Margalit, B. 2017, *ArXiv e-prints*, arXiv:1701.02370
- Metzger, B. D., Giannios, D., Thompson, T. A., Bucciantini, N., & Quataert, E. 2011, *MNRAS*, 413, 2031

- Metzger, B. D., Margalit, B., Kasen, D., & Quataert, E. 2015, *MNRAS*, 454, 3311
- Metzger, B. D., Vurm, I., Hascoët, R., & Beloborodov, A. M. 2014, *MNRAS*, 437, 703
- Metzger, B. D., Martínez-Pinedo, G., Darbha, S., et al. 2010, *MNRAS*, 406, 2650
- Micelotta, E. R., Dwek, E., & Slavin, J. D. 2016, *A&A*, 590, A65
- Michanowsky, G. 1977, The once and future star: exploring the mysterious link between the great southern supernova (Vela X) and the origins of civilization.
- Michilli, D., Seymour, A., Hessels, J. W. T., et al. 2018, ArXiv e-prints, arXiv:1801.03965
- Mizuta, A., & Ioka, K. 2013, *ApJ*, 777, 162
- Mochkovitch, R., Hernanz, M., Isern, J., & Martin, X. 1993, *Nature*, 361, 236
- Mooley, K. P., Nakar, E., Hotokezaka, K., et al. 2017, ArXiv e-prints, arXiv:1711.11573
- Moriya, T., Tominaga, N., Tanaka, M., Maeda, K., & Nomoto, K. 2010, *ApJ*, 717, L83
- Mösta, P., Richers, S., Ott, C. D., et al. 2014, *ApJ*, 785, L29
- Mottez, F., & Zarka, P. 2014, *A&A*, 569, A86
- Mukherjee, S., Feigelson, E. D., Jogesh Babu, G., et al. 1998, *ApJ*, 508, 314
- Müller, B. 2015, *MNRAS*, 453, 287
- Müller, B. 2017, in *IAU Symposium, Vol. 329, The Lives and Death-Throes of Massive Stars*, ed. J. J. Eldridge, J. C. Bray, L. A. S. McClelland, & L. Xiao, 17–24
- Murase, K., Kashiyama, K., Kiuchi, K., & Bartos, I. 2015, *ApJ*, 805, 82
- Murase, K., Kashiyama, K., & Mészáros, P. 2016, *MNRAS*, 461, 1498
- . 2017a, *MNRAS*, 467, 3542
- Murase, K., Mészáros, P., & Fox, D. B. 2017b, *ApJ*, 836, L6
- Murase, K., Thompson, T. A., & Ofek, E. O. 2014, *MNRAS*, 440, 2528
- Murase, K., Toma, K., Yamazaki, R., & Mészáros, P. 2011, *ApJ*, 732, 77
- Murase, K., Toma, K., Yamazaki, R., Nagataki, S., & Ioka, K. 2010, *MNRAS*, 402, L54
- Murdin, P., & Murdin, L. 1985, *Supernovae* (Cambridge University Press)
- Murdin, P., & Murdin, L. 2011, *Supernovae*
- Muslimov, A. G., & Harding, A. K. 2003, *ApJ*, 588, 430
- Nadyozhin, D. K. 1994, *ApJS*, 92, 527
- Nagakura, H., Iwakami, W., Furusawa, S., et al. 2017, ArXiv e-prints, arXiv:1702.01752
- Nakar, E. 2007, *Phys. Rep.*, 442, 166
- Nakar, E., & Piran, T. 2011, *Nature*, 478, 82
- . 2017, *ApJ*, 834, 28

- Nakar, E., & Sari, R. 2010, *ApJ*, 725, 904
- Narayan, R., Paczynski, B., & Piran, T. 1992, *ApJ*, 395, L83
- Nicholl, M., Berger, E., Margutti, R., et al. 2017a, *ApJ*, 845, L8
- . 2017b, *ApJ*, 835, L8
- Nicholl, M., Guillochon, J., & Berger, E. 2017c, *ApJ*, 850, 55
- Nicholl, M., & Smartt, S. J. 2016, *MNRAS*, 457, L79
- Nicholl, M., Williams, P. K. G., Berger, E., et al. 2017d, *ApJ*, 843, 84
- Nicholl, M., Smartt, S. J., Jerkstrand, A., et al. 2013, *Nature*, 502, 346
- . 2014, *MNRAS*, 444, 2096
- . 2015, *MNRAS*, 452, 3869
- Nicholl, M., Berger, E., Smartt, S. J., et al. 2016a, *ApJ*, 826, 39
- Nicholl, M., Berger, E., Margutti, R., et al. 2016b, *ApJ*, 828, L18
- Nicholl, M., Berger, E., Kasen, D., et al. 2017e, *ApJ*, 848, L18
- Norris, J., Hertz, P., Wood, K., & Kouveliotou, C. 1991, *The Astrophysical Journal*, 366, 240
- Nozawa, T., & Kozasa, T. 2013, *ApJ*, 776, 24
- Nozawa, T., Kozasa, T., & Habe, A. 2006, *ApJ*, 648, 435
- Nozawa, T., Kozasa, T., Habe, A., et al. 2007, *ApJ*, 666, 955
- Nozawa, T., Kozasa, T., Tominaga, N., et al. 2010, *ApJ*, 713, 356
- Nozawa, T., Kozasa, T., Umeda, H., Maeda, K., & Nomoto, K. 2003, *ApJ*, 598, 785
- Nozawa, T., Maeda, K., Kozasa, T., et al. 2011, *ApJ*, 736, 45
- Nozawa, T., Kozasa, T., Tominaga, N., et al. 2008, *ApJ*, 684, 1343
- Obergaulinger, M., Janka, H.-T., & Aloy, M. A. 2014, *MNRAS*, 445, 3169
- Ofek, E. O., Fox, D., Cenko, S. B., et al. 2013, *ApJ*, 763, 42
- Olausen, S., & Kaspi, V. 2014, *The Astrophysical Journal Supplement Series*, 212, 6
- Omand, C. M. B., Kashiyama, K., & Murase, K. 2017, *ArXiv e-prints*, arXiv:1704.00456
- Oppenheimer, J. R., & Volkoff, G. M. 1939, *Physical Review*, 55, 374
- Osterbrock, D. E. 2001, in *Bulletin of the American Astronomical Society*, Vol. 33, American Astronomical Society Meeting Abstracts, 1330
- Ostlie, D. A., & Carroll, B. W. 1996, *An Introduction to Modern Stellar Astrophysics*
- Ostriker, J. P., & Gunn, J. E. 1969, *ApJ*, 157, 1395
- . 1971, *ApJ*, 164, L95

- Pacini, F. 1967, *Nature*
- 1968, *Nature*, 219, 145
- Pacini, F., & Salvati, M. 1973, *ApJ*, 186, 249
- Paczynski, B. 1986, *ApJ*, 308, L43
- 1991, *Acta Astron.*, 41, 257
- 1992, *Acta Astron.*, 42, 145
- 1997, *ArXiv Astrophysics e-prints*, astro-ph/9712123
- Paczynski, B., & Rhoads, J. E. 1993, *ApJ*, 418, L5
- Palmer, D. M., Barthelmy, S., Gehrels, N., et al. 2005, *Nature*, 434, 1107
- Palmese, A., Hartley, W., Tarsitano, F., et al. 2017, *ApJ*, 849, L34
- Pan, K.-C., Liebendörfer, M., Hempel, M., & Thielemann, F.-K. 2016, *ApJ*, 817, 72
- Pan, Y.-C., Foley, R. J., Smith, M., et al. 2017, *MNRAS*, 470, 4241
- Pastorello, A., Smartt, S. J., Botticella, M. T., et al. 2010, *ApJ*, 724, L16
- Patat, F., Cappellaro, E., Danziger, J., et al. 2001, *ApJ*, 555, 900
- Pavlov, G., & Shibanov, Y. A. 1979, *Sov. Phys.-JETP (Engl. Transl.);(United States)*, 49
- Perna, R., Soria, R., Pooley, D., & Stella, L. 2008, *MNRAS*, 384, 1638
- Perna, R., & Stella, L. 2004, *ApJ*, 615, 222
- Peterson, B. A., & Price, P. A. 2003, *GRB Coordinates Network*, 1985
- Petroff, E., Bailes, M., Barr, E. D., et al. 2015, *MNRAS*, 447, 246
- Petroff, E., Barr, E. D., Jameson, A., et al. 2016, *PASA*, 33, e045
- Petropoulou, M., Kamble, A., & Sironi, L. 2016, *MNRAS*, 460, 44
- Phillips, M. M. 1993, *ApJ*, 413, L105
- Phinney, E. S. 1991, *ApJ*, 380, L17
- Pilkington, J., Hewish, A., Bell, S., & Cole, T. 1968, *Nature*, 218, 126
- Piran, T. 2004, *Reviews of Modern Physics*, 76, 1143
- Piro, A. L. 2015, *ApJ*, 808, L51
- Piro, A. L., & Kollmeier, J. A. 2017, *ArXiv e-prints*, arXiv:1710.05822
- Pons, J. A., & Geppert, U. 2007, *A&A*, 470, 303
- Pons, J. A., Reddy, S., Prakash, M., Lattimer, J. M., & Miralles, J. A. 1999, *ApJ*, 513, 780
- Pons, J. A., Viganò, D., & Rea, N. 2013, *Nature Physics*, 9, 431
- Pontzen, A., Deason, A., Governato, F., et al. 2010, *MNRAS*, 402, 1523

- Popov, S. B., & Postnov, K. A. 2010a, in *Evolution of Cosmic Objects through their Physical Activity*, ed. H. A. Harutyunian, A. M. Mickaelian, & Y. Terzian, 129–132
- Popov, S. B., & Postnov, K. A. 2010b, in *Evolution of Cosmic Objects through their Physical Activity*, ed. H. A. Harutyunian, A. M. Mickaelian, & Y. Terzian, 129–132
- Porth, O., Komissarov, S. S., & Keppens, R. 2013, *MNRAS*, 431, L48
- Prochaska, J. X., Bloom, J. S., Chen, H.-W., et al. 2006, *ApJ*, 642, 989
- Quimby, R. M., Aldering, G., Wheeler, J. C., et al. 2007, *ApJ*, 668, L99
- Quimby, R. M., Kulkarni, S. R., Kasliwal, M. M., et al. 2011, *Nature*, 474, 487
- Rabinak, I., & Waxman, E. 2011, *ApJ*, 728, 63
- Ramirez-Ruiz, E., Celotti, A., & Rees, M. J. 2002, *MNRAS*, 337, 1349
- Rangelov, B., Pavlov, G. G., Kargaltsev, O., et al. 2016, *ApJ*, 831, 129
- . 2017, *ApJ*, 835, 264
- Ravi, V., & Lasky, P. D. 2014, *MNRAS*, 441, 2433
- Razin, V. 1960, *Izvestiya Vysshikh Uchebnykh Zavedenii. Radiofizika*, 584
- Rees, M. J., & Gunn, J. E. 1974, *MNRAS*, 167, 1
- Renault-Tinacci, N., Kotera, K., Neronov, A., & Ando, S. 2017, *ArXiv e-prints*, arXiv:1708.08971
- Reynolds, S. P., & Chevalier, R. A. 1984, *ApJ*, 278, 630
- Richtmyer, R. D. 1960, *Communications on Pure and Applied Mathematics*, 13, 297
- Romani, R. W. 1996, *ApJ*, 470, 469
- Romani, R. W., & Yadigaroglu, I.-A. 1995, *ApJ*, 438, 314
- Rosswog, S., & Brüggen, M. 2007, *Introduction to high-energy astrophysics* (Cambridge University Press Cambridge)
- Ruderman, M. A., & Sutherland, P. G. 1975, *ApJ*, 196, 51
- Rybicki, G. B., & Lightman, A. P. 1979, *Radiative processes in astrophysics*
- Rykoff, E. S., Aharonian, F., Akerlof, C. W., et al. 2009, *ApJ*, 702, 489
- Sandage, A., Saha, A., Tammann, G. A., Panagia, N., & Macchetto, D. 1992, *ApJ*, 401, L7
- Sari, R., Piran, T., & Halpern, J. P. 1999, *ApJ*, 519, L17
- Schilling, G. 2002, *Flash! The Hunt for the Biggest Explosions in the Universe*
- Scholz, P., Spitler, L. G., Hessels, J. W. T., et al. 2016, *ApJ*, 833, 177
- Schreier, E., Levinson, R., Gursky, H., et al. 1972, *ApJ*, 172, L79
- Sedov, L. I. 1946, *Journal of Applied Mathematics and Mechanics*, 10, 241

- Shand, Z., Ouyed, A., Koning, N., & Ouyed, R. 2016, *Research in Astronomy and Astrophysics*, 16, 80
- Shapiro, S. L., & Teukolsky, S. A. 1983, *Black holes, white dwarfs, and neutron stars: The physics of compact objects*
- Shklovskii, I. S. 1973, *Soviet Ast.*, 16, 749
- . 1976, *Soviet Ast.*, 19, 554
- Shklovsky, I. 1967, *The Astrophysical Journal*, 148, L1
- Shu, F. H. 1991, *Physics of Astrophysics, Vol. I (University Science Books)*
- Sibthorpe, B., Ade, P. A. R., Bock, J. J., et al. 2010, *ApJ*, 719, 1553
- Sironi, L., & Spitkovsky, A. 2011, *ApJ*, 741, 39
- Skidmore, W., et al. 2015, *Research in Astronomy and Astrophysics*, 15, 1945
- Slane, P. 2017, *ArXiv e-prints*, arXiv:1703.09311
- Smartt, S. J., Chen, T.-W., Jerkstrand, A., et al. 2017, *Nature*, 551, 75
- Smith, M., Sullivan, M., D'Andrea, C. B., et al. 2016, *ApJ*, 818, L8
- Smith, N., Chornock, R., Li, W., et al. 2008, *ApJ*, 686, 467
- Smith, N., & McCray, R. 2007, *ApJ*, 671, L17
- Soares-Santos, M., Holz, D. E., Annis, J., et al. 2017, *ApJ*, 848, L16
- Soderberg, A. M., Berger, E., Page, K. L., et al. 2008, *Nature*, 453, 469
- Soglasnov, V. A., Popov, M. V., Bartel, N., et al. 2004, *ApJ*, 616, 439
- Spitkovsky, A. 2006, *ApJ*, 648, L51
- Spitler, L. G., Cordes, J. M., Hessels, J. W. T., et al. 2014, *ApJ*, 790, 101
- Spitler, L. G., Scholz, P., Hessels, J. W. T., et al. 2016, *Nature*, 531, 202
- Spruit, H. C. 2002, *A&A*, 381, 923
- Staelin, D. H., & Reifenstein, III, E. C. 1968, *Science*, 162, 1481
- Stanek, K. Z., Matheson, T., Garnavich, P. M., et al. 2003, *ApJ*, 591, L17
- Stella, L., Dall'Osso, S., Israel, G. L., & Vecchio, A. 2005, *ApJ*, 634, L165
- Stephenson, F. R., & Clark, D. H. 1976, *Scientific American*, 234, 100
- Stephenson, F. R., & Green, D. A. 2003, *S&T*, 105
- . 2005, *Journal for the History of Astronomy*, 36, 217
- Stothers, R. 1977, *Isis*, 68, 443
- Suzuki, A., & Maeda, K. 2017, *MNRAS*, 466, 2633
- Tanaka, M., Kawabata, K. S., Hattori, T., et al. 2012, *ApJ*, 754, 63

- Tanaka, M., Utsumi, Y., Mazzali, P. A., et al. 2017, *PASJ*, 69, 102
- Tanaka, S. J., & Takahara, F. 2010, *ApJ*, 715, 1248
- . 2013, *MNRAS*, 429, 2945
- Tananbaum, H., Gursky, H., Kellogg, E. M., et al. 1972, *ApJ*, 174, L143
- Tanvir, N. R., Levan, A. J., Fruchter, A. S., et al. 2013, *Nature*, 500, 547
- Tchekhovskoy, A., Spitkovsky, A., & Li, J. G. 2013, *MNRAS*, 435, L1
- Temim, T., Dwek, E., Arendt, R. G., et al. 2017, *ApJ*, 836, 129
- Tendulkar, S. P., Kaspi, V. M., & Patel, C. 2016, arXiv:1602.02188, arXiv:1602.02188
- Tendulkar, S. P., Bassa, C. G., Cordes, J. M., et al. 2017, *ApJ*, 834, L7
- Terasawa, T., Tanaka, Y. T., Takei, Y., et al. 2005, *Nature*, 434, 1110
- Terreran, G., Pumo, M. L., Chen, T.-W., et al. 2017, *Nature Astronomy*, 1, 713
- Thirumalai, A., & Heyl, J. S. 2009, *Physical Review A*, 79, 012514
- Thompson, C., & Duncan, R. C. 1993, *ApJ*, 408, 194
- Thompson, C., & Duncan, R. C. 1995, *Monthly Notices of the Royal Astronomical Society*, 275, 255
- . 1996, *The Astrophysical Journal*, 473, 322
- . 2001, *The Astrophysical Journal*, 561, 980
- Thompson, C., Lyutikov, M., & Kulkarni, S. 2002, *The Astrophysical Journal*, 574, 332
- Thompson, T. A., Burrows, A., & Meyer, B. S. 2001, *ApJ*, 562, 887
- Thompson, T. A., Chang, P., & Quataert, E. 2004, *ApJ*, 611, 380
- Thornton, D., Stappers, B., Bailes, M., et al. 2013, *Science*, 341, 53
- Timokhin, A. N., & Harding, A. K. 2015, *ApJ*, 810, 144
- Todini, P., & Ferrara, A. 2001, *MNRAS*, 325, 726
- Tolman, R. C. 1939, *Physical Review*, 55, 364
- Tolstov, A., Zhiglo, A., Nomoto, K., et al. 2017, *ApJ*, 845, L2
- Tong, H., & Yu, C. 2017, *ArXiv e-prints*, arXiv:1711.06593
- Totani, T. 2013, *PASJ*, 65, arXiv:1307.4985
- Tóth, L. V., Zahorecz, S., & Kiss, C. 2013, *Infrared Astronomy (Eötvös Loránd University)*
- Troja, E., Cusumano, G., O'Brien, P. T., et al. 2007, *ApJ*, 665, 599
- Truelove, J. K., & McKee, C. F. 1999, *ApJS*, 120, 299
- Usov, V. 1996, arXiv preprint astro-ph/9612091

- Usov, V. V. 1992, *Nature*, 357, 472
- Usov, V. V., & Melrose, D. B. 1995, *Australian Journal of Physics*, 48, 571
- Utsumi, Y., Tanaka, M., Tominaga, N., et al. 2017, *PASJ*, 69, 101
- Valenti, S., David, Sand, J., et al. 2017, *ApJ*, 848, L24
- van der Swaluw, E. 2003, *A&A*, 404, 939
- Van Der Swaluw, E., Achterberg, A., & Gallant, Y. A. 1998, *Mem. Soc. Astron. Italiana*, 69, 1017
- van der Swaluw, E., Achterberg, A., Gallant, Y. A., & Tóth, G. 2001, *A&A*, 380, 309
- van der Swaluw, E., Downes, T. P., & Keegan, R. 2004, *A&A*, 420, 937
- van Paradijs, J., Groot, P. J., Galama, T., et al. 1997, *Nature*, 386, 686
- Vanderspek, R., Crew, G., Doty, J., et al. 2003, *GRB Coordinates Network*, 1997
- Vietri, M., & Stella, L. 1998, *ApJ*, 507, L45
- Vink, J., Bleeker, J., van der Heyden, K., et al. 2006, *ApJ*, 648, L33
- Virgili, F. J., Liang, E.-W., & Zhang, B. 2009, *MNRAS*, 392, 91
- Virgili, F. J., Mundell, C. G., Pal'shin, V., et al. 2013, *ApJ*, 778, 54
- Vishniac, E. T. 1994, *ApJ*, 428, 186
- Vlasis, A., Dessart, L., & Audit, E. 2016, *MNRAS*, 458, 1253
- Vreeswijk, P., Tanvir, N., & Galama, T. 2000, *The Newsletter of the Isaac Newton Group of Telescopes*, 2, 5
- Vreeswijk, P. M., Savaglio, S., Gal-Yam, A., et al. 2014, *ApJ*, 797, 24
- Vreeswijk, P. M., Leloudas, G., Gal-Yam, A., et al. 2017, *ApJ*, 835, 58
- Wang, L., Howell, D. A., Höflich, P., & Wheeler, J. C. 2001, *ApJ*, 550, 1030
- Wang, S. Q., Wang, L. J., Dai, Z. G., & Wu, X. F. 2015, *ApJ*, 807, 147
- Watts, A. L., Andersson, N., Chakrabarty, D., et al. 2016, *Reviews of Modern Physics*, 88, 021001
- Waxman, E., & Draine, B. T. 2000, *ApJ*, 537, 796
- Waxman, E., & Mészáros, P. 2003, *ApJ*, 584, 390
- Weber, F., Negreiros, R., Rosenfield, P., & Stejner, M. 2007, *Progress in Particle and Nuclear Physics*, 59, 94
- Wheeler, J. C., & Akiyama, S. 2010, *New A Rev.*, 54, 183
- Wheeler, J. C., Yi, I., Höflich, P., & Wang, L. 2000, *ApJ*, 537, 810
- Wijers, R. A. M. J., & Galama, T. J. 1999, *ApJ*, 523, 177
- Winkler, P. F., Gupta, G., & Long, K. S. 2003, *The Astrophysical Journal*, 585, 324

- Winterberg, F. 2001, *Zeitschrift Naturforschung Teil A*, 56, 889
- Wolszczan, A., Prószyński, M., Graham, D. A., & Wright, G. A. E. 1984, in *BAAS*, Vol. 16, *Bulletin of the American Astronomical Society*, 728
- Woods, P. M., Kouveliotou, C., van Paradijs, J., et al. 1999, *The Astrophysical Journal Letters*, 519, L139
- Woosley, S. E. 2010, *ApJ*, 719, L204
- Woosley, S. E., & Bloom, J. S. 2006, *ARA&A*, 44, 507
- Woosley, S. E., Eastman, R. G., & Schmidt, B. P. 1999, *ApJ*, 516, 788
- Woosley, S. E., Hartmann, D. H., Hoffman, R. D., & Haxton, W. C. 1990, *ApJ*, 356, 272
- Woosley, S. E., & Haxton, W. C. 1988, *Nature*, 334, 45
- Yan, L., Quimby, R., Ofek, E., et al. 2015, *ApJ*, 814, 108
- Yan, L., Quimby, R., Gal-Yam, A., et al. 2017a, *ApJ*, 840, 57
- Yan, L., Lunnan, R., Perley, D. A., et al. 2017b, *ApJ*, 848, 6
- Yang, Y.-P., Zhang, B., & Dai, Z.-G. 2016, *ApJ*, 819, L12
- Yasuda, Y., & Kozasa, T. 2012, *ApJ*, 745, 159
- Zeilik, M., & van Panhuys Smith, E. 1987, Philadelphia: Saunders College Pub., c1987. 2nd ed., 1
- Zhang, B. 2014, *ApJ*, 780, L21
- . 2016, *ApJ*, 827, L31
- Zhang, B., & Mészáros, P. 2001, *ApJ*, 552, L35
- Zhang, W., Woosley, S. E., & MacFadyen, A. I. 2003, *ApJ*, 586, 356
- Zhao, F.-Y., Strom, R. G., & Jiang, S.-Y. 2006, *Chinese J. Astron. Astrophys.*, 6, 635